

Electronic Thesis and Dissertation Repository

12-1-2011 12:00 AM

Investigating Interfacial Reactions of Silver-Containing Films Using Novel Methods

Sarah Danielle Pretty, *University of Western Ontario*

Supervisor: Dr. Jungsook Clara Wren, *The University of Western Ontario*

A thesis submitted in partial fulfillment of the requirements for the Doctor of Philosophy degree in Chemistry

© Sarah Danielle Pretty 2011

Follow this and additional works at: <https://ir.lib.uwo.ca/etd>

 Part of the [Analytical Chemistry Commons](#), [Environmental Chemistry Commons](#), [Materials Chemistry Commons](#), and the [Physical Chemistry Commons](#)

Recommended Citation

Pretty, Sarah Danielle, "Investigating Interfacial Reactions of Silver-Containing Films Using Novel Methods" (2011). *Electronic Thesis and Dissertation Repository*. 327.
<https://ir.lib.uwo.ca/etd/327>

This Dissertation/Thesis is brought to you for free and open access by Scholarship@Western. It has been accepted for inclusion in Electronic Thesis and Dissertation Repository by an authorized administrator of Scholarship@Western. For more information, please contact wlsadmin@uwo.ca.

**INVESTIGATING INTERFACIAL REACTIONS OF SILVER-CONTAINING
FILMS USING NOVEL METHODS**

(Spine title: Interfacial Reactions of Silver Films)

(Thesis format: Integrated-Article)

by

Sarah D. Pretty

Graduate Program in Chemistry

A thesis submitted in partial fulfillment
of the requirements for the degree of
Doctor of Philosophy

The School of Graduate and Postdoctoral Studies
The University of Western Ontario
London, Ontario, Canada

© Sarah D. Pretty 2011

CERTIFICATE OF EXAMINATION

Supervisor

Dr. Clara Wren

Supervisory Committee

Dr. Martin Stillman

Dr. Peter Guthrie

Examiners

Dr. Ron Martin

Dr. Viktor Staroverov

Dr. Gordon Southam

Dr. Gerald Frankel

The thesis by

Sarah Danielle Pretty

entitled:

**INVESTIGATING INTERFACIAL REACTIONS OF SILVER-CONTAINING FILMS
USING NOVEL METHODS**

is accepted in partial fulfillment of the
requirements for the degree of
Doctor of Philosophy

Date _____

Chair of the Thesis Examination Board

Abstract

This thesis presents work on the mechanism and kinetics of the surface film reactions involving the conversion of aqueous species on solid surfaces, and specifically, the reactions of iodide and bromide on silver oxide on silver substrate. These reactions provide a method of immobilizing unwanted halides and are particularly suited to control of hazardous radioactive iodine. Potential applications of this research include nuclear reactor safety and post-accident radioiodine management, and the safe production and use of the medical isotope ^{131}I .

The aqueous-solid conversion of reaction Ag_2O with $\text{X}^-(\text{aq})$ to form AgX on a Ag substrate can occur via one of three main reaction pathways. The first pathway is a chemical reaction that occurs at the oxide/solution interface. This is a molecule-molecule interaction that does not involve charge transfer. A second, electrochemical (galvanic coupling) reaction pathway is possible where the reduction of Ag_2O to Ag is coupled to the oxidation of Ag to AgX . Lastly, conversion can proceed via a dissolution pathway where $\text{Ag}^+(\text{aq})$ released from Ag_2O dissolution reacts with $\text{X}^-(\text{aq})$ in solution and AgX precipitates on the Ag surface. The fastest reaction path will determine the nature of the AgX film that is formed. From the perspective of immobilizing the halide ion, the dissolution pathway would be least effective. We are interested in understanding how the system thermodynamics and mass transport properties affect the relative pathway rates.

The kinetics of the $\text{Ag} | \text{Ag}_2\text{O} | \text{X}^-(\text{aq})$ solid-liquid interfacial reactions were studied using a range of electrochemical techniques. Different electrochemical measurements provided chemical kinetic information. The diffusion-limited and surface reaction-limited components of the total reaction rate were separated by measuring the reaction time as a function of the

electrode rotation rate. Linear polarization and potentiostatic polarization were used to probe the rate of the galvanic coupling reaction.

These studies concluded that the reaction of iodide with silver oxide proceeds mainly via the chemical reaction pathway, while the corresponding reaction of bromide proceeds via a combination of the galvanic coupling and the dissolution reaction pathways.

Keywords:

reaction kinetics, film conversion, silver, silver oxide, silver halide, solid-liquid interfacial reactions, galvanic coupling, radioiodine, electrochemical reaction

Acknowledgements

Firstly, I would like to thank my supervisor, Dr. Clara Wren, for offering her input, direction, and interpretation of my project throughout my years of study. Clara's hard work and dedication to her students has given me the most fulfilling graduate experience possible. I have traveled to international conferences in North America and Europe, and was given the opportunity to perform experiments in Australia. These events have helped shape who I am both personally and professionally. I cannot thank Clara enough for all of the lessons that she has taught me. I just hope to make her proud when I continue on in my professional career.

I would also like to acknowledge Dr. Jamie Noël. I think all of Clara's graduate students would agree that Jamie's sense of humor, patience, and intelligence are invaluable assets to the group. I am especially thankful for his patience, as I'm sure I have tested it many times.

I would like to thank all of the graduate students in the Wren lab. I was so fortunate to work with my best friends for the last five years. Like the saying goes, "it takes a village to raise a child," it took a group of talented, kind, caring, and encouraging people to get me to where I am today, and I will never forget that.

Finally, I would like to thank my husband Jason and my family for all of their love and support. Anyone who works in the research field understands how difficult the experience can be. Luckily, I was supported and loved unconditionally from the most exceptional husband and family that anyone could ever have.

Table of Contents

Certificate of Examination	ii
Abstract	iii
Acknowledgements	v
Table of Contents	vi
List of Symbols and Acronyms	xiii
List of Tables	xv
List of Figures	xvi
Chapter 1: Introduction	1
1.1 Thesis Objectives	1
1.2 Research Applications	2
1.2.1 Atmospheric Corrosion of Silver	4
1.2.2 Nuclear Reactor Accidents and the Release of Radioactive Material	7
1.3 Experimental Approach	17
1.4 Thesis Organization	17
1.5 References	18
Chapter 2: Experimental Principles and Details	23
2.1 Experimental Set-Up	23
2.1.1 Electrochemical Cell	23
2.1.2 Solution Preparation	25

2.1.3 Sample Preparation	25
2.2 Electrochemical Reactions at an Electrode Surface.....	26
2.3 Principles of Electrochemical Techniques.....	33
2.3.1 Open Circuit Potential Measurements	33
2.3.2 Cyclic Voltammetry	34
2.3.3 Potentiostatic Polarization.....	36
2.3.4 Cathodic Stripping Voltammetry	37
2.3.5 Galvanostatic Polarization	38
2.3.6 Linear Polarization Measurements.....	39
2.3.7 Rotating Disc Electrode Experiments	40
2.4 Surface Analysis	43
2.4.1 X-Ray Diffraction	43
2.4.2 Scanning Electron Microscopy	44
2.4.3 X-Ray Photoelectron Spectroscopy	46
2.4.4 Neutron Reflectometry.....	47
2.5 References.....	51

Chapter 3: A Comparison of the Electrochemical Behaviour of Silver-Containing Films on Silver Substrate..... 54

3.1 Introduction.....	54
3.2 Experimental Details.....	54
3.3 Results and Discussion	55
3.3.1 Cyclic Voltammetry in NaOH Solutions	55

3.3.2 General Features of the Electrochemical Oxidation of Ag in Alkaline Solutions.....	60
3.3.3 Cyclic Voltammetry in Solutions Containing Br ⁻ (aq) or I ⁻ (aq)	63
3.3.4 General Features of the Electrochemical Oxidation of Ag in Iodide and Bromide Solutions	66
3.3.5 Cyclic Voltammetry in Solutions Containing Cl ⁻ (aq)	67
3.3.6 Potentiostatic Film Growth of Ag ₂ O, AgI, AgBr, and AgCl	68
3.4 Summary and Conclusions	72
3.5 References.....	73

Chapter 4: Interfacial Reaction Kinetics of I⁻(aq) with Ag₂O on Ag Substrate: Kinetic

Model.....	75
4.1 Introduction.....	75
4.2 Experimental Details.....	77
4.3 Results and Discussion	79
4.3.1 Characterization of Electrochemically Grown Ag ₂ O Films.....	79
4.3.2 E _{OC} Behaviour Observed During the Reaction of Ag ₂ O in I ⁻ (aq) Solutions	80
4.3.3 Amounts of Ag ₂ O and AgI as a Function of Reaction Time	83
4.4 Reaction Kinetic Analysis.....	87
4.4.1 Reaction Orders	87
4.4.2 Apparent Reaction Rate Constant.....	91
4.5 Conclusions.....	92

4.6 References.....	94
---------------------	----

Chapter 5: Investigation of Interfacial Reaction Kinetics of $\Gamma^-(aq)$ with $Ag_2O(s)$ on Ag

Substrate: Determining Mass Transport and Surface Reaction Rates..... 95

5.1 Introduction.....	95
-----------------------	----

5.2 Experimental Details.....	95
-------------------------------	----

5.3 Results and Discussion	96
----------------------------------	----

5.3.1 Mass Transport Rate and Surface Reaction Rate.....	96
--	----

5.4 Comparison of Kinetic Parameters to Established Literature Values.....	101
--	-----

5.5 Summary and Conclusions	103
-----------------------------------	-----

5.6 References.....	104
---------------------	-----

Chapter 6: In Situ Conversion of Silver Oxide-Halide Films Studied by Neutron

Reflectometry 105

6.1 Introduction.....	105
-----------------------	-----

6.2 Experimental Details.....	107
-------------------------------	-----

6.2.1 Stand-Alone Electrochemistry and XPS Measurements.....	107
--	-----

6.2.2 Neutron Reflectometry Coupled with In Situ Electrochemistry	108
---	-----

6.3 Results and Discussion	112
----------------------------------	-----

6.3.1 Neutron Reflectometry – As-Prepared Film	112
--	-----

6.3.2 Neutron Reflectometry – As-Prepared Film in Solution at E_{OC}	115
--	-----

6.3.3 In Situ Ag_2O Film Growth	117
---	-----

6.3.4 In Situ Conversion of Ag_2O to AgI	120
--	-----

6.4 Conclusions.....	129
----------------------	-----

6.5 References.....	130
---------------------	-----

Chapter 7: Comparison of the Interfacial Reaction Kinetics of Bromide and Iodide Anion with Silver Oxide on an Ag Substrate..... 131

7.1 Introduction.....	131
-----------------------	-----

7.2 Experimental Details.....	132
-------------------------------	-----

7.3 Results.....	135
------------------	-----

7.3.1 E _{OC} Behaviour Observed During the Reaction of Ag ₂ O in Br ⁻ (aq) Solutions	135
---	-----

7.3.2 Observed Dependence of Total Reaction Time on [X ⁻ (aq)] ₀ and (Q _{Ag₂O}) ₀	136
---	-----

7.3.3 Observed Dependence of Total Reaction Time on Electrode Rotation Speed	140
--	-----

7.3.4 Galvanostatic Reduction Measurements	142
--	-----

7.3.5 Surface Analysis.....	145
-----------------------------	-----

7.4 Discussion.....	147
---------------------	-----

7.4.1 Chemical Reaction Path (1)	147
--	-----

7.4.2 Galvanic Coupling Reaction Path (2)	149
---	-----

7.4.3 Ag ⁺ (aq) Dissolution Path (3).....	151
--	-----

7.5 Conclusions.....	152
----------------------	-----

7.6 References.....	153
---------------------	-----

Chapter 8: Investigating the Galvanic Coupling Reaction Pathway During the Conversion

of Ag₂O to AgX	154
8.1 Introduction.....	154
8.2 Experimental Details.....	155
8.2.1 Reaction of Ag ₂ O with X ⁻ (aq)	155
8.2.2 Potentiostatic Control Measurements	155
8.2.3 Linear Polarization Resistance Measurements.....	156
8.3 Results and Discussion	157
8.3.1 Open Circuit Behaviour Observed During the Conversion of Ag ₂ O to AgX.....	157
8.3.2 Reaction of Ag ₂ O with Br ⁻ (aq)	158
8.3.2.1 Potentiostatic Polarization at $(E^e)_{Ag_2O/Ag}$	158
8.3.2.2 Potentiostatic Polarization at the End of Stage 1.....	162
8.3.2.3 Linear Polarization Resistance Measurements	162
8.3.3 Reaction of Ag ₂ O with I ⁻ (aq).....	167
8.3.3.1 Potentiostatic Polarization at $(E^e)_{Ag_2O/Ag}$	167
8.3.3.2 Potentiostatic Polarization at the End of Stage 1.....	171
8.3.3.3 Linear Polarization Resistance Measurements	172
8.4 Conclusions.....	175
8.5 References.....	177
Chapter 9: Summary and Future Work	178
9.1 Summary.....	178

9.2 Future Work	180
Curriculum Vitae	183

Symbols and Acronyms

Symbols

a_X	Activity of Species X
atm	Atmosphere Pressure
b	Coherent Scattering Length
c^s	Surface Concentration
c^b	Bulk Concentration
$^{\circ}\text{C}$	Degrees Celsius
d	Interplanar Spacing
D	Diffusion Coefficient
E	Electrochemical Potential
E^e	Equilibrium Potential
E°	Standard Potential
E_{Corr}	Corrosion Potential
E_{OC}	Open Circuit Potential
E_{initial}	Initial Potential
E_{final}	Final Potential
F	Faraday Constant
$\Delta_r G$	Free Energy Change of a Reaction
$h\nu$	Energy of Incident Photons
i	Current
i_0	Exchange Current
i_A	Anodic Current
i_C	Cathodic Current
i_{Corr}	Corrosion Current
I_M	Measured Current Density
I_L	Limiting Current Density
J	Flux
\bar{k}	Rate Constant
\bar{k}_o	Pre-exponential factor
K_{eq}	Equilibrium Constant
n	Electrons
Q	Charge
Q_A	Anodic Charge
Q_C	Cathodic Charge
Q_z	Momentum Transfer
R	Universal Gas Constant

t	time
T	Absolute Temperature (K)
\bar{v}	Forward Rate
z	Order of Reflection
α_A	Anodic Transfer Coefficient
α_C	Cathodic Transfer Coefficient
$\bar{\alpha}_o$	Symmetry Coefficient
δ	Nernst Diffusion Layer Thickness
η	Overpotential
θ	Angle of Incidence or Reflection
λ	Wavelength
ν	Kinematic Viscosity
ρ	Number Density of Atoms
σ	Scan Rate
ϕ	Work Function
ψ	Diffraction Angle
ω	Electrode Angular Velocity

Acronyms

ANSTO	Australian Nuclear Science and Technology Organisation
BE	Binding Energy
CE	Counter Electrode
CSV	Cathodic Stripping Voltammetry/Voltammogram
CV	Cyclic Voltammetry/Voltammogram
EDX	X-Ray Energy Dispersive Spectroscopy
KE	Kinetic Energy
NR	Neutron Reflectometry
PTFE	Polytetrafluoroethylene
XPS	X-Ray Photoelectron Spectroscopy
XRD	X-Ray Diffraction
RE	Reference Electrode
SCE	Saturated Calomel Electrode
SEM	Scanning Electron Microscopy
SLD	Scattering Length Density
SHE	Standard Hydrogen Electrode
WE	Working Electrode

List of Tables

Table 6.1	Numerical parameters of the least squares fitted model representing the as-prepared sample in air, electrolyte, and throughout step-wise anodization	114
Table 6.2	Numerical parameters of the least squares fitted model, representing the sample after the addition of KI	123
Table 6.3	Summary of the calculated amount of Ag_2O , AgI and AgCl from the neutron reflectometry experiment compared to cathodic stripping voltammetry	128
Table 7.1	Measured quantities of Ag_2O and AgBr on an electrode and amount of $\text{Ag}^+(\text{aq})$ dissolved for different reaction times.....	143
Table 7.2	Thermodynamic parameters for species involved in the $\text{Ag}_2\text{O}/\text{AgX}$ reactions	148

List of Figures

Figure 1.1	The potential-pH equilibrium diagram for Ag in H ₂ O at 25 °C. Figure is adopted from data found in [26].....	5
Figure 1.2	Schematic of the key components of a nuclear reactor	8
Figure 1.3	Fission yield, frequency distribution of the fission products generated in the fission of ²³⁵ U	9
Figure 1.4	Transport flow paths of iodine for CANDU reactor under accident conditions	11
Figure 1.5	Schematic representation of the Ag surface at the beginning and end of the surface chemical reaction	14
Figure 1.6	Schematic representation of the galvanic coupling reaction described in equations (1.8a-c).....	14
Figure 1.7	Schematic representation of the dissolution reaction pathway.....	15
Figure 2.1	Schematic of a three-electrode cell setup	24
Figure 2.2	Schematic of an assembled silver working electrode	26
Figure 2.3	Current-potential relationship for a redox active species	32
Figure 2.4	Current-potential relationship for coupled reactions in a corrosion process	33
Figure 2.5	The potential-time profile applied in a cyclic voltammetric experiment.....	35
Figure 2.6	The current-potential response in a cyclic voltammetric experiment for a reaction in which all of the anodic charge is recovered during the cathodic scan	36
Figure 2.7	A schematic of the potential-time profile for a galvanostatic reduction measurement showing the reduction of a film containing Ag ₂ O and AgI. Once those species are consumed the potential drops to drive water reduction.....	39
Figure 2.8	Concentration profile of steady-state mass transport controlled reaction under controlled convective conditions	39
Figure 2.9	Schematic of a single photon/electron ejection process	47

Figure 2.10	A neutron beam is partially reflected and partially transmitted at the interface between two media	48
Figure 2.11	The Platypus time-of-flight neutron reflectometer	49
Figure 2.12	Reflectivity of a Si substrate covered by 400 Å of Ag (black line) or a Si substrate covered by 50 Å of Ag (red line). The Kiessig fringes corresponding to the total film thickness of the layer are denoted by arrows	51
Figure 3.1	Cyclic voltammogram recorded on Ag in (a) 0.01 mol·dm ⁻³ NaOH solutions to an anodic limit of 0.4 V _{SCE} and (b) 0.02 mol·dm ⁻³ NaH ₂ PO ₄ solutions to an anodic limit of 0.6 V _{SCE}	56
Figure 3.2	SEM images of an Ag ₂ O film grown in (a) 0.01 mol·dm ⁻³ NaOH and (b) 0.02 mol·dm ⁻³ NaH ₂ PO ₄ . The total anodic charges, $(Q_{Ag_2O})_0$, used to grow the films were 0.050 C in both cases	58
Figure 3.3	Cyclic voltammograms recorded on Ag electrodes in 0.01 mol·dm ⁻³ NaOH at various electrode rotation speeds.....	60
Figure 3.4	Cyclic voltammograms recorded on Ag electrodes in solutions containing KI or KBr	65
Figure 3.5	Cyclic voltammograms recorded on Ag electrodes in halide-free NaOH, or solutions containing KI or KBr at a concentration of 5×10^{-4} mol·dm ⁻³	66
Figure 3.6	Cyclic voltammograms recorded on Ag electrodes in halide-free NaOH and 5×10^{-4} mol·dm ⁻³ KCl solutions.....	68
Figure 3.7	Anodic charges accumulated during Ag ₂ O, AgBr, AgCl, and AgI film growth. For all silver-halide films the bulk halide concentration was 5×10^{-4} mol·dm ⁻³ , and the halide-free NaOH concentration was 0.01 mol·dm ⁻³	70
Figure 3.8	SEM images of (a) Ag ₂ O, (b) AgI, (c) AgBr and (d) AgCl grown potentiostatically on Ag electrodes	71
Figure 4.1	XRD patterns recorded for the oxides grown ($(Q_{Ag_2O})_0 = 0.050$ C) in the presence of 0.02 mol·dm ⁻³ NaH ₂ PO ₄ and in 0.01 mol·dm ⁻³ NaOH.....	80
Figure 4.2	Open circuit potential as a function of reaction time and its dependence on $[\Gamma(\text{aq})]_0$ in NaOH solutions where $(Q_{Ag_2O})_0$ was constant at 0.050 C. The concentration of $\Gamma(\text{aq})$ ranged from 4×10^{-5} to 5×10^{-3} mol·dm ⁻³	81

Figure 4.3	Open circuit potential as a function of reaction time and its dependence on $(Q_{Ag_2O})_0$ in NaOH solutions. For these experiments, $[I^-(aq)]_0$ was constant at $5 \times 10^{-4} \text{ mol}\cdot\text{dm}^{-3}$ and $(Q_{Ag_2O})_0$ ranged from 0.035 to 0.063 C.....	82
Figure 4.4	Final steady-state E_{OC} values observed for various $[I^-(aq)]_0$ compared to calculated equilibrium potential values for the $Ag + I^-(aq) \rightarrow AgI + e^-$ reaction	83
Figure 4.5	(a) Cathodic stripping voltammograms performed on the Ag_2O/AgI covered electrodes following termination of the reaction at various times, and (b) cathodic charges used for the reduction of Ag_2O to Ag and AgI to Ag determined from the CSV. For these experiments $(Q_{Ag_2O})_0$ was 0.050 C and $[I^-(aq)]_0$ was constant at $5 \times 10^{-4} \text{ mol}\cdot\text{dm}^{-3}$	84
Figure 4.6	SEM images of the Ag electrode surface obtained after various reaction times. The times when the reaction was terminated, and the SEM images taken, are shown in (a), and the corresponding micrographs are shown in (b-d).....	87
Figure 4.7	(a) Plot of the log of the total reaction time vs. log of $[I^-(aq)]_0$. (b) Plot of the log of the total reaction time vs. log $(Q_{Ag_2O})_0$	91
Figure 5.1	(a) E_{OC} as a function of reaction time and its dependence on electrode rotation rate, and (b) total reaction time vs. $1/\omega^{-1/2}$. The experimental conditions were $0.01 \text{ mol}\cdot\text{dm}^{-3}$ NaOH, $(Q_{Ag_2O})_0$ was constant at 0.050 C and $[I^-(aq)]_0$ was $5 \times 10^{-4} \text{ mol}\cdot\text{dm}^{-3}$ for all cases. Electrode rotation rate ranged from 0 to 50 Hz	98
Figure 5.2	(a) E_{OC} as a function of reaction time and its dependence on electrode rotation rate, and (b) total reaction time vs. $1/\omega^{-1/2}$. The experimental conditions were $0.02 \text{ mol}\cdot\text{dm}^{-3}$ NaH_2PO_4 , $(Q_{Ag_2O})_0$ was constant at 0.050 C and $[I^-(aq)]_0$ was $5 \times 10^{-4} \text{ mol}\cdot\text{dm}^{-3}$ for all cases. Electrode rotation rate ranged from 0 to 50 Hz	100
Figure 6.1	A schematic view of the experimental set-up used during the in situ neutron reflectometry experiments	109
Figure 6.2	A potential vs. time plot of the experimental approach used to study: (1) the anodic growth of Ag_2O , and (2) the chemical reaction of a Ag_2O film with $I^-(aq)$	110
Figure 6.3	Least-squares fitted SLD profile of the as-prepared sample. The numerical parameters of the model, consisting of four distinct layered species: Si, Ag, AgOH and air are given in Table 6.1. The normalized neutron reflectivity spectra of the sample and proposed model are inset	113
Figure 6.4	XPS survey spectra of the as-prepared Ag sample after sputter deposition....	115

- Figure 6.5** Graphical representation of the numerical values presented in Table 6.1 indicating the progression of Ag₂O film growth 116
- Figure 6.6** SLD profile and normalized reflected neutron counts and calculated reflectivity for the Ag film at the end of 1200 s anodization..... 118
- Figure 6.7** SLD profile of the Ag electrode recorded after the addition of $1 \times 10^{-5} \text{ mol}\cdot\text{dm}^{-3}$ of $\Gamma(\text{aq})$. The observed neutron reflectivity spectrum and the predictions of our proposed model with five distinct layers is inset 120
- Figure 6.8** Graphical representation of the calculated Ag, Ag₂O, AgI, and AgCl thickness and roughness values after the addition of $\Gamma(\text{aq})$ 122
- Figure 6.9** Cathodic stripping voltammogram recorded approximately 8 hours after the addition of $1 \times 10^{-5} \text{ mol}\cdot\text{dm}^{-3}$ of $\Gamma(\text{aq})$ to the electrochemical cell solution. Cathodic stripping result recorded after a Ag₂O film with $(Q_{\text{Ag}_2\text{O}})_0$ 0.050 C was exposed to a solution containing $3 \times 10^{-3} \text{ mol}\cdot\text{dm}^{-3}$ of $\Gamma(\text{aq})$ and $3 \times 10^{-3} \text{ mol}\cdot\text{dm}^{-3}$ of $\text{Cl}^-(\text{aq})$ 125
- Figure 6.10** Open-circuit potential for a Ag₂O oxide grown at 0.4 V_{SCE} to a constant anodic charge $(Q_{\text{Ag}_2\text{O}})_0$ of 0.05 C. The Ag₂O film was exposed to, 1) [$\Gamma(\text{aq})$] of $5 \times 10^{-3} \text{ mol}\cdot\text{dm}^{-3}$, 2) [$\Gamma(\text{aq})$] of $1 \times 10^{-4} \text{ mol}\cdot\text{dm}^{-3}$, 3) [$\text{Cl}^-(\text{aq})$] of $5 \times 10^{-3} \text{ mol}\cdot\text{dm}^{-3}$ and 4) [$\text{Cl}^-(\text{aq})$] of $1 \times 10^{-4} \text{ mol}\cdot\text{dm}^{-3}$ 126
- Figure 6.11** SEM image of the Ag thin film electrode after Ag₂O film growth, film conversion and cathodic stripping..... 129
- Figure 7.1** Schematic representation of the potential vs. time profile used for the kinetic analysis of Ag₂O on Ag with aqueous $\text{Br}^-(\text{aq})$ 134
- Figure 7.2** A typical open circuit potential (E_{OC}) measurement observed of a Ag₂O film exposed to a solution containing $5 \times 10^{-4} \text{ mol}\cdot\text{dm}^{-3}$ of $\text{Br}^-(\text{aq})$. The stars indicate the times at which an Ag electrode was removed for SEM analysis (Figure 7.8) 136
- Figure 7.3** (a) A series of open circuit potential measurements performed at various $\text{Br}^-(\text{aq})$ concentrations where $(Q_{\text{Ag}_2\text{O}})_0$ is constant at 0.050 C. (b) Open circuit potential measurements carried out with different amounts of Ag₂O exposed to $5 \times 10^{-4} \text{ mol}\cdot\text{dm}^{-3}$ $\text{Br}^-(\text{aq})$ 137
- Figure 7.4** (a) Plot of the log of the total reaction time (τ_f) vs. log [$\text{X}^-(\text{aq})$]₀. (b) Plot of the log of the total reaction time (τ_f) vs. log $(Q_{\text{Ag}_2\text{O}})_0$ 139

- Figure 7.5** (a) E_{OC} plotted as a function of reaction time for different electrode rotation speeds, ω , and (b) total reaction time vs. $(\omega^{-1/2})$. For this data $(Q_{Ag_2O})_0$ was 0.050 C and $[Br^-(aq)]_0$ was $5 \times 10^{-4} \text{ mol}\cdot\text{dm}^{-3}$ 141
- Figure 7.6** Potential as a function of time for galvanostatic reduction of Ag_2O and $AgBr$ films. Prior to reduction, the Ag_2O films were grown to a constant anodic charge of 0.050 C and then exposed to solutions containing $[Br^-(aq)]_0$ at $5 \times 10^{-4} \text{ mol}\cdot\text{dm}^{-3}$ for different reaction times 143
- Figure 7.7** Fraction of Ag remaining on the Ag substrate as determined by the amounts of Ag_2O and $AgBr$ present. Also shown is the fraction of the initial Ag_2O after exposure of a film to a $0.01 \text{ mol}\cdot\text{dm}^{-3}$ $NaOH$ solution as a function of time and the amounts of Ag_2O and AgI calculated from the cathodic stripping results shown in Figure 4.5b. 144
- Figure 7.8** SEM images of the Ag electrode surface obtained after different reaction times 146
- Figure 7.9** EDX analysis carried out on the Ag electrode surface corresponding to the SEM images shown in Figure 7.8 and reaction times shown in Figure 7.2a 146
- Figure 8.1** Open circuit potential as a function of reaction time and its dependence on halide type. For these experiments, $(Q_{Ag_2O})_0$ was constant at 0.050 C and the halide concentration was $1 \times 10^{-4} \text{ mol}\cdot\text{dm}^{-3}$ 158
- Figure 8.2** (a) Currents observed during the potentiostatic periods of the partial control experiments as described in section 8.3.2.1 and 8.3.2.2. The current observed during anodization at 0.20 V_{SCE} of an oxide-free Ag electrode in $5 \times 10^{-4} \text{ mol}\cdot\text{dm}^{-3} Br^-(aq)$ solution is also shown for comparison. Potential profiles recorded during partially controlled potentiostatic experiments; (b) 0.22 V_{SCE} was applied for 1400 s immediately after transfer of the Ag_2O/Ag electrode to the bromide solution, followed by E_{OC} measurement; (c) E_{OC} was measured until the end of stage 1, followed by potentiostatic control at E_{OC} (0.20 V_{SCE}) for 700 s, followed by further measurement at E_{OC} 160
- Figure 8.3** Anodic and cathodic currents measured during polarization over the potential range $E_{OC} \pm 15 \text{ mV}_{SCE}$ during the conversion of Ag_2O to $AgBr$ in $1 \times 10^{-4} \text{ mol}\cdot\text{dm}^{-3} Br^-(aq)$ solutions 166
- Figure 8.4** (a) Currents observed during the potentiostatic periods of the partial control experiments as described in section 8.3.2.1 and 8.3.2.2. The current observed during anodization at 0.00 V_{SCE} of an oxide-free Ag electrode in $5 \times 10^{-4} \text{ mol}\cdot\text{dm}^{-3} I^-(aq)$ solutions is also shown for comparison. Potential profiles recorded during partially controlled potentiostatic experiments; (b) 0.22 V_{SCE} was applied for 600 s immediately after transfer of the Ag_2O/Ag electrode to the iodide solution, followed

by E_{OC} measurement; (c) E_{OC} was measured until the end of stage 1, followed by potentiostatic control at E_{OC} ($0.20 V_{SCE}$) for 300 s, followed by further measurement at E_{OC} 169

Figure 8.5 Schematic of the Ag/Ag₂O/solution interface in X⁻(aq) solutions..... 170

Figure 8.6 Anodic and cathodic currents measured during polarization over the potential range $E_{OC} \pm 15 mV_{SCE}$ during the conversion of Ag₂O to AgI in $1 \times 10^{-4} mol \cdot dm^{-3} \Gamma(aq)$ solutions..... 174

Figure 8.7 Current measured during polarization over the potential range $E_{OC} \pm 15 mV$ during the conversion of Ag₂O to AgI in $1 \times 10^{-4} mol \cdot dm^{-3} \Gamma(aq)$ solutions near the potential transition 175

Chapter 1

Introduction

1.1 Thesis Objectives

This thesis describes a number of studies that were performed on the reactions of $\text{Ag}_2\text{O}/\text{Ag}$ with halides in solution. The overall objective of this thesis is to establish the mechanism and kinetics of reactions involving the conversion of silver oxide (Ag_2O) to silver halide (AgX). There were multiple sub-objectives for the work as detailed below. The objectives are listed in the order in which the associated research is presented in the thesis.

- One objective was to examine the nature, both electrochemical and morphological, of silver oxide and silver halide films formed on Ag electrodes under various conditions. The type of films formed were investigated by changing variables such as halide species, halide concentration, overpotential, and electrolyte composition.
- A second objective was to identify the dominant chemical and electrochemical reaction pathways possible for the conversion of silver oxide films to silver halide films by reaction with aqueous halide anion.
- A third objective was to develop a kinetic model that can be used to study chemical reactions at the solid-aqueous interface. The kinetic model was first used to examine the conversion reaction of solid silver oxide with aqueous iodide anion to form solid silver iodide. From the kinetic model, the reaction orders and reaction rate constant were extracted. By studying the chemical conversion as a function of electrode rotation rate, in order to separate mass transport effects from

the reaction kinetics, a surface chemical reaction rate was determined. To confirm the validity of assumptions made in the kinetic model the conversion of silver oxide to silver iodide was monitored *in situ* using neutron reflectometry.

- A fourth objective was to examine the effect of electrolyte on (i) the composition and morphology of silver-containing films and (ii) the chemical reaction kinetics.
- A fifth objective was to explore how the different reaction thermodynamics and mass transport properties of the different halide ions affect interfacial reaction kinetics. This was accomplished by investigating the reaction of solid silver oxide with aqueous bromide anion. The changes to the competing rates of the dominant reaction pathways and how they affected the nature of the silver bromide film are discussed.
- The final objective was to evaluate the contribution of the electrochemical (galvanic coupling) reaction to the overall conversion reaction of silver oxide to silver halide.

1.2 *Research Applications*

Silver, in either the bulk metallic or nanoparticle state, is used in a number of industrial, medical, and commercial products (e.g., silver-zinc rechargeable batteries, and silver halide reference electrodes, surgical masks, odor reducing fabrics, solder, telecommunication equipment, and conductive pastes [1–6]), not to mention its popularity in jewelry and cutlery.

The antimicrobial activity of silver is very well-known [8–11]. This property is highly desirable for materials used in biomedical devices such as catheters, surgical

masks, and bandages [4,12,13]. For most industrial processes, and particularly biomedical uses, the chemistry at the silver surface, and especially aqueous-silver interfacial kinetics must be well understood.

This thesis is focused on the reactions of silver with halogens. There are several industrial applications of silver that depend on these reactions. These include the immobilization and timely release of radioiodine isotopes used for cancer therapies or diagnosis [14], and the filtration of airborne radioiodine from airstreams present in the nuclear industry [15,16]. Exposure of humans to radioiodines can be beneficial when administered carefully in calculated small doses [17,18]. Radioiodines are deliberately introduced into the body to treat or diagnose a number of thyroid-related diseases and for medical imaging purposes [17,18]. These purposes include investigating blood flow in the brain, detecting internal tumors, and imaging the urinary tract [14]. Iodine-131 and iodine-123 are the most commonly used isotopes in medical imaging [19]. They are produced either in a nuclear reactor or in a cyclotron by proton irradiation [20]. Once made, the isotopes of iodine begin to radioactively decay immediately, therefore management of the controlled capture, release, and delivery of these isotopes is critical if they are to be safely used as diagnostic or treatment agents.

Despite the widespread use of silver in a broad range of applications, there are very few studies that have investigated the interfacial reaction mechanisms and kinetics of silver-containing films.

The overall objective of this thesis is to establish the mechanism and kinetics of reactions involving the conversion of silver oxide (Ag_2O) to silver halide (AgX) in aqueous halide ($\text{X}^-(\text{aq})$) solutions, where $\text{X}^-(\text{aq})$ is the $\text{I}^-(\text{aq})$ or $\text{Br}^-(\text{aq})$ anion. The

incorporation of a halide ion into an oxide film or conversion from a metal oxide to a metal halide film can occur via different reaction pathways [21]. The protective properties of the resulting surface film depend on the pathway(s) that the conversion follows. The relative contributions of each reaction pathway to the overall film conversion will depend on the redox properties of the metal, and its oxide and halide, and the aqueous redox conditions. For example, for redox-active metals such as iron, the metal oxide is thermodynamically more stable than the metal halide [22], while for a noble metal such as silver, the metal halide is thermodynamically more stable than the metal oxide [21,22]. For iron it has been shown that metal halide formation requires a porous or defective oxide layer which exposes the base metal and leads to pitting corrosion [22]. Our research goal is to establish quantitative relationships between the redox properties of the silver/halide system, and the kinetics of the different reaction pathways for conversion of Ag_2O to AgX .

1.2.1 Atmospheric Corrosion of Silver

Silver possesses relatively high thermal and electrical conductivity and this has led to it being used in a number of commercial and industrial products. Any change in the electrochemical properties (e.g., conductance) of silver due to the formation of a surface corrosion film can negatively affect the function of an electronic part or device, especially since the sizes of many electronic devices have become smaller and more compact [23,24]. However, atmospheric corrosion rates of silver in urban, industrial, and marine conditions have not been extensively studied. Preliminary studies have shown that the corrosion rates are similar to those of aluminum and iron, less than that of zinc,

and much less than those observed on carbon steel [25]. Insight into the processes responsible for corrosion requires a detailed understanding of the relationship between the chemical properties of the oxidized silver surface and the atmospheric components responsible for the changes.

The potential–pH or Pourbaix diagram for silver is shown in Figure 1.1 [25]. The dashed line at more positive potentials is the reversible oxygen line and defines the O_2/H_2O equilibrium potential as a function of pH. The dashed line at less positive potentials is the reversible hydrogen line and defines the H_2/H_2O equilibrium potential as a function of pH. A Pourbaix diagram gives an indication of the thermodynamic stability of metal species at various combinations of potential and pH, but provides no kinetic information. Dry silver does not usually have a thick oxide layer present on the surface at ambient temperature and pressures (usually less than 100 nM [27]). The Pourbaix diagram shows that Ag_2O is only stable at a high pH (12–14) and in the presence of strong oxidizers.

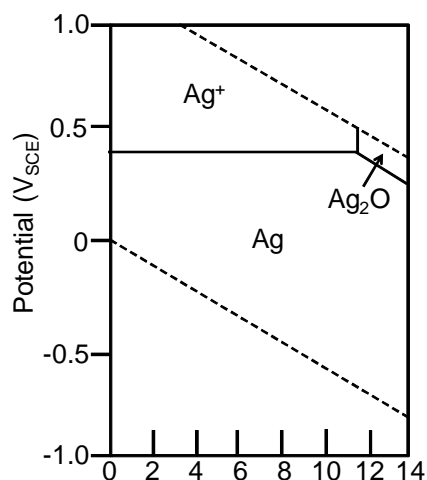


Figure 1.1 The potential-pH equilibrium diagram for Ag in H_2O at 25 °C. Figure is adopted from data found in [25].

One issue that is often not addressed when reporting atmospheric corrosion rates of silver is the poor correlation of corrosion rates measured in the laboratory compared to those measured in field exposure experiments. This discrepancy led Kelly et al. to pursue an investigation of the influence of UV radiation, relative humidity and exposure to ozone on the corrosion of silver [28]. The morphology and composition of the corrosion products were examined by scanning electron microscopy (SEM) and energy dispersive x-ray spectroscopy (EDX) and galvanostatic reduction measurements quantified the amount of each corrosion product. The main corrosion products were identified as Ag_2O and AgCl [28]. They determined that the combination of ozone and UV irradiation caused rapid degradation of the silver samples, while humidity had little impact on the corrosion process [28]. During their investigation an unexpected side reaction, namely the conversion of Ag_2O to AgCl , occurred [28]. This reaction was avoided by performing experiments in chloride-free sulphate solutions. This demonstrates how Ag film conversions and transformations are extremely sensitive to solution conditions. We have performed experiments in both buffered sodium phosphate, and un-buffered halide solutions to investigate the role of solution conditions (Chapter 4 and 5).

Only a few studies are published that examine the atmospheric corrosion of silver in outdoor environments after short (less than one year) exposure times [29]. In one study Watanabe et al. investigated the corrosion of silver exposed to an urban atmosphere for one month [29]. The corrosion products were characterized using x-ray diffraction (XRD) and x-ray fluorescence analysis. The XRD patterns revealed that two corrosion products, AgCl and Ag_2S , had formed on the silver samples over the one-month exposure period. They determined that the amount of AgCl that was formed was sensitive to

changes in sea-salt concentrations, and that more AgCl formed during the summer months compared to the winter months [29]. No seasonal differences were found for Ag₂S formation because the airborne concentration of H₂S and carbonyl sulfide did not change throughout the year [29].

While Watanabe et al. were successful in determining the chemical composition of the corrosion products formed on silver, the key chemical process or processes responsible for silver degradation were not reported. They speculated that AgCl formation occurred by the precipitation reaction of Ag⁺(aq), produced anodically at the Ag/H₂O interface, with dissolved Cl⁻(aq) anions [29]. However, very little information has been published on the rates of dissolution, precipitation, and transformation of silver-containing chemical species. We investigate the transformation or reaction rate of Ag₂O to AgI and AgBr and the results are discussed in Chapters 4–8.

1.2.2 Nuclear Reactor Accidents and the Release of Radioactive Materials

Measures that can limit the release of radioactive iodine into the environment are of particular interest to the nuclear industry. There are currently 440 nuclear reactors operating in 30 countries and these reactors produce almost 14% of the world's total electricity [30]. In Canada, there are 18 CANDU[®] reactors currently in operation (16 in Ontario, one in Quebec and one in New Brunswick) and these supply up to 52% of Ontario's electricity and 15% of Canada's electricity [30]. Nuclear energy has proven to be a reliable, clean, and economical energy source that does not contribute to conventional air pollution or green house gas emissions. However, accidents at the Chernobyl, Three Mile Island and the Fukushima Daiichi reactors demonstrate the

importance of the development and implementation of strategies that can limit releases of radioactive materials [31].

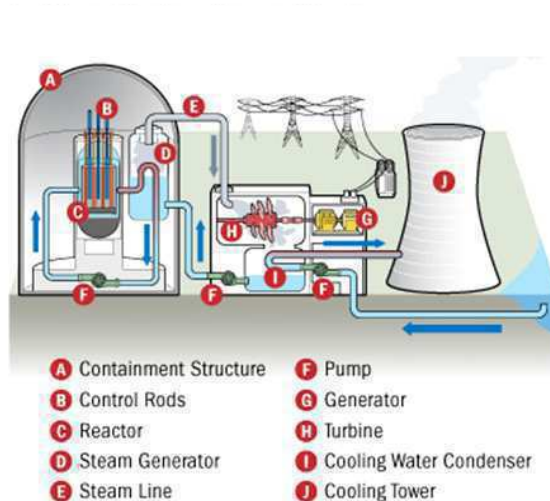


Figure 1.2. Schematic of the key components of a nuclear reactor which is adopted from [32].

The key components of a conventional nuclear power reactor are depicted in Figure 1.2 [32]. A nuclear power reactor works in the same way as a conventional fossil power plant; it produces heat to generate steam which then turns a turbine to generate electricity. The main difference between the two types of power plants is the fuel. In a nuclear power reactor, heat is generated by fission of uranium fuel. During the fission process a uranium atom nucleus splits into two smaller atomic fragments that are termed nuclear fission products. Fissioning of the fuel also produces a large release of energy, gamma rays and neutrons. The neutrons released from fission interact with additional uranium nuclei in a self-sustaining fission chain reaction. The fission fragments range in mass between 60 and 160 amu in a distribution with peaks at mass numbers around 90

and 140 amu [33]. The distribution of atomic fragments formed from the fission of ^{235}U is shown graphically in Figure 1.3. The peak at 140 contains a range of radioactive iodine isotopes (^{123}I to ^{129}I) plus stable ^{127}I .

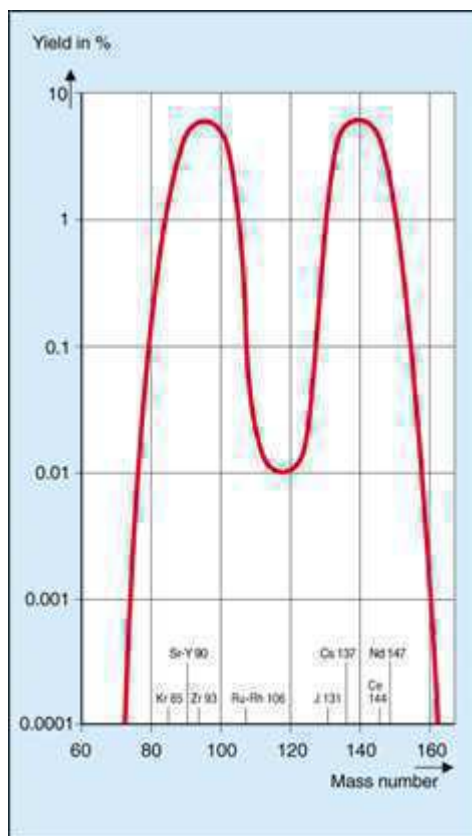


Figure 1.3. Fission yield, frequency distribution of the fission products generated in the fission of ^{235}U adopted from [33]

From the perspective of public safety, radioiodine is one of the most important fission products from the uranium fuel because its a radiological hazard [31,32]. Once radioiodine is released to the environment, human exposure to radioiodines can occur through inhalation, or ingestion after it enters the food chain [31]. Once iodine enters the body it rapidly accumulates in the thyroid gland where it can be a source of substantial

doses of beta radiation [35]. The primary biological consequence of radiation exposure is DNA damage [35]. Acute effects from high radiation doses include thyroiditis, while chronic and delayed effects include hypothyroidism, thyroid nodules, and thyroid cancer [35].

In the event of a severe nuclear reactor accident (an event where the reactor fuel overheats) a significant fraction of the radioiodine inventory in the nuclear reactor will be released from the reactor core (labeled “C” on Figure 1.2) into the containment building (labeled by “A” on Figure 1.2) [36–49]. Most of the released iodine would quickly dissolve and remain in the water that would be present throughout the containment building following an accident [36–39]. However, a small fraction of the iodine could be released to the gas phase due to the continuous conversion of non-volatile $\Gamma(\text{aq})$ in the water to volatile iodine species such as I_2 or CH_3I , under the oxidizing conditions prevailing in the water due to the presence of ionizing radiation [40,43]. This is shown schematically in Figure 1.4. Because of its mobility, control and prevention of release of the airborne iodine is critical for safety and post-accident management. One of the methods used to control and limit airborne radioiodine release is air filtration with deep zeolites that are impregnated with silver [15,16].

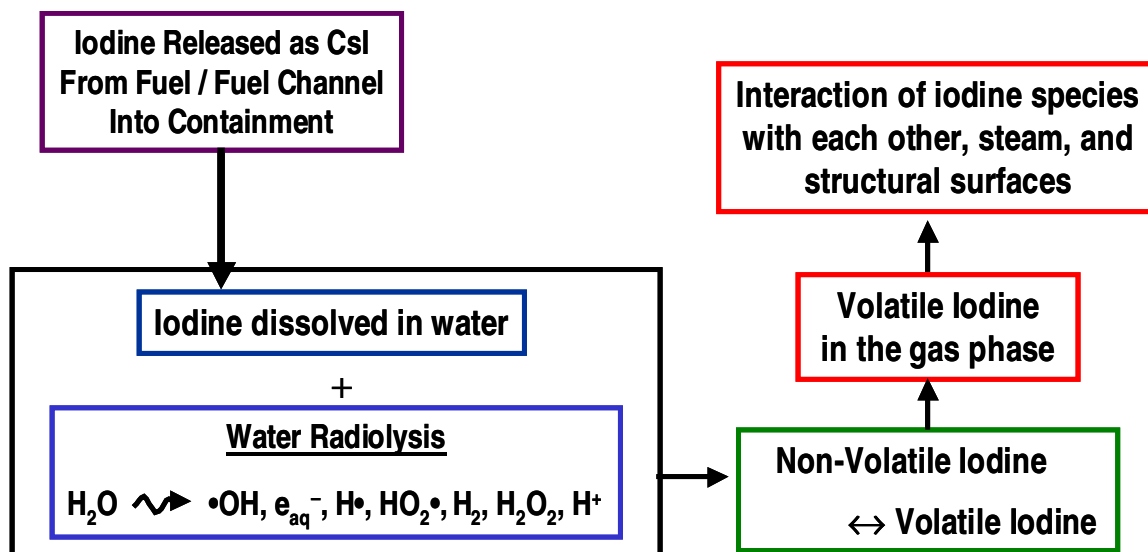


Figure 1.4 Transport flow paths of iodine for CANDU reactor under accident conditions.

A means of controlling airborne radioiodine generation during a reactor accident is immobilization of the iodide in the water by reaction with a metal to produce an insoluble halide. Silver is a candidate material for such a process. Results from large-scale experiments that simulate severe accident conditions have shown that the formation of volatile iodine species is suppressed when silver is present [42,44,46,48,49]. This silver is naturally released from the melting of AgInCd control rods (“B” in Figure 1.2) that are used in some reactor designs [50]. These control rods maintain an appropriate level of the fission chain reaction neutrons. Control rods can be made of various materials, one silver-cadmium-indium alloy (80%, 15%, and 5% by weight) is used in Pressurized Water Reactors and Boiling Water Reactors [50]. In some accident scenarios reactions of silver from these alloys with aqueous iodine to form insoluble silver iodide could dominate iodine behaviour in solution [42,46].

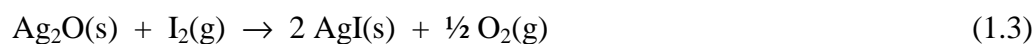
Because there will be a high radiation field present in a containment building during a severe accident, the silver in the water will be exposed to oxidizing conditions driven by ionizing radiation that is present [36-49]. Hence, while Ag could enter the aqueous phase in the metallic state, it can be expected to grow an oxide (AgOH, Ag₂O or AgO) surface film. To assess the availability of volatile radioiodine under severe accident conditions, it is important to establish the mechanism and kinetics of individual iodine reactions with silver/silver oxide. Knowledge of the reaction kinetics is also important in understanding the immobilization of iodine on silver surfaces impregnated on filtration materials, since the filters are most likely to operate under conditions where high humidity in the filtered air will lead to moisture condensation on the silver surfaces.

Due to this ability of silver to immobilize iodine by forming an insoluble solid it has been suggested that silver be deliberately added to the aqueous phase following an accident, or incorporated into barriers to prevent radioiodine release from nuclear waste management facilities [15,16].

Early studies on silver-iodine interactions involved measurements of overall iodine uptake on silver as a function of pH and the extent of initial Ag oxidation, in either the presence or absence of radiation [42,44,46,48,49]. The results suggested that the uptake involves the interaction of I⁻(aq) with Ag₂O:

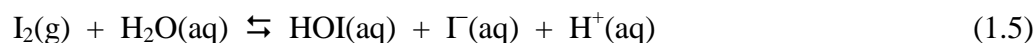


and the reaction of I₂ with both metallic Ag and Ag₂O:



However, these studies have not unambiguously established detailed mechanisms and kinetics of the individual reactions [42,44,46,48,49].

A complication to interpretation of previous experimental results is the pseudo-steady state that exists between $\Gamma(\text{aq})$ and $\text{I}_2(\text{aq})$ in the aqueous solution [37,39,40]:



Equilibria (1.5) and (1.6) are achieved thermally even in the absence of radiation.

The formation of AgI can occur by the reaction of Ag_2O with $\Gamma(\text{aq})$ (equation 1.1) or Ag with I_2 (equation 1.2). Since the goal of this work was to determine the mechanism and kinetics of the individual reactions that are most important in solution only the reaction involving Ag_2O and $\Gamma(\text{aq})$ has been studied. The reaction between aqueous $\Gamma(\text{aq})$ and the solid $\text{Ag}_2\text{O}/\text{Ag}$ surface can occur via three reaction pathways:

1. Chemical reaction at the oxide/aqueous (ox/aq) interface (Figure 1.5). This is a molecule-molecule interaction that does not involve charge transport in the solid:



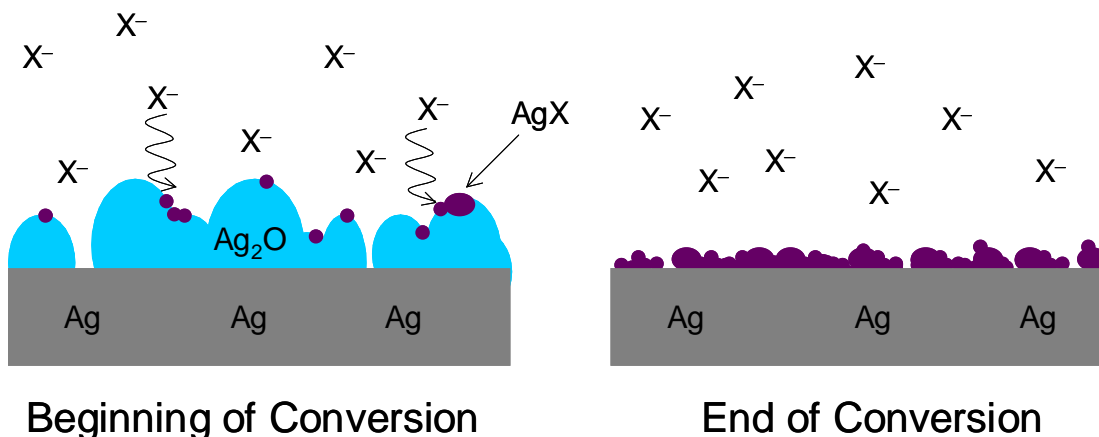


Figure 1.5 Schematic representation of the Ag electrode surface at the beginning and end of the surface chemical reaction.

2. Electrochemical (termed galvanic coupling hereafter) reaction in which reduction of Ag_2O to Ag in the solid surface 'oxide' phase (ox) is coupled with oxidation of Ag + $\text{X}^-(\text{aq})$ to AgX at the Ag metal/water (m/aq) interface (Figure 1.6):

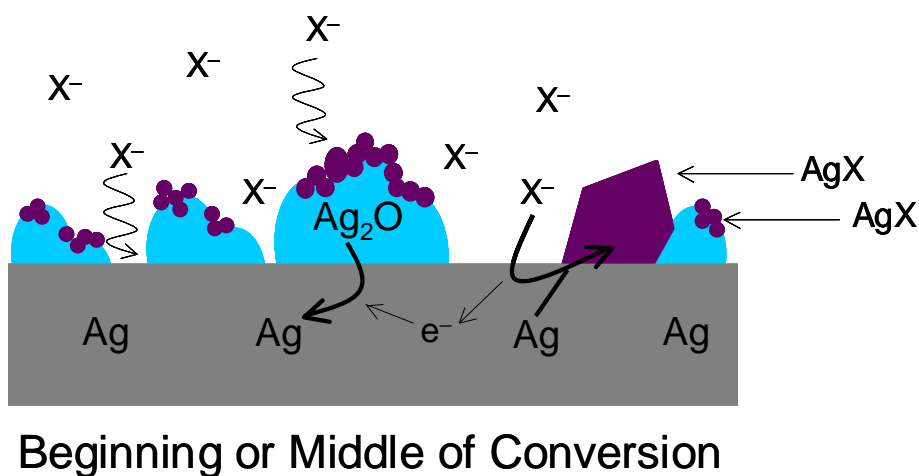
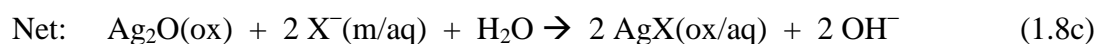
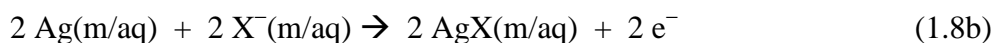
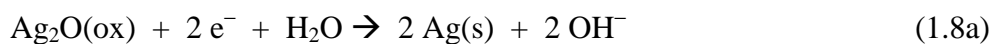
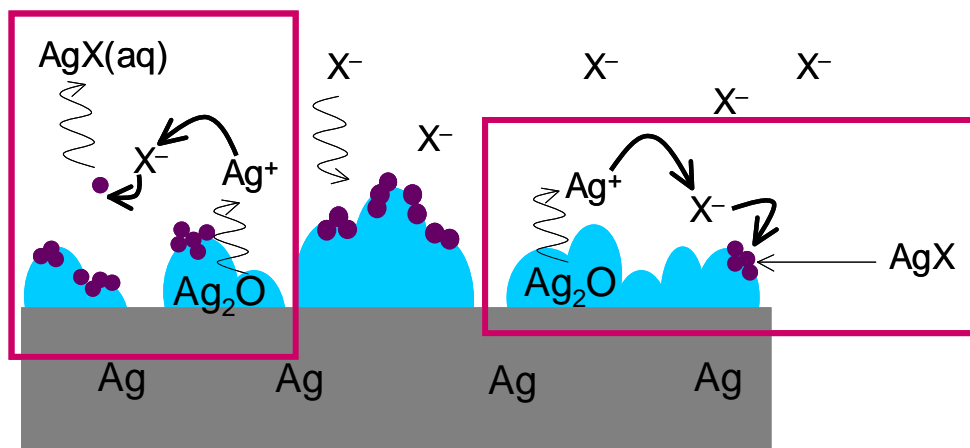
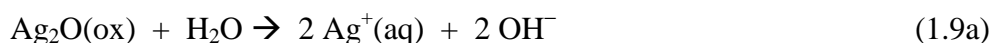


Figure 1.6 Schematic representation of the galvanic coupling reaction described in equations (1.8a-c).

This electrochemical reaction requires charge transport through the bulk solid phases, i.e., the silver substrate and/or the silver oxide film lattice. The charge transport can be accomplished by migration of electrons, ions and/or ion vacancies. This reaction will depend on the electrochemical potential at the Ag/Ag₂O and Ag₂O/solution interfaces.

3. Dissolution of Ag⁺(aq) from Ag₂O(ox), followed by the diffusion of Ag⁺(aq) into the bulk aqueous phase (Figure 1.7). Some dissolved Ag⁺(aq) will react with X⁻(aq) to form AgX(aq) in the aqueous phase, which will then migrate away from the interface region to the bulk aqueous phase or re-settle on the electrode surface.



Beginning or Middle of Conversion

Figure 1.7 Schematic representation of the dissolution reaction pathway.

All three pathways lead to the formation of solid AgX on the Ag₂O surface.

However, the nature (size and morphology) of the solid film formed by the different

pathways will be different. The competing rates of the different reaction pathways are very important since the fastest reaction pathway will determine the nature of the AgX film that is formed. Which reaction pathway dominates is expected to depend on parameters such as the difference between the equilibrium potentials of the Ag/Ag₂O and Ag/AgX redox pairs, oxide and halide film morphologies and thickness, film compositions and solid crystallinities, cation and anion oxidation states, or solution redox conditions. The properties of the surface film that is formed is an important factor controlling corrosion kinetics. Thus, if we can determine how the dominant conversion pathway changes with respect to the chemical/electrochemical environment, the information can be used for corrosion control.

This study on the reaction of Ag₂O with $\Gamma^-(aq)$ echoes a related study by Smith et al. [51]. The kinetic model that is described in Chapter 4 was applied by Smith et al. to their investigation of the conversion of copper oxide (Cu₂O) to copper sulphide (Cu₂S). Copper has been proposed as the material of choice for the fabrication of nuclear waste containers since it is thermodynamically stable under the saline, anoxic conditions that are expected to be present in a nuclear waste repository over the majority of the container lifetime [52]. Destabilization of Cu by conversion to Cu₂S sulphide appears to be the only feasible long-term corrosion process for Cu waste containers [53,54]. Due to an initial period of oxic corrosion, a copper container surface will be covered with a thin oxide/hydroxide/Cu^{II} film that can chemically react with dissolved sulphide ions (S²⁻) that are generated in groundwater by microbes. The primary goal of Smith et al.'s research was to determine whether films formed during the initial repository oxic period can subsequently inhibit, and perhaps even prevent, reaction with sulphide [51]. Hence

they had an objective similar to our objective of understanding the kinetics of AgI formation and iodine immobilization.

1.3 Experimental Approach

Investigation of the kinetics of aqueous–solid interfacial reactions often requires either very cumbersome measurements (such as drying and weighing of the solid reactant or products formed as a function of reaction time [55]) or sophisticated and expensive surface analyses [56]. Studies of redox surface reactions are exceptions, since they involve interfacial-charge-transfer reactions and, hence, their reaction kinetics can be followed by current measurement using an appropriate electrochemical cell arrangement. Highly sensitive current measurement-based techniques do not work very well for studying purely chemical (molecule–molecule) interactions on surfaces because they do not generate any current. However, for such reactions, potentiometric electrodes that are sensitive to changes in the activity of either the reactant or the product can be used to follow the reaction kinetics. One example of a potentiometric electrode is the conventional platinum hydrogen electrode that is widely used for acid–base titrations [57,58]. In this work a specific form of this potentiometric approach is used. During the course of the conversion reaction, the measurements change from one sensor system ($\text{Ag}|\text{Ag}_2\text{O}|\text{H}_2\text{O}$) to another ($\text{Ag}|\text{AgI}|\text{X}^-(\text{aq})$).

1.4 Thesis Organization

This thesis contains nine chapters. Chapter 1 briefly introduces the thesis topic and the research objectives. Chapter 2 contains background information and the general

experimental methods utilized for the generation of data presented in this thesis.

Experimental details specific to Chapters 4–8 can be found at the beginning of each of these chapters. In Chapter 3, the electrochemical behaviour of silver oxide and silver halide films is investigated. The results of Chapter 3 were used in the development of an experimental approach that allowed us to determine the kinetic parameters (i.e., reaction orders and reaction rate constant) for the chemical conversion of silver oxide to silver iodide (Chapter 4). The influence of solution composition and mass-transport contributions to the chemical kinetics are presented in Chapters 4 and 5, and a revised method to determine the surface reaction rate constant is reported. Chapter 6 documents an additional study of the interfacial reaction kinetics of Ag_2O with $\Gamma(\text{aq})$ using *in situ* neutron reflectometry. The kinetics of the conversion of Ag_2O to AgBr are analyzed in Chapter 7 using the electrochemical analysis methods developed in Chapters 4 and 5. The results show that the contributions of the possible conversion pathways to the overall conversion rate are different for the $\Gamma(\text{aq})$ and $\text{Br}^-(\text{aq})$ systems (Chapter 8). The thesis concludes with a short summary of Chapters 3–8, and future experiments are suggested.

1.5 References

1. T.W. Purcell, and J.J. Peters, *Environ. Tox. Chem.*, **17**, 539 (1998).
2. I.R. Gould, J.R. Lenhard, A.A. Muentner, S.A. Godleski, and S. Farid, *J. Am. Chem. Soc.*, **122**, 11934 (2000).
3. D.J.G Ives, G.J. Janz, *Reference Electrodes*, Academic Press, New York, 1961, pp.54, 184.
4. Y. Li, P. Leung, L. Yao, Q.W. Song, and E. Newton, *J. Hosp. Infec.*, **62**, 58 (2006).
5. T.M. Benn, and P. Westerhoff, *Environ. Sci. Technol.*, **42**, 4133 (2008).

6. K.S. Park, J.T. Son, H.T. Chung, S.J. Kim, C.H. Lee, K.T. Kang, and H.G. Kim, *Solid State Commun.*, **129**, 311 (2004).
7. G. Gosh, *Acta Materialia*, **49**, 2609 (2001).
8. A.D. Russel, W.B. Hugo, *Prog. Med. Chem.*, **31**, 351 (1994).
9. C.P. Zachariadis, S.K. Hadjikakuo, N. Hadjiliadis, S. Skoulika, A. Michaelides, J. Balzarini, E. De Clercq, *Sci. Technol.*, **7**, 1420 (2004).
10. X. Wu, H. Liu, J. Liu, K.N. Haley, J.A. treadway, J.P. Larson, E. Ge, F. Pearle, M.P. Bruchez, *Nat. Biotechnol.*, **21**, 41 (1993).
11. K.B. Holt, and A.J. Bard, *Biotechnol.*, **44**, 13214 (2005).
12. K. Nomiya, K. Tsudah, and M. Gala, *J. Inorg. Biochem.*, **68**, 39 (1997).
13. R. Rai, A. Yadav, and A Gade, *Biotechnol. Adv.*, **27**, 76 (2009).
14. A.B. Brill, M. Stabin, A. Bouville, and E. Ron, *Rad. Research*, **166**, 128 (2006).
15. K.W. Chapman, P.J. Chupas, and T.M. Nenoff, *J. Am. Chem. Soc.*, **132**, 8897 (2010).
16. H. Faghihian, M. Ghannadi Maragheh, and A. Malekpour, *J. Radioanal. Nucl. Chem.*, **254**, 545 (2002).
17. M.J. O'Doherty, T.O. Nunan, and D.N. Croft, *Nucl. Med. Commun.*, **14**, 736 (1993).
18. W.J.G. Oyen, L. Bodei, F. Giammanie, H.R. Maecke, J. Tennvall, M. Luster, and B. Brans, *Annals of Oncology*, **18**, 1782 (2007).
19. O.W. Press, J.F. Eary, F.R. Applebaum, P.J. Martin, C.C. Badger, W.B. Nelp, S. Glenn, G. Butchko, D. Fisher, B. Porter, D.C. Matthews, L.D. Fisher, and I.D. Bernstein, *N. Eng. J. Med.*, **329**, 1219 (1993).
20. D.J. Schyler, *Production of Radioactive Iodine*, Technical Meeting of Project Counterparts on Cyclotron Production of Iodine-123, Institute of Nuclear and Energy Research, BNL-68599, Aug. 8, 2001, pp. 1-14.
21. X. Zhang, S.D. Stewart, D.W. Shoesmith, and J.C. Wren, *J. Electrochem. Soc.*, **154**, F70 (2007).
22. K. Yazdanfar, X. Zhang, P.G. Keech, D.W. Shoesmith, J.C. Wren, *Corr. Sci.*, **52**, 1297 (2010).
23. M. Watanabe, M. Tomita, T. Ichino, *J. Electrochem. Soc.*, **148**, B522 (2001).

24. E. Toyoda, M. Watanabe, Y. Higashi, T. Tanaka, Y. Miyata, T. Ichino, *Corrosion*, **60**, 729 (2004).
25. E. Mattsson, *Mater. Perf.*, **21**, 9 (1982).
26. T.E. Graedel, *J. Electrochem. Soc.*, **139**, 1963 (1992).
27. D.E. Davies, *Nature*, **179**, 1293 (1969).
28. Z.Y. Chen, D. Liang, G. Ma, G.S. Frankel, H.C. Allen, and R.G. Kelly, *Corr. Eng. Sci. Technol.*, **45**, 169 (2010).
29. M. Watanabe, S. Shinozaki, E. Toyoda, K. Asakura, T. Ichino, N. Kuwaki, Y. Higashi, and T. Tanaka, *Corrosion*, **62**, 243 (2006).
30. “*Energy, Electricity and Nuclear Power Estimates for the Period up to 2050*”. Vienna: International Atomic Energy Agency, 2011. (IAEA publication no. 978–92–0–119410–7).
31. J.P. Christodouleas, R.D. Forrest, C.G. Ainsley, Z. Tochner, S.M. Hahn, E. Glastein, *N. Eng. J. Med.*, **364**, 2334 (2011).
32. <http://science.howstuffworks.com/nuclear-reactor2.htm>
33. <http://www.euronuclear.org/info/encyclopedia/f/fissionyield.htm>.
34. Y. Shibata, S. Yamashita, V.B. Masyakin, G.D Panasyuk, S. Nagataki, , *Lancet*, **358**, 1965 (2001).
35. “Follow up of delayed health consequences of acute accidental radiation exposure”. Vienna: International Atomic Energy Agency, 2002. (IAEA publication no. IAEA-TECDOC-1300).
36. G.W. Parker and C.J. Barton, *Fission Product Release. The Technology of Nuclear Reactor Safety*, **2**, The M.I.T. Press, Cambridge, Mass (1973).
37. F. Garisto, R.J. Lemire, J. Paquette, P.P.S. Saluja, S. Sunder, D.F. Torgerson, A.C. Vikis, D.J. Wren, and J.C. Wren, in *Radioiodine Chemistry in Reactor Accident Conditions*, ISBN 92-0-020086-9, p. 501, Proceedings Series of an International Symposium on Source Term Evaluation for Accident Conditions, Columbus, OH (1986).
38. L. Soffer, S.B. Burson, and C.M. Ferrell, R.Y. Lee, and J.N. Ridgely, in *Accident Source Terms for Light-Water Nuclear Power Plants*, NUREG-1465GAR, **95(13)**, Washington, DC (1995).

39. J. McFarlane, J.C. Wren, and R.J. Lemire, *Nucl. Tech.*, **138**, 162 (2002).
40. J.C. Wren, J.M. Ball, G.A. Glowa, *Nucl. Tech.*, **129**, 297 (2000).
41. D. Jacquemain, N. Hanniet, C. Poletiko, S. Dickinson, C. Wren, D.A. Powers, E. Krausmann, F. Funke, R. Cripps, and B. Herrero, in *An Overview of the Iodine Behaviour in the Two First PHEBUS Tests FPT-0 and FPT-1*, NEA/CSI/R(99)7, p.57, Proceedings of the OECD Workshop on Iodine Aspects of Severe Accident Management, Vantaa, Finland (1999).
42. N. Girault, S. Dickinson, F. Funke, A. Auvinen, L. Herranz, and E. Krausmann, *Nuc. Eng. Des.*, **236**, 1293 (2006).
43. F. Funke, G.U. Greger, A. Bleier, S. Hellman, and W. Morell, in *The Reaction Between Iodine and Silver Under Sever PWR Accident Conditions- An Experimental Parameter Study*, PSI-Bericht, Editors, NEA/CSNI/R(96)6, Proceedings of The 4th CSNI Workshop on the Chemistry of Iodine in Reactor Safety, Wurenlingen, Switzerland (1996).
44. E. Krausemann, and Y. Drossinos, *J. Nucl. Mater.*, **264**, 113 (1999).
45. C.C. Lin, and J.H. Chao, *J. Nucl. Sci. Technol.*, **46**, 1023 (2009).
46. L. Sepold, T. Lind, A. Pintér Csordás, U. Stegmaier, M. Steinbrück, and J. Struckert, *Annals Nucl. Energy*, **36**, 1349 (2009).
47. H. Glänneskog, J.O. Liljenzin, and L. Sihver, *J. Nucl. Mater.*, **348**, 87 (2006).
48. L. Bosland, F. Funke, N. Girault, and G. Langrock, *Nucl. Eng. Des.*, **238**, 3542 (2008).
49. S. Güntay, R.C. Cripps, B. Jäckel, and H. Bruchertseifer, *Nucl. Technol.*, **150**, 303 (2005).
50. E.A. Lepel, S.L. Pratt, D.E. Robertson, C.W. Thomas, and D.L. Haggard, *J. Radioanal. Nucl. Chem.*, **194**, 81 (1995).
51. J.M. Smith, J.C. Wren, M. Odziemkowski, D.W. Shoesmith, *J. Electrochem. Soc.*, **154**, C431-C438 (2007).
52. I. Puigdomenech and C. Taxen, *SKB Swedish Nuclear Fuel and Waste Management Co.*, Technical Report TR-00-13 (2000).
53. SKB, *Deep Repository for Spent Nuclear Fuel*, SR 97–Post Closure Safety TR-99-06 (1999).
54. M. Pourbaix and A. Pourbaix, *Geochim. Cosmochim. Acta*, **56**, 3157 (1992).

55. A. Popova, E. Sokolova, S. Raicheva, and M. Christov, *Corro. Sci.*, **45**, 33 (2003).
56. D. Koeppenkastrop, and E.H. De Carlo, *Environ. Sci. Technol.*, **27**, 1796 (1993).
57. M.Cremer, *Z. Brol (Munich)*, **47**, 562 (1906).
58. W.S. Hughes, *J. Am. Chem. Soc.*, **44**, 2860 (1922).

Chapter 2

Experimental Principles and Details

This chapter includes general information regarding the various experimental techniques employed in this thesis project. It also includes experimental procedures that are common to all experiments. Additional experimental details will be provided, as necessary, immediately prior to the discussion of results in later chapters.

2.1 *Experimental Set-Up*

2.1.1 *Electrochemical Cell*

In an electrochemical cell where current is allowed to flow between two electrodes, the current will polarize both electrodes in response to the reactions occurring on the electrodes. To address this problem, the cell contains separate reference and counter electrodes. A potentiostat is used to allow a very low current to flow through the reference electrode, as its only role is to act as a reference point against which the potential of the working electrode can be measured or controlled. The current passed at the working electrode is balanced by a current flow through the counter electrode. This arrangement of a working electrode (WE), a reference electrode (RE) and a counter (CE) is shown in Figure 2.1.

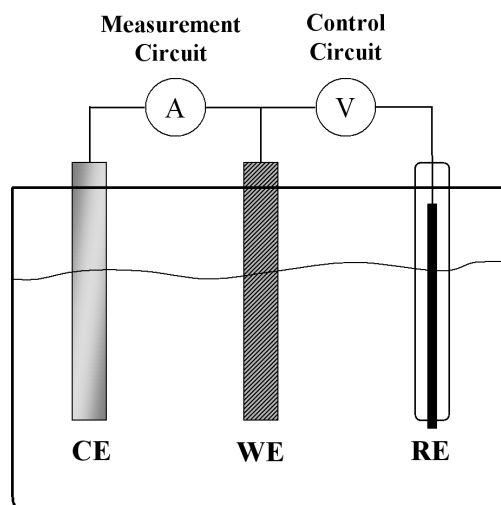


Figure 2.1 Schematic of a three-electrode cell setup.

For this work all electrochemical experiments were performed in a Pyrex cell using this conventional three-electrode configuration. The counter electrode was made by spot welding a 2 cm \times 2 cm platinum sheet to 1 mm diameter platinum wire (99.95% purity). The wire was used to connect the electrode to the measurement equipment. Platinum is chosen for the counter electrode because it is quite inert and will not oxidize or dissolve under the conditions of the experiments. It is known to readily sustain water oxidation/reduction reactions. The reference electrode was a commercially available saturated calomel electrode from Fisher Scientific. A saturated calomel electrode (SCE) provides a reference potential that is +241 mV with respect to the standard hydrogen electrode (SHE).

Electrochemical measurements were made with a Solartron 1480 multistat or a Solartron 1287 potentiostat running Corrware software (version 3, Scribner Inc.). Rotating disc experiments were performed using a rotator produced by Pine Instruments Inc.

2.1.2 *Solution Preparation*

Electrolyte solutions were prepared from ultra-pure deionized water with a resistivity of 18.2 M Ω -cm. The water was obtained from a NANOpure Diamond UV ultra-pure water system (Barnstead International). Reagent grade chemicals from a variety of sources were used to make up the electrolyte solutions to the desired concentrations. To achieve anoxic conditions in the electrolyte, solutions were deaerated by purging with ultra high purity argon gas for a minimum of 60 min prior to, and then during, all experiments.

2.1.3 *Sample Preparation*

Working electrodes were made by machining discs from a silver rod (area of 0.385 cm²) obtained from Goodfellow Cambridge Limited (99.99 % purity). To provide an electrical contact, a stainless steel rod was threaded into the back of the silver disc. The electrodes were then wrapped with polytetrafluoroethylene (PTFE) tape and Parafilm® or bonded in cylindrical PTFE holders with epoxy resin to allow only one face of the electrode to contact the electrolyte as shown in Figure 2.2.

Prior to an experiment, the silver electrode was polished with incremental grades of silicon carbide paper (500, 800, 1000, 1200 grit). The electrode was then rinsed, sonicated in deionized water to remove any remaining polishing residue and rinsed again. After placement in the electrochemical cell, the silver working electrodes were cathodically cleaned by polarizing the electrode at $-1.1 V_{SCE}$ for 300 s. This removed

any air-formed oxides and ensured that all experiments started with a reproducible surface of pure Ag.

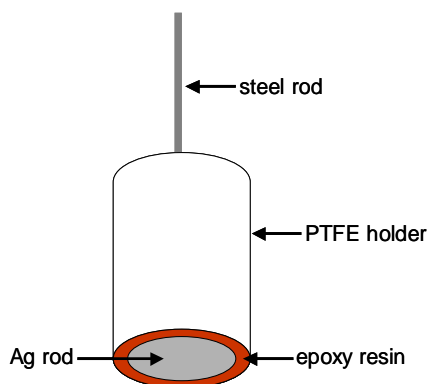


Figure 2.2 Schematic of an assembled silver working electrode.

2.2 *Electrochemical Reactions at an Electrode Surface*

Electrochemical reactions are redox (reduction-oxidation) reactions occurring on the surface of an electronic conductor (electrode) in contact with an ionically conducting medium. In considering the thermodynamics and kinetics of such reactions, it is often quite useful to separate the reaction into “half-reactions” by isolating the components participating in the oxidative part of the overall reaction from those participating in the reductive part to yield respectively an anodic half-reaction and a cathodic half-reaction. In the half-reactions, electrons are explicitly specified as a charge-balancing reactant or product. The main convenience afforded by half-reactions is that they can be used in a “mix and match” fashion to compare various overall redox reactions while allowing what is known about the thermodynamic and kinetics of each half-reaction to be used independently of the other half-reaction with which it might be paired [1–6].

The thermodynamics of electrochemical reactions are much like those of other chemical reactions, with the addition that, for electrochemical reactions, one must also

consider the energetics of moving charges species (electrons or ions) through the electric field that resides at charged phase boundaries. Therefore, the free energy change in an electrochemical half-reaction is potential-dependent, as given by [1,5]

$$\Delta_r G = -nFE \quad (2.1)$$

where $\Delta_r G$ is the free energy change of the reaction, n the number of equivalent electrons transferred in the reaction, F the Faraday constant ($96\,485\text{ C}\cdot\text{mol}^{-1}$), and E the electrochemical potential difference between the electrode surface at which the reaction (half-reaction) in question is taking place and the defined standard reference potential. That is, we consider the free energy change for an overall redox reaction in which one half-reaction is the half-reaction of interest and the other is, by convention,



where this reaction represents the reaction taking place on the Standard Hydrogen Electrode (SHE) (Pt at $25\text{ }^\circ\text{C}$ in solution with $a_{\text{H}^+} = 1$ and $P_{\text{H}_2} = 1\text{ atm}$). The latter half-reaction has been chosen as the zero or reference point for the potential scale ($E_{\text{SHE}} = 0$). The thermodynamics of any half-reaction can then be described in terms of a potential (which, strictly is a potential difference from $E_{\text{SHE}} = 0$). The thermodynamics of any overall redox reaction can, in turn, be evaluated from the difference between the potentials (vs. SHE) determined for each half-reaction involved.

The dependence of the free energy change on reactant and product concentrations and temperature in chemical reactions is given by the Van't Hoff Isotherm [5],

$$\Delta_r G = \Delta_r G^\circ + RT \ln K_{\text{eq}} \quad (2.3)$$

where $\Delta_r G^\circ$ is the standard free energy change for the reaction (i.e., for the reaction occurring under standard conditions), R the Universal Gas Constant ($8.314 \text{ J}\cdot\text{K}^{-1}\cdot\text{mol}^{-1}$), T the absolute temperature, and K_{eq} the equilibrium constant for the reaction.

Substituting equation 2.1 into 2.3 allows us to convert the Van't Hoff Isotherm into the electrochemical equivalent, known as the Nernst equation,

$$E^e = E^\circ - \frac{RT}{nF} \ln K_{eq} \quad (2.4)$$

where E^e is the equilibrium potential for the half-reaction of interest (vs. SHE) and E° is the Standard Potential (i.e., the equilibrium potential for the half-reaction under standard conditions, $\Delta_r G^\circ = -nFE^\circ$) [7]. To connect this directly with the activities (concentrations) of reactants and products involved, note that for a reaction,



$$K_{eq} = \frac{a_C^c a_D^d}{a_A^a a_B^b} \quad (2.6)$$

where a_X is the activity of species X. This can be incorporated into the Nernst equation to give:

$$E^e = E^\circ - \frac{RT}{nF} \ln \left(\frac{a_C^c a_D^d}{a_A^a a_B^b} \right) \quad (2.7)$$

Note also that the convention for redox half-reactions is to express them in the form of a reduction reaction (electrons on the left side) to yield the usual sign convention for the potential [1,5].

When an electrode is placed in a solution with a redox couple present and without an external power supply or current source/pathway, it will spontaneously react such that the free energy decreases and the systems heads toward equilibrium. After an initial

charge transfer between electrode and solution (a very small number of charges) an electric field develops at the electrode-solution interface, which then prevents any further uncompensated charge transfer between them. From that point, any charge transfer between electrode and solution species must conserve charge so that no further charge separation occurs. That means that for every oxidation occurring on that surface, a charge-equivalent reduction must also occur on that surface. No current is measurable because there is no current pathway through an external measurement device and there is no current generated by the reaction since all electrons produced in the oxidation half-reaction are consumed in the reduction half-reaction. This means that the partial anodic current generated by the oxidation half-reaction, i_A , is equal in magnitude to the partial cathodic current generated by the coupled reduction half-reaction, i_C , such that they sum to zero:

$$i_A = |i_C| \quad (2.8)$$

$$i_A + i_C = 0 \quad (2.9)$$

A specific term is given to the partial current magnitude at the equilibrium condition; it is called the “exchange current”, i_o , and is a measure of the dynamics underlying the equilibrium state. The electrode potential measured in this case is E^e . The term “open circuit” is used to describe an electrode isolated from external current pathways, and the potential achieved under the open circuit condition is called the open circuit potential, E_{OC} [1–6].

In the case where an electrode is immersed in a solution in which an ongoing redox reaction can occur spontaneously (e.g., a corrosion situation) the open circuit potential is not an equilibrium potential ($E_{OC} \neq E^e$). Yet still, if the electrode has no

available external current pathway (i.e., it is at open circuit) the requirement for charge conservation, implying that no net current must flow, implies that the potential will establish a value (usually the only value) of which this condition is satisfied for the existing conditions (i.e., $i_A = |i_C|$, $i_A + i_C = 0$). In corrosion reactions, this open circuit potential is established by the oxidative and reductive half-reactions of a corrosion process, so it is given the special name “corrosion potential,” E_{Corr} (i.e., $E_{\text{OC}} = E_{\text{Corr}}$).

The magnitude of the underlying partial anodic and cathodic currents is also specifically named the “corrosion current,” i_{Corr} (i.e., $i_A = |i_C| = i_{\text{Corr}}$). The corrosion current is directly proportional to the rate of the corrosion reaction. Since it cannot be measured directly (net current at E_{Corr} is zero), several methods (Chapter 8) have been developed to evaluate this important parameter [1,9–11].

The forward rate, \bar{v} , of a simple first-order redox half-reaction, for example



is proportional to the activity of the reacting species

$$\bar{v} = \bar{k} a_{\text{ox}} \quad (2.11)$$

where \bar{k} is the constant of proportionality, known as the “rate constant”. In electrochemical terms, the rate is expressed in the form of a current

$$\bar{i} = -nF\bar{k} a_{\text{ox}} \quad (2.12)$$

Furthermore, in electrochemical reactions the rate constant is potential-dependent (analogous to the temperature dependence of the rate constant of thermal reactions via the activation barrier as described by the Arrhenius expression). Therefore,

$$\bar{k} = \bar{k}_o \exp\left(-\frac{\bar{\alpha}nF\eta}{RT}\right) \quad (2.13)$$

where \bar{k}_o is the pre-exponential factor, $\bar{\alpha}_o$ is the symmetry coefficient (describes the symmetry of the activation barrier to the forward and reverse reactions), and η is the “overpotential” or shift of the electrode potential from the equilibrium potential value, i.e.,

$$\eta = E - E^\circ \quad (2.14)$$

Analogous rate and rate constant expressions can be defined for the reverse reaction (2.10), and by summing the kinetic relationships for the forward and reverse half-reactions, the net current can be expressed as:

$$i = i_o \left[\exp\left(\frac{\bar{\alpha}nF\eta}{RT}\right) - \exp\left(-\frac{\bar{\alpha}nF\eta}{RT}\right) \right] \quad (2.15)$$

where $\bar{\alpha}$ and $\bar{\alpha}$ are the symmetry coefficients for the half-reactions proceeding in the reverse (anodic) and forward (cathodic) directions, respectively ($\bar{\alpha} + \bar{\alpha} = 1$). This is the Butler-Volmer equation [12]. It describes the measured current as a function of applied overpotential for a given half-reaction. It is represented graphically as shown in Figure 2.3. Inspection of equation 2.15 indicates that for large positive overpotentials, the second exponential term rapidly diminishes to a negligible magnitude and the reaction is dominated by the oxidation described by the first (anodic) term. Likewise, at large negative overpotentials, the second (cathodic) exponential term dominates the equation, the first (anodic) term diminishes to a negligible amount and the nature of the reaction is almost entirely cathodic (reduction).

In the case of a corroding electrode, two different half-reactions are proceeding on the same electrode at E_{OC} . Each half-reaction is independently described by its own unique Butler-Volmer equation. The net observable current-potential relationship is

easily obtained from the sum of the two simultaneous Butler-Volmer equations. The proposed name of this summary equation is the Wagner-Traud equation [9–11]. The Wagner-Traud equation is given by

$$i = i_{Corr} \left[\exp\left(\frac{\alpha_A nF}{RT}(E - E_{OC})\right) - \exp\left(-\frac{\alpha_C nF}{RT}(E - E_{OC})\right) \right] \quad (2.16)$$

where α_A is the anodic transfer coefficient and α_C the cathodic transfer coefficient.

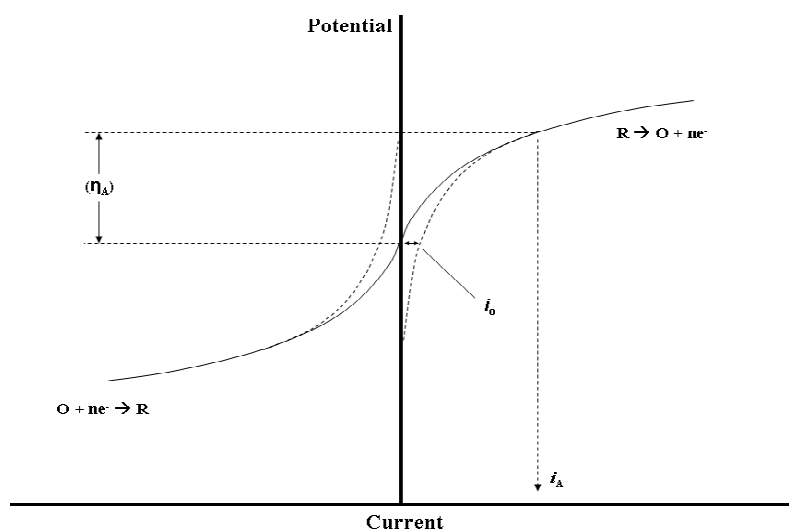


Figure 2.3 Current-potential relationship for a redox active species [6].

The form of the Wagner-Traud equation is similar to that of the Butler-Volmer equation, and it has some of the same properties/features. The transfer coefficients are similar to the symmetry coefficients, though in this case they correspond to activation barriers from two different half-reactions. The analogy between i_0 and i_{Corr} has already been described above. The difference $E - E_{OC}$ is akin to the overpotential η but now represents the degree of polarization away from the open circuit, rather than the equilibrium potential, E^e . Also, it can be seen that at large polarizations positive of E_{OC} ($E - E_{OC} \gg 0$) the first (anodic) term of the Wagner-Traud equation dominates and the net

current is anodic, whereas at large polarizations negative of E_{OC} ($E - E_{OC} \gg 0$), the second (cathodic) term of the Wagner-Traud equation dominates and the net current is cathodic. The summing of two Butler-Volmer equations and the form of the Wagner-Traud equation are illustrated graphically in Figure 2.4. The use and implications of the Wagner-Traud equation are further discussed in Chapter 8.

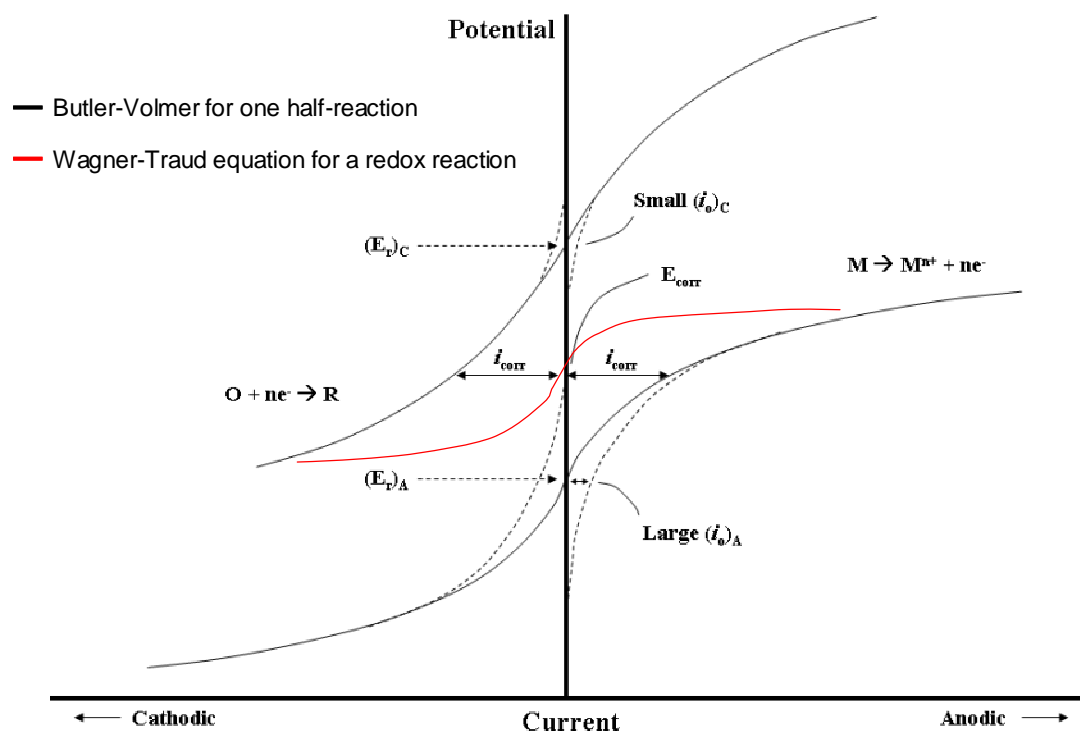


Figure 2.4 Current-potential relationships for coupled reactions in a corrosion process.

2.3 Principles of Experimental Techniques

2.3.1 Open Circuit Potential Measurements

As previously stated the E_{OC} is the potential that is established on a metal working electrode in an electrochemical cell when there is no external current or potential applied

to the system. The rates of the coupled anodic and cathodic reactions depend on a number of factors, including: the working electrode properties, electrolyte concentration and pH, electrode film formation, temperature, and the presence of other species in the electrolyte (such as dissolved oxygen). The E_{OC} can be measured by placing a high impedance voltmeter between the working and reference electrodes of the electrochemical cell. The high impedance of the voltmeter ensures that negligible current flows through the external measurement circuit, which ensures a limited iR (or voltage) drop [13].

The E_{OC} is typically a complicated function of not only the equilibrium potentials of the aqueous- and electrode surface-redox pairs, but also the electrode surface area, and topography, the concentration of the redox couples, and the individual reaction rates. In many cases, changes to surface properties due to the progress of corrosion and the build-up of electrode surface films make it difficult to predict E_{OC} from thermodynamic and kinetic considerations alone.

2.3.2 *Cyclic Voltammetry*

Cyclic voltammetry (CV) is used to study various anodic and cathodic processes that occur at an electrode surface as a function of an applied potential. In a typical cyclic voltammetry experiment, the current density is monitored while the working electrode potential is scanned linearly/at a constant rate of change from an initial starting potential ($E_{initial}$) to a chosen final potential (E_{end}). The scan direction is subsequently reversed and the potential is swept back to the original potential ($E_{initial}$) as illustrated in Figure 2.5. The current measured during the potential scan is a measure of the net rate of the charge

transfer reactions occurring on the working electrode at each time during the scan. An observed anodic current is a measure of the net rate of oxidation on the electrode surface and an observed cathodic current is a measure of the net rate of reduction on the electrode surface. The Faraday Law determines the relationship between the total charge transferred by the current and the number of moles of oxidized or reduced species:

$$m = \frac{Q \cdot M}{F \cdot n} \quad (2.17)$$

where m is the mass (in g), Q is the total charge (in Coulombs), M is the molar mass (in $\text{g} \cdot \text{mol}^{-1}$), F is the Faraday constant, and n is the number of electrons transferred per mol of product.

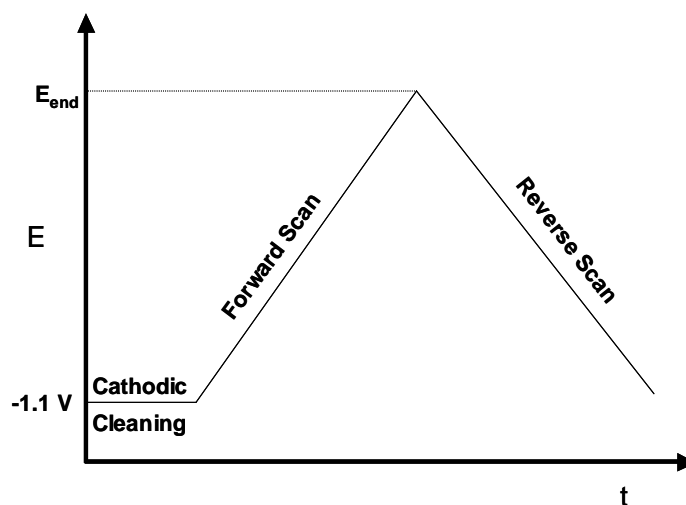


Figure 2.5 The potential-time profile applied in a cyclic voltammetry experiment.

The measured current is recorded as a function of potential and can often provide information about the sequence of electrochemical oxidation and reduction reactions occurring on the electrode. The current response may depend on the potential scan rate (σ), and changes to this parameter may provide information on the relative contribution to the current of “slow” vs. “fast” and reversible vs. irreversible reactions.

There are other elements of cyclic voltammetry that are helpful in understanding electrode kinetics. For example, if an oxidation product formed during the forward scan is insoluble and can be completely reduced during the reverse scan, the total accumulated charge during the anodic scan ($Q_A = \int_{E_{\text{Initial}}}^{E_{\text{End}}} i \cdot dt$) should be equal to that for the cathodic scan ($Q_C = \int_{E_{\text{End}}}^{E_{\text{Initial}}} i \cdot dt$). An idealized cyclic voltammogram depicting the condition where $Q_A = Q_C$ is shown schematically in Figure 2.6

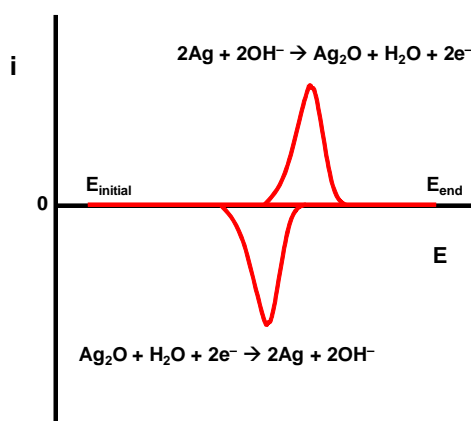


Figure 2.6 The current-potential response in a cyclic voltammetric experiment for a reaction in which all of the anodic charge is recovered during the cathodic scan. The areas under the two peaks are the same.

2.3.3 Potentiostatic Polarization

In a potentiostatic anodic polarization experiment, a constant external potential is applied to the working electrode using a potentiostat and held for a certain length of time while the resulting current is measured. The static potential allows for isolation of the anodic and cathodic reactions involved in corrosion. The value of the applied potential with respect to the E_{OC} will determine the direction of electron flow, thereby allowing

either the anodic or cathodic reaction to be studied at the working electrode. During anodic polarization, oxidation occurs at the working electrode and the resulting electrons are passed through the potentiostat circuitry to the counter electrode where they are available to support the balancing reduction reaction, without affecting the applied potential at the working electrode.

2.3.4 *Cathodic Stripping Voltammetry*

Cathodic stripping voltammetry (CSV) is conducted by scanning the working electrode potential to a lower potential (in a cathodic direction) while monitoring the current that flows during the potential sweep. The cathodic scan usually starts at the E_{OC} and ends at a potential where it is expected that the surface species is fully reduced. During the CSV, species present on the electrode will be reduced at potentials more negative than their thermodynamic equilibrium potentials. If the cathodic behaviour of a system is already known, for example, from a combination of cyclic voltammetry and surface analyses, CSV can be used to quantify the film that forms on the surface of an electrode during an anodic process. It is thus convenient to couple CSV with E_{OC} or potentiostatic anodic polarization to determine the amounts of various species formed on an electrode as a function of potential and time.

By integrating the current attributed to a specific film reduction process in a CSV over time, one can obtain the charge corresponding to the reduction of that film. Assuming that film dissolution does not take place during the stripping and that the electrochemical reduction process goes to completion, Faraday's law can be used to quantify the amount of surface film material that was present.

2.3.5 Galvanostatic Polarization

During a galvanostatic polarization process, a constant current is applied to the working electrode and the potential is monitored as a function of time. In such a controlled current experiment, a redox reaction must occur at the surface of the working electrode in order for the applied current to flow. The sign of the applied current will determine whether the reactions at the surface are oxidizing or reducing. For a reduction process, the potential will initially be set by the reduction of the species on the electrode that can sustain the highest potential. Once the amount of the species on the electrode supporting this redox reaction approaches zero, the applied current can no longer be supported by that particular electron transfer reaction. The potential decreases and is set by the redox potential of the next species that can be reduced. When there is no available redox reaction on the electrode, the potential will change to that which can sustain reduction of water. This process is shown for a cathodic reduction reaction of an electrode with a mixed Ag_2O and AgI film in Figure 2.7.

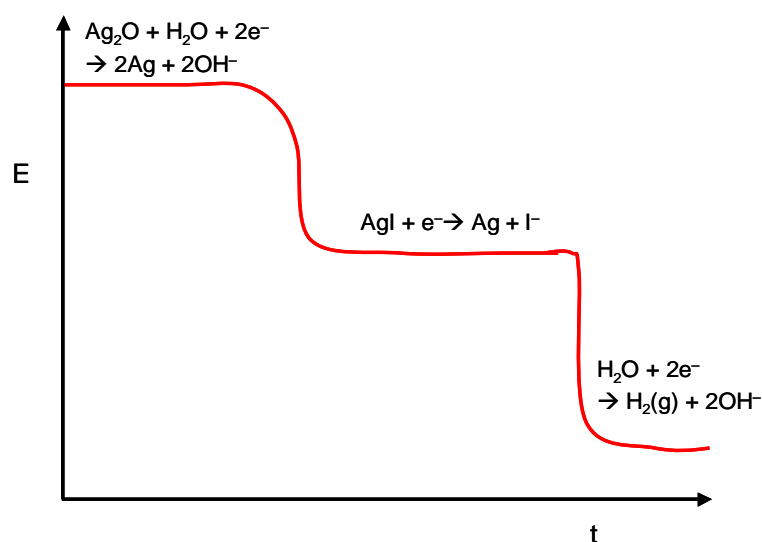


Figure 2.7 A schematic of the potential-time profile for a galvanostatic reduction measurement showing the reduction of a film containing Ag₂O and AgI. Once those species are consumed the potential drops to drive water reduction.

The applied current can be negative (cathodic) or positive (anodic), depending on which redox process is under investigation. The total charge passed during the oxidation or reduction process can be calculated using equation 2.18:

$$Q = i\Delta t \quad (2.18)$$

where Q is the total charge applied during the oxidation/reduction process that occurs at potential (E), i is the applied current, and t is the time at which this potential is sustained.

2.3.6 Linear Polarization Measurements

Linear polarization measurements involve scanning 5 to 30 mV positive and negative of either the E_{OC} or an applied potential, while measuring the current. A very small potential range is selected to minimize perturbation of the system away from the E_{OC} (i.e., the natural corroding system) or from the desired applied potential. The other major reason for using small ΔE is that the Wagner-Traud equation, an exponential relationship, is approximately linear over a small ΔE.

Several useful parameters can be calculated from linear polarization measurements depending on the ongoing electrode kinetics. One parameter, the polarization resistance, can be useful in interpreting passivity in the case of resistive films, or electron transfer in the case of active films [20]. Because the system under investigation in this thesis is unique, specific details of the linear polarization technique as applied to that specific system are described in more detail in Chapter 8, section 8.3.2.3.

2.3.7 Rotating Disc Electrode Experiments

If a reacting species in solution is being consumed at the electrode surface at a rate faster than the rate at which it can be replenished at the surface by solution mass transport, a concentration gradient will develop in the solution near the electrode surface. Under idealized stagnant conditions in the solution, a steady-state reaction rate at the surface cannot be achieved since the concentration gradient will continually change with time. However, completely stagnant conditions are difficult to achieve and natural convection will eventually stabilize the flux, J , of a species to (or from) the electrode surface. Under controlled convective conditions, a linear concentration gradient can be established that depends on the diffusion rate of the species and the flux is approximated by [5]:

$$J = \frac{-D}{\delta}(c^b - c^s) \quad (2.19)$$

where D is the diffusion coefficient, δ is the Nernst diffusion layer thickness, c^b is the bulk concentration and c^s is the surface concentration. Where mass transfer (not electron transfer) is the rate limiting process, c^s is zero. This is schematically depicted by the grey lines in Figure 2.8.

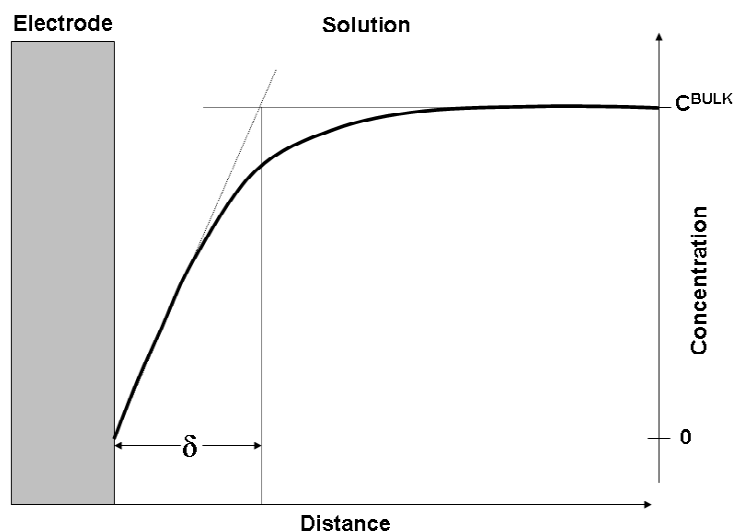


Figure 2.8 Concentration profile of steady-state mass transport controlled reaction under controlled convective conditions adopted from [6].

The flux is an approximation of Fick's first law of diffusion and from this, one can describe the limiting current density, I_L as:

$$|I_L| = \frac{nFDc^b}{\delta} \quad (2.20)$$

A rotating disc electrode is used to force convection currents at the surface of the electrode in a well-defined manner. The movement of the electrode creates conditions of non-turbulent laminar flow parallel to the electrode surface. Variation of the speed of rotation permits control of δ and, hence, I_L .

A rotating disc electrode consists of a circular electrode embedded in a circular PTFE holder. The holder provides additional planar surface area surrounding the disc electrode and the movement of the holder forces turbulent flow to occur away from the surface of interest. The thickness of the diffusion layer next to the electrode and, ultimately, the limiting current will depend on the angular rotation rate, ω , of the

electrode and the solution kinematic viscosity, ν . The limiting current density can be described by the Levich equation:

$$I_L = 0.62nFD^{2/3}\nu^{-1/6}c^b\omega^{1/2} \quad (2.21)$$

Therefore, if a reaction is completely diffusion controlled, a plot of I_L as a function of $\omega^{1/2}$ will be linear, and the slope of that plot can be used to calculate the diffusion coefficient, provided that the number of electrons being transferred in the controlling redox reaction is known.

Often situations exist in which the measured current is not simply controlled by either reaction kinetics or mass transport, but rather partial control by both is observed. In these cases, the species concentration, c^s , at the electrode surface is not zero, but it may still be very small compared to the bulk concentration. In these cases the measured current is still a function of the electrode angular rotation rate, but it is described by the Koutecky-Levich equation:

$$\frac{1}{I_M} = \frac{1}{I_K} + \frac{1.61\nu^{1/6}}{nFc^bD^{2/3}\omega^{1/2}} \quad (2.22)$$

where I_M is the measured current density and I_K is the kinetic current density that would flow if the reaction was not mass transfer limited. A plot of $1/I_M$ versus $\omega^{-1/2}$ will yield a linear relationship which can be extrapolated to infinite ω (or $\delta = 0$) to yield a value for the kinetic current. For a sufficiently large overpotential (η), $\log I_K$ can then be plotted as a function of the applied potential. This type of plot is known as a Tafel plot. While we used a rotating disc electrode in our studies, as described in Chapter 5, we did not use either a conventional Levich or Koutecky-Levich equation to analyze our data. We

derived alternative equations that relate mass transport rates to the E_{OC} to extract chemical kinetic rates [14].

2.4 *Surface Analysis*

Scanning electron microscopy, X-ray photoelectron spectroscopy, and X-ray diffraction were used to study the composition and morphology of oxide and halide films chemically and electrochemically formed on a silver substrate. These measurements were performed on samples of the electrode after removal from the electrochemical cell. Neutron reflectometry was performed *in situ*, while silver oxide was converted to silver iodide. The principles of each technique are described below.

2.4.1 *X-Ray Diffraction*

When a monochromatic X-ray beam of wavelength λ is projected into a solid the atoms will scatter the x-rays in all directions. When the solid has an ordered structure (a crystal lattice for a pure species), constructive and destructive interference of the scattered X-rays will result in diffraction patterns according to Bragg's Law:

$$z \lambda = 2d \sin \psi \quad (2.23)$$

where z is termed the order of reflection, d is the interplanar spacing, and ψ is the diffraction angle. The value of z is an integer and is equal to the number of wavelengths in the path length difference of two X-rays scattered by adjacent crystal planes [15,16]. Note that the conventional symbols for Bragg's Law have been altered to avoid redundancy.

Large databases of XRD spectra for pure species exist, and these can be referenced to aid in the fingerprint identification of an unknown compound. X-rays that are diffracted from the sample can be produced from diffraction occurring well within the sample so XRD is not a surface sensitive analytical technique.

2.4.2 *Scanning Electron Microscopy*

Scanning electron microscopy (SEM) is primarily used to investigate surface topography. A high resolution electron beam is directed onto the sample surface and the scattered electrons are detected. Samples are in a vacuum chamber in order to give both incident and resulting electrons free passage from source to sample, and sample to detector. The incident electrons typically have an energy ranging from 0.2 to 30 keV. They are focused by one or two condenser lenses into a beam with a very fine focal spot, sized 0.4 to 5 nm. The beam passes through pairs of scanning coils or pairs of deflector plates which deflect the beam horizontally or vertically so that it scans in a raster fashion over a rectangular area of the sample surface [17].

When a sample surface is subjected to a focused beam of electrons, various processes can occur. Incident electrons can interact with the atoms on (or very near) the surface of the sample and eject secondary electrons. These are lower in energy than the incident beam and arise only from the sample surface (top few nanometers). They are used to study the sample topography. As a result of proximity to the detector, secondary electrons from areas of higher points on the sample surface are more likely to be detected than electrons from lower points. This results in a brightness contrast in the image that gives the micrograph depth perspective.

Incident electrons can also be elastically scattered as a result of collision with electrons within the sample. As higher atomic number species contain more electrons, the probability of backscattering is greater for higher mass species. A backscattered electron image is useful in discriminating between elements of different atomic mass.

Energetic impact between incident electrons and sample atoms can also promote electrons within the sample atoms to higher energy levels. When the electrons return to their ground state, they emit discrete X-rays, characteristic of a specific energy gap in a specific element. Measurement of these secondary X-rays is called Energy Dispersive X-ray (EDX) Spectroscopy. Since X-ray penetration through samples is greater than electron penetration, these secondary X-rays can escape from much greater depths than are probed by the backscattered electrons (typically depths of 0.02 – 1 mm are possible, depending on the sample elemental composition and the energy of the incident electrons).

Scanning electron microscopy was performed using a Hitachi S-4500 scanning electron microscope. Images were recorded with an accelerating voltage of 10 KeV and a beam current of 20 μ A at a 15 mm working distance. The SEM instrument was also equipped with a Quartz Xone energy dispersive X-ray (EDX) analysis system to analyze the elements present in the surface.

2.4.3 *X-Ray Photoelectron Spectroscopy*

X-ray photoelectron spectroscopy (XPS) spectra are obtained by irradiating a material with X-rays and measuring the kinetic energy (KE) and number of electrons that

are ejected as a result of X-ray adsorption. Photoelectron spectroscopy is based on a single photon/electron ejection process as illustrated in Figure 2.9. The sample is irradiated by X-rays of known energy. Adsorption of an X-ray by an atom on the sample surface leads to the ejection of a single electron from the inner shell of the atom. The kinetic energy distribution of the emitted photoelectrons

$$KE = h\nu - BE - \phi \quad (2.24)$$

is measured using an electron energy analyzer, and a photoelectron spectrum is obtained. Note that BE is the binding energy of the electron in the atom that is ionized, $h\nu$ is the energy of the incident X-ray photons, KE is the kinetic energy of the emitted electron and ϕ is the work function. The work function is a combination of the sample work function and the work function induced by the spectrometer. The sample work function is the minimum amount of energy required to move an electron from the Fermi level of the sample into vacuum, see Figure 2.9. In an XPS measurement, the kinetic energy of the ejected electron is directly measured, and the binding energy of the emitted electron is calculated using equation 2.24 (and knowing $h\nu$ and ϕ) [18].

A typical XPS spectrum is a plot of the measured photoelectron intensity as a function of the binding energy of the electrons detected. Each element produces a set of XPS peaks or lines at characteristic binding energy values. The sizes of the peaks are directly related to the amount of a particular element within the sample volume that is irradiated (typically a spot size of $400 \mu\text{m} \times 700 \mu\text{m}$ and depth 1 – 10 nm).

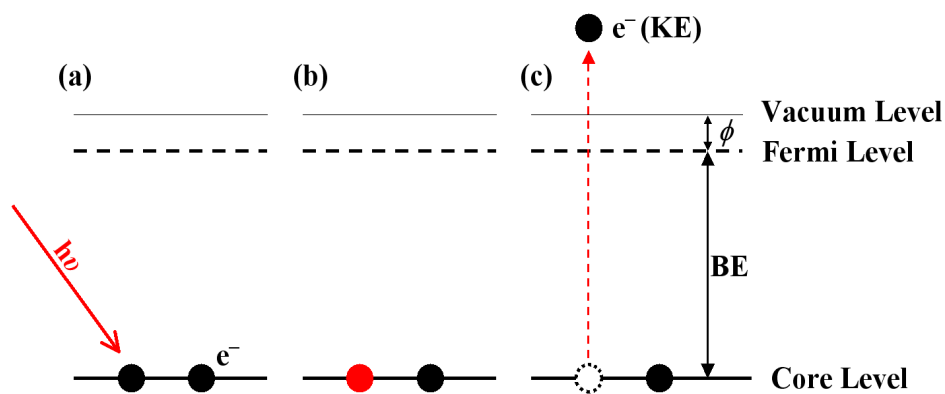


Figure 2.9 Schematic of a single photon/electron ejection process.

2.4.4 Neutron Reflectometry

Specular neutron reflectometry experiments probe the variation in the neutron scattering length density perpendicular to the sample surface at depths from a few, up to several thousand, angstroms [19]. It is a particularly useful technique for investigating layered film structures on surfaces and can be used to characterize surface layers in aqueous environments, such as the $\text{Ag}_2\text{O}/\text{AgI}$ layered film we are studying. The technique is based on the principle that when a highly collimated beam of neutrons of wavelength λ is incident on a flat surface of a material at a small grazing angle θ_i , the penetration depth is small and scattering is limited to the surface and sub-surface regions [19].

The neutron scattering at an interface between two media, A and B, is shown schematically in Figure 2.10. In neutron reflectometry, medium A is usually air or a neutron-transparent material such as silicon. Neutrons are reflected and transmitted at the interface of any two materials with different refractive indexes [20].

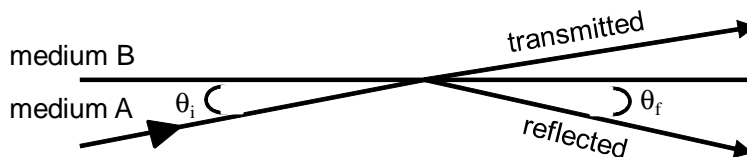


Figure 2.10 A neutron beam is partially reflected and partially transmitted at the interface between two media adapted from [20].

Neutron reflectometry was performed using a time-of-flight apparatus (Figure 2.11) where the incidence angle is fixed and a reflectivity curve is obtained by measuring the neutron beam reflection intensity as a function of the incident neutron wavelength. The Platypus reflectometer used in our studies had a white neutron beam with a spectrum of wavelengths from 2 – 20 Å. The neutron beam was generated by the 20 MW OPAL (Lucas Heights, Australia) research reactor. The incident beam was pulsed by boron-coated disc chopper pairs. Within each neutron pulse there is a continuous band of neutrons of different wavelengths. This band is divided into discrete segments, each corresponding to a narrow wavelength spread, based on the time that it takes for the neutrons to travel from the chopper to the detector. The neutron beam is collimated by passing it through a number of slits, and the angle (θ) of the sample with respect to the incident beam can be varied using a computer-controlled sample holding stage. The reflected neutrons are detected by a 2-dimensional ^3He detector [21].

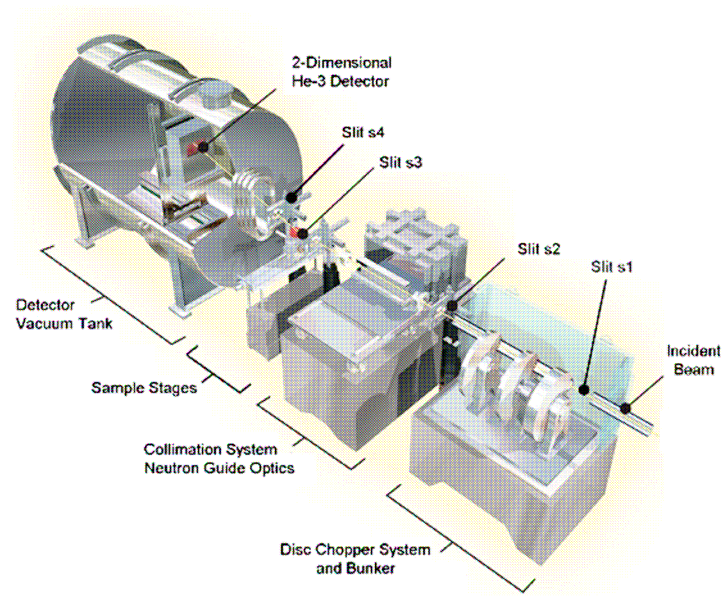


Figure 2.11 The Platypus time-of-flight neutron reflectometer.

Neutron reflectivity data were collected as a function of the momentum transfer (Q_z), normal to the surface of the film, where Q_z is defined by

$$Q_z = \frac{4\pi \sin \theta}{\lambda} \quad (2.25)$$

The measured reflectivity is normalized by dividing the number of neutrons reflected by the sample with the number of neutrons incident upon its surface. Since the wavelength spectrum of the beam is not wide enough to cover a wide Q_z -range in the reciprocal space, data are collected at more than one angle to cover a wider range of Q_z [20].

The neutron reflectivity depends on the scattering length density (SLD) which is determined by the composition and density of the film of interest. The SLD is defined as the product ρb , where ρ is the number density of atoms and b the coherent scattering length of a particular isotope [20]. The experimentally observable reflectivity of a sample depends on the variation in the SLD which in turn is determined by the isotopic composition and density of the constituent layers. The reflectivity spectrum will exhibit

repeated modulated structures which are labeled Kiessig fringes (Figure 2.12). The spacing between the minima of successive fringes is inversely proportional to film thickness [20,21]. If a sample film contains many interfaces, then the reflectivity spectrum will show modulations of several different periodicities. The clarity of the Kiessig fringes depends on the interface width (or roughness) between two materials. Derivations of film type and thickness from neutron reflectivity spectra have the lowest uncertainty if the film components have sub-Angstrom roughness.

Neutron reflectivity data is analyzed by comparing a theoretical or “best guess” model to the measured reflectivity curve. A least-squares refinement procedure is then used to minimize the differences between the theoretical and measured reflectivity curves by changing the parameters that describe each layer. The various parameters in the layer profile that affect the calculated reflectivity curve are the thickness of the layers, the layer SLD, and the interface width. The layer thickness controls the position (in Q_z) of the local minima and maxima of the curve. The SLD, or more accurately the difference of SLD between adjacent layers, controls how deep the minima are compared to the maxima on either side. Finally, the interface width controls how quickly (in Q_z) the overall intensity drops at high Q_z .

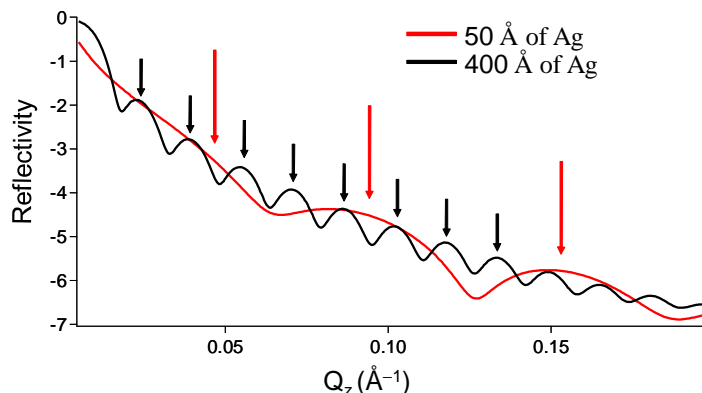


Figure 2.12 Reflectivity of a Si substrate covered by 400 Å of Ag (black line) or a Si substrate covered by 50 Å of Ag (red line). The Kiessig fringes corresponding to the total film thickness of the layer are denoted by arrows.

Neutron reflectivity measurements were carried out on the Platypus time-of-flight reflectometer, at the Bragg Institute, Australian Nuclear Science and Technology Organisation (ANSTO) in Sydney, Australia. This time-of-flight instrument provided 20 Hz neutron pulses and was operated in the medium resolution mode ($\Delta\lambda/\lambda = 4.3\%$). The reflected neutrons were measured using a 2-dimensional helium-3 detector with an active area 500 mm wide \times 250 mm high. Data were collected at two incident grazing angles ($\theta = 0.6^\circ$ for 5 min and $\theta = 2.4^\circ$ for 10 min). Analysis of the data was done with Motofit reflectometry analysis software [21].

2.5 References

1. R.G. Kelly, J.R. Scully, D.W. Shoesmith and R.G. Buchheit, *Electrochemical Techniques in Corrosion Science and Engineering.*, Marcel Dekker Inc., New York (2003).
2. W. Plieth, *Electrochemistry for Material Scientists*, Elsevier, Amsterdam, The Netherlands (2008).
3. *Electrochemical Techniques for Corrosion Engineering*, National

- Association of Corrosion Engineers, Houston, TX, USA. Edited by R. Baboian (1986).
4. *Corrosion Basics: An Introduction*. Published by the National Association of Corrosion Engineers, Houston, TX, USA. Edited by L.S. Van Delinder (1984).
 5. Bard, Allen J., Faulkner, and Larry R. *Electrochemical Methods: Fundamentals and Applications*, 2nd Ed., John Wiley & Sons Inc. (2000).
 6. *Metals Handbook Ninth Edition*, Vol. 13. Corrosion. ASM International, Metals, Park, Ohio. (1987).
 7. W. Nernst, *Z. Physikal. Chem.*, **47**, 52 (1904).
 8. M. Stern, and A.L. Geary, *J. Electrochem. Soc.*, **104**, 56 (1956).
 9. V.C. Wagner, W. Traud, *Z. Electrochemie Angewandt Physika.*, **44(7)**, 391 (1938).
 10. F. Mansfield, "The Polarization Resistance Technique for Measuring Corrosion Currents," in *Advances in Corrosion Science and Technology*, Vol. 6, New York: Plenum Press, 1976.
 11. G.S. Frankel, *J. ASTM Internat.*, **5(2)**, Paper ID JAI101241 (2008).
 12. J.A.V. Butler, *Trans Faraday Soc.*, **19**, 729 (1924).
 13. K.J. Vetter, *Elektrochemische Kinetik*, Springer Verlag, Berlin (1961) [English translation: *Electrochemical Kinetics*, Academic Press, New York (1967)].
 14. J. Tafel, *Z. Phys. Chem.*, **50**, 64 (1905).
 15. W. Niemantsverdriet, *Spectroscopy in Catalysis, An Introduction*, Wiley-VCH, Weinheim (2000).
 16. Cullity, B.D., *Elements of X-Ray Diffraction*, Addison-Wesley Publishing Company Inc. (1959).
 17. Egerton, Ray F., *Physical Properties of Electron Microscopy: An Introduction to TEM, SEM and AE*, Springer Science + Business Media Inc. (2005).
 18. D.J. O'Connor, B.A. Sexton, R.St.C. Smart, *Surface Analysis Methods in Materials Science*, Springer Series in Surface Science, Springer-Verlag, Berlin Heidelberg, Germany. Edited by G. Ertl, R. Gomer, and D.L. Mills (1992).
 19. J. Penfold, R. M. Richardson, A. Zarbakhsh, J. R. P. Webster, D. G. Bucknall, A. R. Rennie, R. A. L. Jones, T. Cosgrove, R. K. Thomas, J. S. Higgins, P. D. I. Fletcher, E. Dickinson, S. J. Roser, I. A. McLure, A. R. Hillman, R. W. Richards, E. J. Staples, A. N.

Burgess, E. A. Simister and J. W. White, *J. Chem. Soc., Faraday Trans.*, **93**, 3899-3917 (1997).

20. Z. Tun, J.J. Noël and D.W. Shoesmith, *J. Electrochem. Soc.*, **146**, 988 (1999).

21. M. James, A. Nelson, S.A. Holt, T. Saerbeck, W.A. Hamilton and F. Klose, *Nucl. Instr. and Meth. Phys. A*, **632**, 112 (2011).

Chapter 3

A Comparison of the Electrochemical Behaviour of Silver-Containing Films on Silver Substrate

3.1 Introduction

In this chapter, comparative studies of the electrochemical behaviour of Ag in aqueous KI, KBr, KCl and halide-free NaOH solutions have been made by means of cyclic voltammetry (CV) and potentiostatic polarization techniques, complemented with scanning electron microscopy (SEM). The separation between the equilibrium potential of the silver-silver oxide ($\text{Ag}_2\text{O}/\text{Ag}$) redox pair and the equilibrium potential for the silver-silver halide (AgX/Ag , where X was I^- , Br^- , or Cl^-) redox pair allows for the formation of a specific type of film, depending on the solution conditions and the potential applied to grow the film. These measurements will provide a basis for the experimental approach used in Chapters 4–8.

3.2 Experimental Details

A silver working electrode, platinum mesh counter electrode, and saturated calomel reference electrode were used for all electrochemical experiments. The silver working electrode had an exposed surface area of 0.385 cm^2 and was polished according to the polishing procedure described in Chapter 2, section 2.1.3 prior to electrochemical tests. Electrochemical measurements were conducted at room temperature in Ar-sparged $0.01 \text{ mol}\cdot\text{dm}^{-3}$ NaOH or $0.02 \text{ mol}\cdot\text{dm}^{-3}$ NaH_2PO_4 . All solutions were made with

deionized water (Chaper 2, section 2.1.2). Potassium bromide, potassium iodide and potassium chloride solutions had a final concentration of $5 \times 10^{-4} \text{ mol}\cdot\text{dm}^{-3}$.

Cyclic voltammetry was performed in solutions of KBr, KI, and KCl, as well as in halide-free NaOH at a scan rate of $5 \text{ mV}\cdot\text{s}^{-1}$. The potential was scanned from $-1.1 \text{ V}_{\text{SCE}}$ to 0.0, 0.2 or 0.4 V_{SCE} , depending on the halide species present in solution. Silver oxide and silver halide films were grown potentiostatically until the total charge reached 0.050 C ($0.13 \text{ C}\cdot\text{cm}^{-2}$). The morphologies of potentiostatically grown Ag_2O , AgI, AgBr and AgCl films were examined using a Hitachi S-4500 field emission scanning electron microscope (SEM).

3.3 Results and Discussion

3.3.1 Cyclic Voltammetry in NaOH Solutions

A cyclic voltammogram (CV) covering a potential range of -1.1 to $0.4 \text{ V}_{\text{SCE}}$ recorded on Ag in a NaOH solution free of halide species is shown in Figure 3.1a. A second CV recorded in NaH_2PO_4 with a potential range of -1.1 to $0.6 \text{ V}_{\text{SCE}}$ is shown in Figure 3.1b for comparison. A small anodic current at potentials slightly negative of the $\text{Ag}_2\text{O}/\text{Ag}$ equilibrium potential, $(E^e)_{\text{Ag}_2\text{O}/\text{Ag}}$, preceded Ag_2O formation, and was attributed to the chemisorption process [1–9],



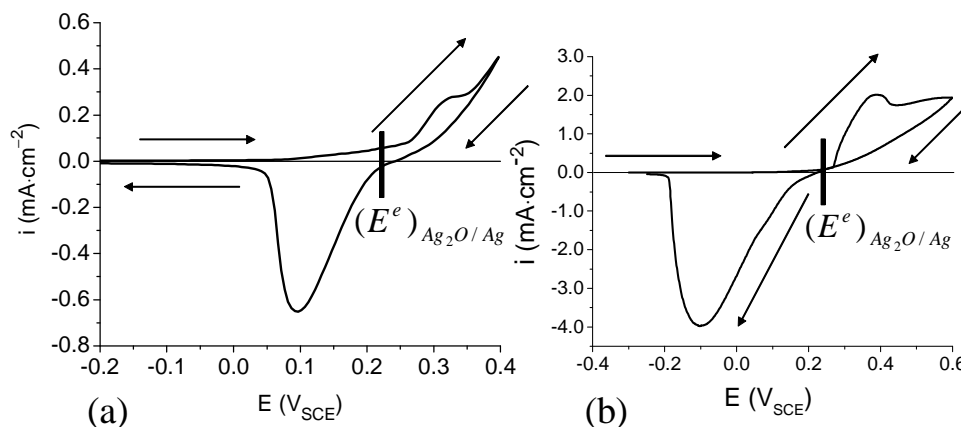


Figure 3.1 Cyclic voltammogram recorded on Ag in (a) $0.01 \text{ mol}\cdot\text{dm}^{-3}$ NaOH solutions to an anodic limit of $0.4 \text{ V}_{\text{SCE}}$ and (b) $0.02 \text{ mol}\cdot\text{dm}^{-3}$ NaH_2PO_4 solutions to an anodic limit of $0.6 \text{ V}_{\text{SCE}}$. The vertical line indicates the equilibrium potential for $\text{Ag}_2\text{O}/\text{Ag}$ at pH 12. Arrows on the CV indicate the direction of potential scanning.

In both cases, the current rose rapidly at potentials slightly higher than $(E^e)_{\text{Ag}_2\text{O}/\text{Ag}}$. The initial steep increase in current was attributed to the oxidation of Ag to Ag(I), which follows a Butler-Volmer potential dependence (equation 2.15, Chapter 2, section 2.2). The slight decrease in current at $\sim 0.32 \text{ V}_{\text{SCE}}$ was attributed to the formation of Ag_2O nucleation sites, and the increase in current that followed was due to Ag_2O film growth at these nucleation sites.

The potential for the onset of Ag_2O formation on the forward scan, and reduction on the reverse scan, occur close to (there is a small delay) the equilibrium potential for the reaction [1–5]:



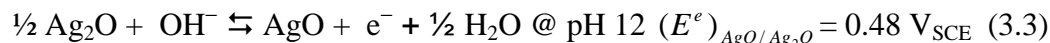
The vertical line in Figure 3.1 indicates the potential value of $(E^e)_{\text{Ag}_2\text{O}/\text{Ag}}$.

The charges used during the forward potential scan ($Q_A^{Ag_2O}$) were compared to those recovered during the reverse scan ($Q_C^{Ag_2O}$). The charges were obtained by integration of the voltammetric currents. In both solutions $Q_A^{Ag_2O} \cong Q_C^{Ag_2O}$, within an error of ~8%. This indicates that nearly all of the anodic charge was used to grow the Ag₂O film on the Ag electrode, and Ag was not lost to dissolution during oxide formation.

The form of the voltammogram was very similar to that observed in phosphate buffered solutions. However, the maximum current density, and hence amount of Ag₂O formed, was much less in NaOH-only solutions compared to NaH₂PO₄ solutions. It is believed that the higher ionic strength of the phosphate solution makes transport of ions in the aqueous phase easier (lower solution resistance), which makes the Ag₂O film kinetically easier to grow.

The polarization resistance ($R_{\text{film}} + R_{\text{solution}} + R_{\text{CT}}$) was calculated from the linear current-potential region of the reduction Ag₂O peak. In phosphate solutions the resistance was low at 58 $\Omega \cdot \text{cm}^2$, compared to a resistance of 416 $\Omega \cdot \text{cm}^2$ in NaOH solutions. The solution resistance was measured by electrochemical impedance spectroscopy and was determined to be ~300 $\Omega \cdot \text{cm}^2$ in NaOH under stagnant conditions. Therefore, the solution resistance contributes significantly to the polarization resistance measured from the Ag₂O reduction peak in NaOH solutions. The addition of phosphate significantly reduced the solution resistance. This suggests that the Ag(I) diffusion through the oxide layer is fast.

In the NaH_2PO_4 CV, the upper anodic limit was extended to $0.6 \text{ V}_{\text{SCE}}$. This introduces the possibility of an additional electrochemical reaction, which involves the conversion of Ag_2O to AgO via the following reaction [1–5]:



Therefore, in order to minimize AgO formation, all Ag_2O films were potentiostatically grown at $0.04 \text{ V}_{\text{SCE}}$ in the following experiments to be discussed.

Another concern when growing Ag_2O in solutions containing NaH_2PO_4 was incorporation of PO_4^{2-} into the silver oxide lattice. SEM micrographs of Ag_2O films grown with the same amount of charge, 0.050 C , in NaOH and NaH_2PO_4 solutions are compared in Figure 3.2. The Ag_2O crystals grown in both solutions have similar diameters, typically in the range of $200 - 500 \text{ nm}$. The slight difference in the Ag_2O crystal shapes may arise from the different rates of film growth in the two solutions. Silver oxide films grown in the presence of phosphate generally grow much faster.

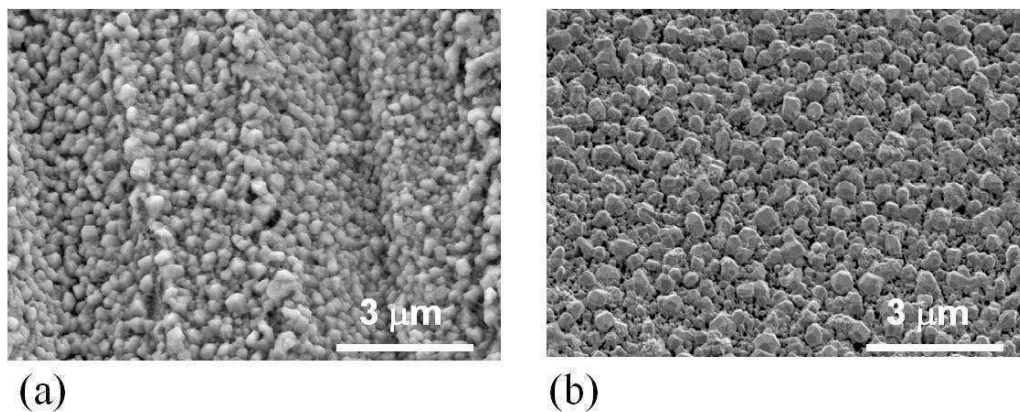


Figure 3.2 SEM images of an Ag_2O film grown in (a) $0.01 \text{ mol-dm}^{-3} \text{ NaOH}$ and (b) $0.02 \text{ mol-dm}^{-3} \text{ NaH}_2\text{PO}_4$. The total anodic charges, $(Q_{\text{Ag}_2\text{O}})_0$, used to grow the films were 0.050 C in both cases.

The influence of electrode rotation rate on the formation and reduction of Ag_2O is shown in Figure 3.3. Increasing the electrode rotation rate did not affect the potentials at which the anodic oxidation of adsorbed species (reaction 3.1), or Ag_2O formation or reduction occurred. At most rotation rates, the anodic current exhibited the same potential dependences discussed previously, i.e. nucleation and growth processes were clearly observed. Increasing the electrode rotation rate resulted in an increase in the anodic and cathodic currents, and hence, amount of Ag_2O oxidized and subsequently reduced, i.e. Q_A and Q_C increased with faster rotation speeds. This increase was likely due to the increased transport of OH^- to the $\text{Ag}|\text{Ag}_2\text{O}|\text{solution}$ interface, where O^{2-} and Ag(I) are injected at opposite sides of the growing oxide interface and result in Ag_2O formation. The notation Ag(I) refers to Ag cations in the solid oxide/halide lattice. These cations are different from the solvated Ag species produced by Ag_2O dissolution which are given the notation $\text{Ag}^+(\text{aq})$. The initial steep increase at potentials positive of $(E^e)_{\text{Ag}_2\text{O}/\text{Ag}}$ was attributed to an increase in Ag(I) production near the bare Ag metal surface. As the concentration of Ag(I) increases, it will precipitate or nucleate on the Ag electrode surface. Under stagnant conditions or slower rotation rates, the large build up of Ag(I) in the interfacial region hinders charge transport in this region and the current decreases. Once the surface was sufficiently nucleated, Ag_2O film growth and thickening continues, as seen by the almost linear increase in current.

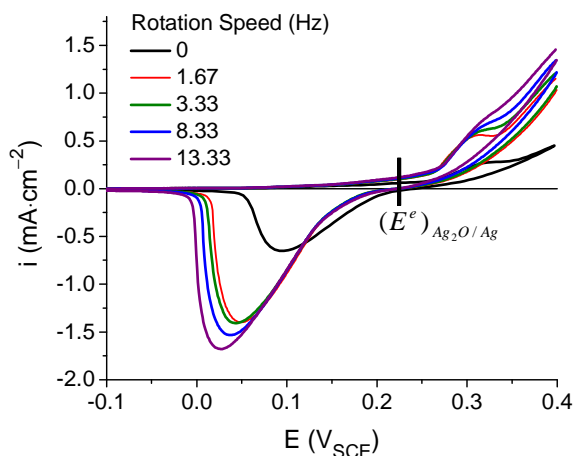


Figure 3.3 Cyclic voltammograms recorded on Ag electrodes in $0.01 \text{ mol}\cdot\text{dm}^{-3}$ NaOH at various electrode rotation speeds. The $\text{Ag}_2\text{O}/\text{Ag}$ equilibrium potential is indicated by the vertical line.

The increase in the area under the cathodic reduction peak further confirms that increasing the electrode rotation rate increased the amount of Ag_2O formed and subsequently reduced during the CV scan. As mentioned above, the resistance measured during the reduction of Ag_2O in NaOH under stagnant conditions was close to the resistance of the solution ($\sim 300 \Omega\cdot\text{cm}^2$) and was $416 \Omega\cdot\text{cm}^2$. As Figure 3.3 shows, increasing the electrode rotation rate changed the resistance and the new resistance was consistent for all rotation rates studied ($90 \Omega\cdot\text{cm}^2$). The linear portion of the current observed during Ag_2O reduction remained constant with increasing electrode rotation rates, which suggests that Ag_2O reduction is limited by aqueous diffusion.

3.3.2 General Features of the Electrochemical Oxidation of Ag in Alkaline Solutions

The anodic behaviour of Ag in alkaline solutions has been studied extensively [1–9], probably because silver is used as a cathode in rechargeable Ag-Zn batteries and Ag-Al batteries. Most researchers agree that the oxidation of Ag to Ag_2O and AgO

involves multiple steps, however there is still some disagreement concerning the mechanism of the electrochemical formation of Ag_2O [1–9]. Some of the points commonly disputed and accepted will be discussed briefly.

Based on the extensive electrochemical and surface analytical research that has been performed, it is commonly accepted that the formation of Ag_2O proceeds by a multi-step process, and solid film formation commences at potentials slightly positive of $(E^e)_{\text{Ag}_2\text{O}/\text{Ag}}$ [1–9]. The first stage of oxidation observed is one of the steps of the oxidation process that is not agreed upon. The small current at potentials slightly negative of $(E^e)_{\text{Ag}_2\text{O}/\text{Ag}}$ has been attributed to many different processes, which include the formation of a monolayer of Ag_2O , a monolayer of AgOH , or dissolution of a silver species [1–9]. In a study by Burstein et al. it was concluded that nucleation of the AgOH monolayer is the rate-determining step of Ag_2O film formation since diffusion of $\text{OH}^-(\text{aq})$ to a scratched Ag surface and charge-transfer were both relatively fast processes [3]. This stage is followed by a second stage that is also commonly disputed whereby either a base layer of Ag_2O is formed, electrodisolution of Ag as $\text{Ag}(\text{OH})_2^-$ occurs, a sublayer of O atoms is trapped in the Ag surface, or there is preferential oxidation of an activated lattice [1–5]. The cyclic voltammetry experiments that we have completed and discussed thus far do not exclude or favour any one of these theories in particular.

The final stage of the anodic formation of Ag_2O has been assigned to the nucleation and three dimensional growth of the Ag_2O phase on the Ag_2O base layer [1–5]. As mentioned above, if the potential is scanned to more positive values the oxidation of Ag_2O to AgO could occur [1–9]. Since the reactant used in the kinetic analysis (Chapter 4) presented in this thesis is an Ag_2O film, we will restrict our

discussion to features relevant to its formation. The structure and layering of the Ag₂O film changes at the different stages of oxidation. Many researchers have agreed that a compact layer of Ag₂O forms under a porous outer Ag₂O layer. The formation of these layers are diffusion or migration controlled and the rate-controlling process is solid-state diffusion of Ag(I) through the oxide lattice [1,2].

More recently, electrochemical techniques have been coupled with *in situ* or *ex situ* surface analysis methods in order to gain a better understanding of the processes involved in the multi-step anodic formation of Ag₂O. In one study, Hur et al. examined the surface of silver electrodes using scanning electron microscopy after electrochemical testing. The images of the Ag electrode after potentiostatic polarization at $(E^e)_{Ag_2O/Ag}$ showed two distinct Ag₂O crystal structures covering the Ag surface. Large crystals coexisted with much smaller hemispherical crystals. The difference observed in Ag₂O crystal size was attributed to Ostwald ripening, where the growth of the larger crystals occurred at the expense of the smaller crystals [1]. They came to this conclusion because the Ag₂O crystals had a bimodal, rather than random, distribution. The Ag₂O crystals shown in Figure 3.2 are not consistent with growth by Ostwald ripening, however we have not performed an extensive investigation of Ag₂O crystal growth.

Hur et al. also examined the Ag surface after continuous potential cycling since many authors had reported changes in the surface area of Ag after repeated potential cycling [5,10]. SEM micrographs after the first cycle showed significant differences compared to freshly polished Ag electrodes. Much smaller reduced Ag particles were present on the surface after Ag₂O reduction. The amount of the reduced Ag particles observed on the surface increased with a positive increase in the anodic potential.

Therefore, changes to the surface roughness were observed by SEM images even after one oxidation/reduction cycle, and the roughness increased with increasingly positive anodic limits [1].

Temperini et al. attempted to analyze the electrochemical formation of Ag₂O films using *in situ* Raman spectroscopy [11]. However, they discovered that Ag₂O is a weak Raman scatterer, and that the frequencies and relative band intensities of the scattered film were from AgO, even though the sample was presumed to only contain Ag₂O, as it was grown at potentials where only Ag₂O was produced. It was determined that Ag₂O was photochemically oxidized to AgO under the influence of light excitation [11]. Based on these results, examination of the Ag₂O/AgX/solution interface by Raman spectroscopy would likely not yield any useful information.

3.3.3 Cyclic Voltammetry in Solutions Containing Br⁻(aq) or I⁻(aq)

Cyclic voltammograms were recorded on Ag electrodes in solutions containing bromide and iodide and are shown in Figure 3.4. For these CVs, the upper potential limit was selected to prevent silver oxidation to Ag₂O.

In both halide solutions, the onset of AgX formation



occurred at potentials slightly positive to the AgX/Ag equilibrium potentials ($(E^e)_{\text{AgI}/\text{Ag}} = -0.20 \text{ V}_{\text{SCE}}$ and $(E^e)_{\text{AgBr}/\text{Ag}} = 0.050 \text{ V}_{\text{SCE}}$). The AgBr/Ag and AgI/Ag equilibrium potentials at the relevant halide concentration were calculated using the Nernst equation and are indicated by vertical lines on Figure 3.4. The small overpotential required before a current was observed on the positive scan is attributed to a requirement for a nucleation

process to occur. Once the nucleation energy barrier is overcome, the anodic current rises quickly [10–18].

The results for $\text{Br}^-(\text{aq})$ are different from those seen for $\text{I}^-(\text{aq})$. For the iodide case, the anodic current quickly reached a plateau that has been attributed to control of AgI formation by aqueous diffusion of $\text{I}^-(\text{aq})$. In the case of $\text{Br}^-(\text{aq})$ no such plateau is seen. Instead, the anodic current increases steadily with potential, but also shows large fluctuations. This indicated that bromide diffusion is only partially rate determining. Since the $\text{Br}^-(\text{aq})$ and $\text{I}^-(\text{aq})$ ion diffusion coefficients in water are similar ($2.080 \times 10^{-5} \text{ cm}^2 \cdot \text{s}^{-1}$ for Br^- and $2.045 \times 10^{-5} \text{ cm}^2 \cdot \text{s}^{-1}$ for I^- [14]), the larger anodic current in the bromide case was attributed to an additional contribution of the oxidation of Ag by $\text{OH}^-(\text{aq})$. The oxidation of Ag by $\text{OH}^-(\text{aq})$ was observed at potentials $> 0.10 \text{ V}_{\text{SCE}}$ in NaOH solutions without any $\text{Br}^-(\text{aq})$ present, see Figure 3.1.

The cathodic current observed on the reverse scan in both halide solutions shows similar potential-dependent behaviour. In both cases the cathodic current increased in magnitude nearly linearly with potential until all of the reducible AgX was reduced and then the current quickly dropped to zero. The linear dependence on potential of the cathodic current indicates that the charge transfer resistance was mainly due to the halide film resistance and not due to the solution resistance or metal-halide interfacial charge transfer. The polarization resistance, calculated from the linear region of the cathodic scan, was similar in both halide solutions, $370 \text{ } \Omega \cdot \text{cm}^2$ for bromide and $400 \text{ } \Omega \cdot \text{cm}^2$ for iodide. The similar resistances observed for the reduction of AgI , AgBr and Ag_2O strongly suggests that the polarization resistance is most likely due to the diffusion of an

aqueous species, and further supports that solid-state diffusion of Ag(I) in the oxide/halide lattice is a fast process.

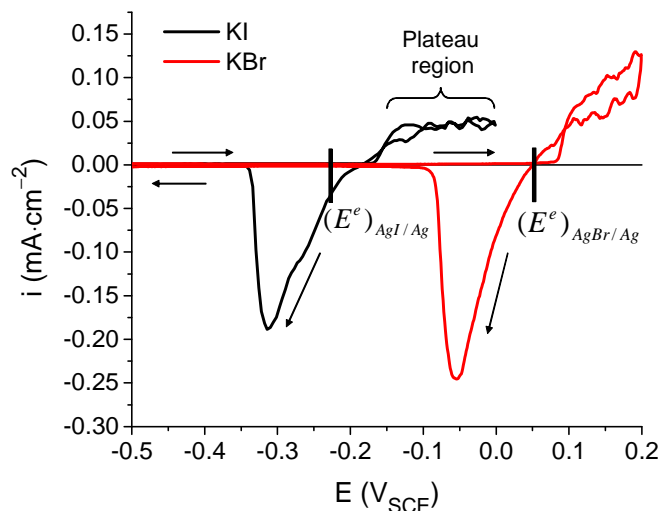


Figure 3.4 Cyclic voltammograms recorded on Ag electrodes in solutions containing KI or KBr. In both cases the halide concentration was $5 \times 10^{-4} \text{ mol}\cdot\text{dm}^{-3}$. For the CV in KBr solutions the potential scan range was between -1.1 and $0.2 \text{ V}_{\text{SCE}}$, and for the CV in KI solutions the potential was scanned between -1.1 and $0.0 \text{ V}_{\text{SCE}}$.

Extension of the upper limit of the anodic scan to $0.4 \text{ V}_{\text{SCE}}$ in halide solutions shows the formation of both Ag_2O and AgX (Figure 3.5). The observation of two distinct cathodic reduction peaks at the expected potentials for Ag_2O and AgX reduction indicates that two distinct Ag_2O and AgX phases are formed. A slightly larger current density was observed in the bromide case compared to the iodide case. The larger current density may be due to the additional reaction of Ag being oxidized by $\text{OH}^-(\text{aq})$ to AgOH which occurs at potentials $> 0.10 \text{ V}_{\text{SCE}}$. A similar shift is not seen for AgI indicating that the AgI film is not as affected as the AgBr film by inclusion of AgOH.

The CVs performed in iodide solution show a clear separation of the Ag_2O and AgI reduction potentials because of the $0.40 \text{ V}_{\text{SCE}}$ separation between $(E^e)_{\text{Ag}_2\text{O}/\text{Ag}}$ and $(E^e)_{\text{AgI}/\text{Ag}}$. Since the peaks are so well separated, individual amounts of Ag_2O and AgI can be determined from the cathodic scan of the CV. This technique, termed cathodic stripping voltammetry (CSV) was used to quantify the amounts of Ag_2O and AgI as a function of reaction time. These results are presented in Chapter 4 and discussed in detail in section 4.3.3.

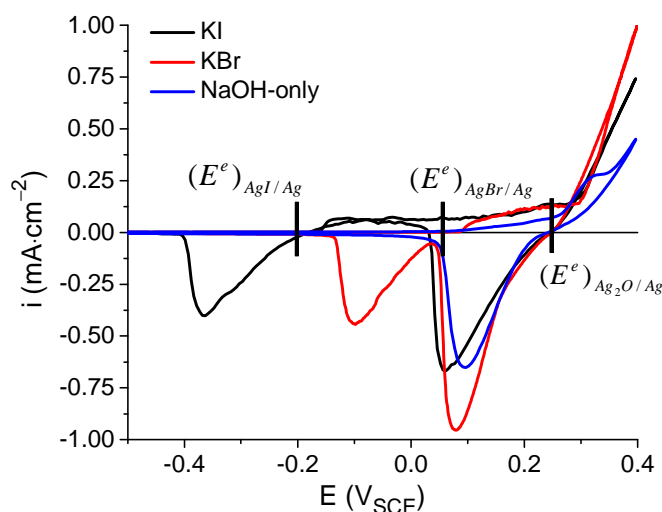


Figure 3.5 Cyclic voltammograms recorded on Ag electrodes in halide-free NaOH (blue line), or solutions containing KI (black line) or KBr (red line) at a concentration of $5 \times 10^{-4} \text{ mol}\cdot\text{dm}^{-3}$. In all cases, the potential was scanned from -1.1 to $0.4 \text{ V}_{\text{SCE}}$.

3.3.4 General Features of the Electrochemical Oxidation of Ag in Iodide and Bromide

Solutions

Rotating disk experiments performed by Birss et al. on Ag electrodes in dilute $\text{Br}^-(\text{aq})$ and $\text{I}^-(\text{aq})$ solutions confirmed that the oxidation of Ag in the presence of either halide was limited by aqueous diffusion of the halide anion to the $\text{AgX}/\text{solution}$ interface.

A linear relationship between current density and the square root of the electrode rotation rate ($\omega^{1/2}$) was also observed, which further confirms our observation that AgX formation was limited by the aqueous diffusion of the halide species [7].

These results were confirmed in a separate study by Brolo et al. who investigated the anodic formation of AgBr by electron probe beam deflection [12]. At potentials just above $(E^e)_{AgBr/Ag}$, linear diffusion models indicated that film thickening was controlled by diffusion of $Br^-(aq)$ from the bulk solution. However, at high positive overpotentials and low $Br^-(aq)$ concentrations a net flux of ions away from the surface was detected. It was suggested that soluble $Ag^+(aq)$ ions were electrochemically produced through the porous AgBr structure under these conditions, and that film thickening was controlled by a dissolution-precipitation mechanism and not diffusion of $Br^-(aq)$ at high anodic limits [12].

3.3.5 Cyclic Voltammetry in Solutions Containing $Cl^-(aq)$

The correct assignment of individual processes responsible for the anodic and cathodic currents observed in a CV can only be made if the equilibrium potentials for the Ag_2O/Ag and AgX/Ag redox pairs are sufficiently separated. For the CVs performed in KI and KBr solutions, $(E^e)_{Ag_2O/Ag}$ was 0.42 V_{SCE} positive of $(E^e)_{AgI/Ag}$, and 0.19 V_{SCE} positive of $(E^e)_{AgBr/Ag}$, therefore the anodic and cathodic currents could be attributed to specific processes. This is not the case for the $AgCl/Ag$ system which has a $(E^e)_{AgCl/Ag}$ of 0.17 V_{SCE} at a $Cl^-(aq)$ concentration of $5 \times 10^{-4} \text{ mol}\cdot\text{dm}^{-3}$. The CV recorded on Ag in

KCl solution (Figure 3.6) reveals that cyclic voltammetry cannot be used to make a clear distinction between the anodic formation of Ag_2O and AgCl .

The similarity of $(E^e)_{\text{Ag}_2\text{O}/\text{Ag}}$ and $(E^e)_{\text{AgCl}/\text{Ag}}$ resulted in a blending of both the anodic and cathodic currents. Careful examination of the cathodic peak revealed the presence of a small shoulder centered at $\sim 0.08 \text{ V}_{\text{SCE}}$, which was most likely due to AgCl reduction since $(E^e)_{\text{AgCl}/\text{Ag}}$ is negative of $(E^e)_{\text{Ag}_2\text{O}/\text{Ag}}$. These results show that the anodic and cathodic currents can be assigned to specific processes occurring in solutions containing KI, KBr or NaOH-only, but not solutions containing KCl at the concentration used in these studies.

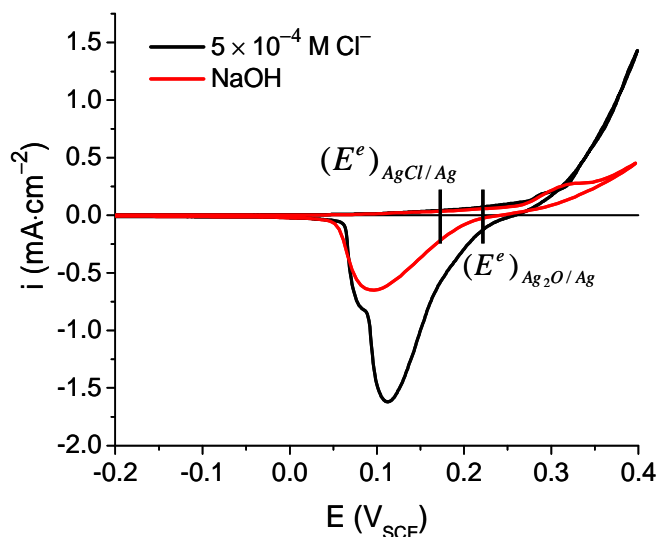


Figure 3.6 Cyclic voltammograms recorded on Ag electrodes in halide-free NaOH and $5 \times 10^{-4} \text{ mol}\cdot\text{dm}^{-3}$ KCl solutions. The potential was scanned from -1.1 to $0.40 \text{ V}_{\text{SCE}}$.

3.3.6 Potentiostatic Film Growth of Ag_2O , AgI , AgBr , and AgCl

The total anodic charge measured as a function of time during the potentiostatic growth of Ag_2O , AgI , AgBr , and AgCl is shown in Figure 3.7. A comparison of the

growth rates of the silver films is complicated since the films were grown at slightly different overpotentials, specifically $0.18 V_{SCE}$ for Ag_2O , $0.20 V_{SCE}$ for AgI , $0.15 V_{SCE}$ for $AgBr$, and $0.08 V_{SCE}$ for $AgCl$. The rate of $AgBr$ and AgI formation was equal until the total accumulated charge reached $\sim 0.1 C \cdot cm^{-2}$, after which the rate of AgI formation increased slightly compared to $AgBr$. The linear increase in total anodic charge observed in KI and KBr solutions suggests that the accumulation of $AgBr$ or AgI on the Ag electrode surface did not affect film growth. Therefore, the $AgBr$ and AgI films do not form a protective or passive layer on the Ag substrate and charge transfer through the growing $AgBr$ and AgI films must be a relatively fast process. This result is also consistent with the cyclic voltammetry results discussed in that the cathodic peak associated with silver halide reduction increased linearly with potential, indicating that charge transfer within the silver-halide film is extremely fast.

The slope of the total anodic charge vs. time was the steepest during the growth of $AgCl$. However, this is somewhat misleading, because as discussed in section 3.3.5, the oxidation of Ag to Ag_2O or $AgCl$ happens concurrently. Therefore, the total charge measured will have contributions from both processes.

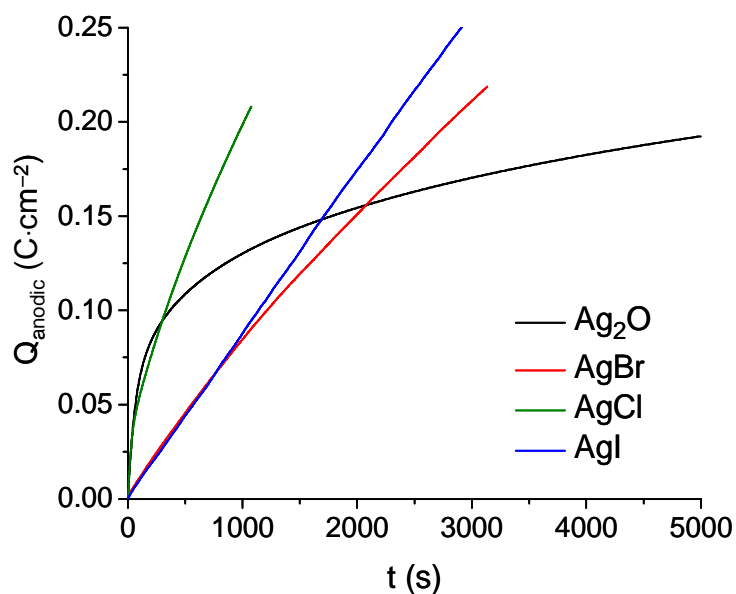


Figure 3.7 Anodic charges accumulated during Ag_2O , AgBr , AgCl , and AgI film growth. For all silver-halide films the bulk halide concentration was $5 \times 10^{-4} \text{ mol}\cdot\text{dm}^{-3}$, and the halide-free NaOH concentration was $0.01 \text{ mol}\cdot\text{dm}^{-3}$.

The anodic growth behavior of Ag_2O was different from the silver halide films.

A sharp, linear increase in the anodic charge was observed until $Q_A^{\text{Ag}_2\text{O}}$ reached $\sim 0.075 \text{ C}\cdot\text{cm}^{-1}$. After $\sim 250 \text{ s}$ the accumulated anodic charge behaviour changed quickly, and increased only a small amount for the remainder of the measurement. The non-linear increase in $(Q_A^{\text{Ag}_2\text{O}})$ vs. time during Ag_2O film growth suggests that the Ag_2O film is more passive or protective compared to the silver halide films, which is consistent with the cyclic voltammetry discussed above.

The surface morphology of the silver oxide and silver halide films were examined by SEM and are presented in Figure 3.8. The films were grown at potentials equivalent to those discussed earlier in this section. The image of a Ag_2O film grown in NaOH

shows that it was composed of small, round, evenly sized crystals ~ 200 nm in diameter. The Ag_2O layer forms a cohesive layer on top of the Ag substrate so the Ag substrate was not visible in the SEM image. Comparing the Ag_2O film to the AgI film, it can be easily seen that the AgI crystals were much larger, and ranged in size from $0.5\text{--}1\ \mu\text{m}$ in diameter. The AgI crystals have much sharper edges compared to the Ag_2O crystals. Potentiostatic growth of AgBr and AgCl did not result in the formation of coherent films and the Ag substrate was clearly visible under the patchy silver halide crystals.

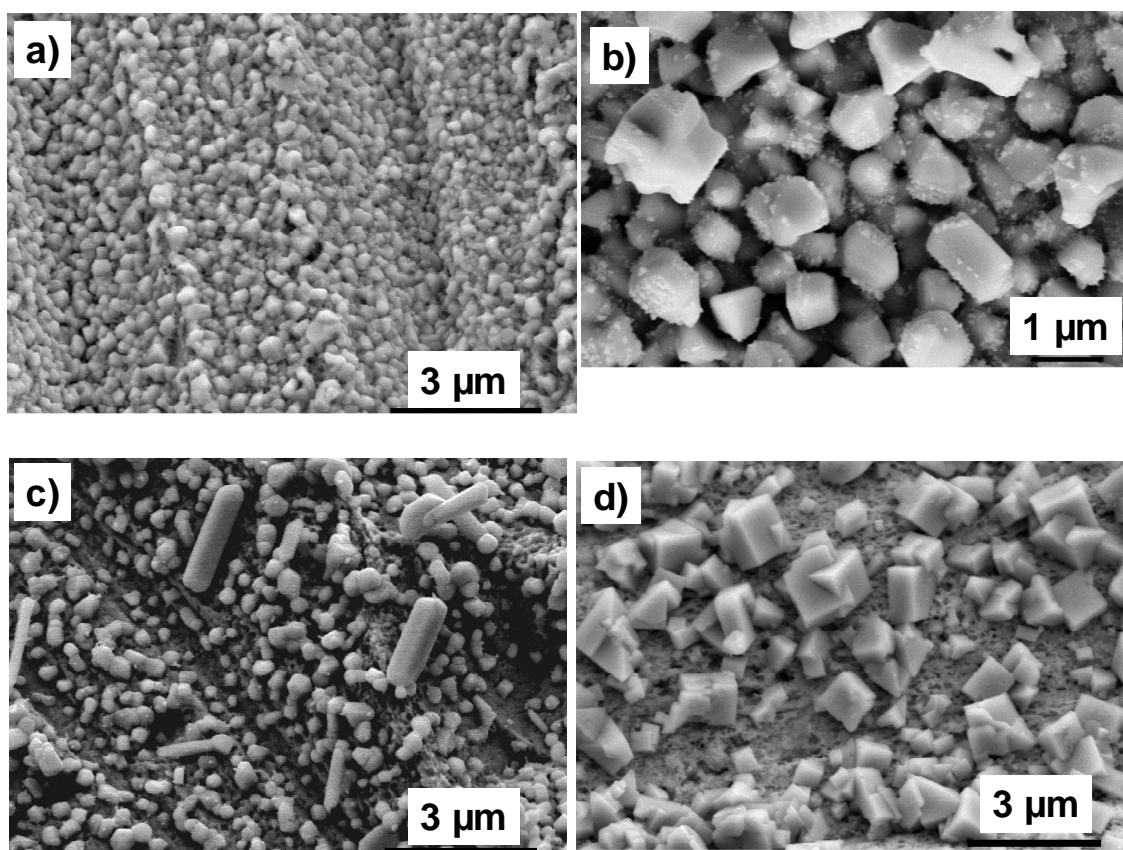


Figure 3.8 SEM images of (a) Ag_2O , (b) AgI, (c) AgBr and (d) AgCl grown potentiostatically on Ag electrodes.

3.4 *Summary and Conclusions*

The electrochemical behaviour of silver oxide and silver halide films was studied using cyclic voltammetry, galvanostatic reduction and potentiostatic polarization. The cyclic voltammograms of Ag in the KI and KBr solutions are similar. However, we have shown that the type of film formed on the surface depends on two factors: (1) solution conditions (i.e. halide *vs.* halide-free) and (2) the magnitude of the applied potential. This finding was significant since we need to grow a consistent Ag₂O film, which serves as the reactant for the kinetic experiments presented in Chapters 4–8.

From our voltammetry results we have also determined that little charge was lost to dissolution, therefore the oxidation and reduction of Ag₂O, AgBr, AgI and AgCl is a nearly a 100% efficient process. Clear separation between the cathodic reduction peaks for Ag₂O and AgX is observed when the Ag₂O/Ag and AgX/Ag equilibrium potentials are well separated. From these results we have determined that cathodic stripping voltammetry (the cathodic half of a CV) would be an appropriate technique for determining the amounts of Ag₂O and AgI present as a function of reaction time, since both will be present on the Ag electrode during the kinetic analysis. This technique would likely not be an appropriate choice when studying the kinetics of the conversion of Ag₂O to AgBr or AgCl since the equilibrium potentials are close.

The voltammetry and potentiostatic polarization results demonstrate that the presence of a Ag₂O or AgX film does not impede additional film growth. This was attributed to fast charge transfer through the Ag₂O or AgX films, and that likely the charge carrier was Ag(I). Due to a large solution volume and small electrode surface area ratio, the halide concentration during the AgX formation remained constant. Therefore,

the effective surface area of silver during AgX film growth was also constant, despite the presence of a AgX film on the Ag electrode surface. The anodic formation of AgX was limited by the diffusion of $X^-(aq)$ from the bulk solution to the electrode surface.

The growth of Ag_2O differed from that observed for AgX. The resistance of the silver oxide layer was higher than the AgX films. Initially the film grew linearly with time, however the accumulated anodic charge quickly came to a plateau after a layer of oxide covered the Ag surface, and the current decreased exponentially with time.

3.5 References

1. T.U. Hur, and W.S. Chung, *J. Electrochem. Soc.*, **152**, A996 (2005).
2. M. Hepel, and M. Tomkiewicz, *J. Electrochem. Soc.*, **131**, 1288 (1984).
3. G.T. Burstein, and R.C. Newman, *Electrochim. Acta.*, **25**, 1009 (1980).
4. J. Kunze, H.H. Strehblow, and G. Staikov, *Electrochem. Commun.*, **6**, 132 (2004).
5. B.M. Jovic, V.D. Jovic, and G.R. Strafford, *Electrochem. Commun.*, **1**, 247 (1999).
6. B.V. Tilak, R.S. Perkins, H.A. Kozłowska, and B.E. Conway, *Electrochim. Acta.*, **17**, 1447 (1972).
7. N.A. Hampson, J.B. Lee, and J.R. Morley, *Electrochim. Acta.*, **16**, 637 (1971).
8. S. Mayer, and R.H. Miller, *J. Electrochem. Soc.*, **135**, 2133 (1988).
9. P. Stonehart, *Electrochim. Acta.*, **13**, 1789 (1968).
10. V.I. Birss, and G.A. Wright, *Electrochim. Acta.*, **27(10)**, 1439 (1982).
11. M.L.A. Temperini, G.I. Lacconi, and O. Sala, *J. Electrochem. Soc.*, **227**, 21 (1987).
12. A.G. Brolo, and Y. Yang, *Electrochim. Acta*, **49**, 339 (2004).
13. A. Hoffman, and A. Ames, *J. Electrochem. Soc.*, **126**, 803 (1979).

14. S.S. Abd El Rehim, H.H. Hassan, M.A.M Ibrahim, and M.A. Amin, *Monatshefte für Chemie*, **129**, 1103 (1998).
15. S. Jaya, T. Prasada Rao, and G. Prabhakara Rao, *J. Appl. Electrochem.*, **18**, 459 (1988).
16. M.F.L. de Mele, R.C. Salvarezza, V.D. Vasquez Moll, H.A. Videla, and A.J. Ariva, *J. Electrochem. Soc.*, **133**, 746 (1986).
17. X. Jin, J. Lu, P. Liu, and H. Tong, *J. Electroanal. Chem.*, **542**, 85 (2003).
18. J.M. Mrgudich, *J. Electrochem. Soc.*, **107**, 475 (1960).

Chapter 4

Interfacial Reaction Kinetics of $\Gamma(\text{aq})$ with Ag_2O on Ag Substrate: Kinetic Model

4.1 Introduction

In this chapter, the conversion of Ag_2O on Ag substrate to AgI in aqueous $\Gamma(\text{aq})$ solutions has been investigated. Electrochemical techniques coupled with surface analysis methods monitored the progression of the conversion reaction. The reactant Ag_2O was grown anodically on Ag substrates prior to exposure to $\Gamma(\text{aq})$. The amount of Ag_2O could be controlled by increasing or decreasing the polarization time.

The conversion reaction was initiated by transferring the Ag_2O -coated electrode to a solution containing a pre-determined concentration of $\Gamma(\text{aq})$. The reaction was followed by monitoring the open circuit potential (E_{OC}). The initial E_{OC} value was close to the equilibrium potential, $(E^e)_{\text{Ag}_2\text{O}/\text{Ag}}$, for the $\text{Ag}_2\text{O}/\text{Ag}$ redox pair. At the end of conversion, the final E_{OC} reached a steady-state value close to the equilibrium potential for the AgI/Ag redox pair. Complete conversion of Ag_2O to AgI was indicated by an abrupt, ~ 400 mV drop in the E_{OC} from $(E^e)_{\text{Ag}_2\text{O}/\text{Ag}}$ to $(E^e)_{\text{AgI}/\text{Ag}}$. The time required for complete conversion is termed the total reaction time, τ_f . This time was easily determined as it corresponded to the time at which the drop in E_{OC} occurred.

The progress of conversion was also monitored by cathodic stripping voltammetry (CSV) which was performed at intermediate reaction times. The cathodic current peaks for the reduction of Ag_2O to Ag and AgI to Ag are well separated (Chapter 3, section 3.3.3). Therefore, cathodic stripping voltammetry was used to determine the amounts of reactant Ag_2O and product AgI present at intermediate reaction times. Comparison of the

total anodic charge used to grow the initial Ag_2O film to the anodic charge(s) recovered from cathodic stripping voltammetry indicated that the conversion reaction was nearly 100% efficient.

Two sets of kinetic experiments were completed in order to determine the surface reaction orders. In the first set of experiments, the amount of Ag_2O was held constant while the effect of $\Gamma(\text{aq})$ concentration on the E_{OC} behaviour was observed. In the second set of experiments, the concentration of $\Gamma(\text{aq})$ was held constant while the amount of Ag_2O grown varied. For all conditions studied the abrupt drop in potential, or potential transition, was observed. These two sets of experiments provided the surface reaction orders. The reaction rate constant was determined two ways. Firstly, the total reaction times from both sets of data were used to calculate an average reaction rate constant. Secondly, by plotting the rate of loss of Ag_2O and rate of gain of AgI as a function of reaction time using the cathodic stripping results, the reaction rate constant was calculated. To our knowledge, this is the first time electrochemical techniques have been used to quantitatively monitor the interfacial kinetics of an aqueous anion induced chemical reaction between two insoluble solids.

This study was also extended to examine the effect of electrolyte composition. Initially all experiments were performed in NaH_2PO_4 solutions for pH control and as a supporting electrolyte (ionic strength). However, energy dispersive x-ray (EDX) analysis showed evidence of phosphate present in the reactant Ag_2O film indicating that phosphate may have incorporated into the Ag_2O film matrix during anodic film growth. As a result we have performed reactions in phosphate-free NaOH solutions to determine

if the incorporation of anions into the electrochemically-grown Ag₂O films exerts a significant influence on the kinetics of the film conversion reaction.

4.2 Experimental Details

Experiments were performed using silver electrodes that were fabricated by the method described in Chapter 2, section 2.1.3. A silver working electrode with an exposed surface area of 0.385 cm², a platinum mesh counter electrode, and a saturated calomel reference electrode (SCE) were used for all electrochemical measurements. Experiments were conducted at room temperature in either Ar-sparged 0.02 mol·dm⁻³ NaH₂PO₄ with the pH adjusted to 12 with NaOH or in 0.01 mol·dm⁻³ NaOH.

Oxide films were grown on Ag substrates using the following procedure. After polishing the Ag electrode using the procedure described in Chapter 2, section 2.1.3, the electrode was cathodically cleaned by applying $-1.1 V_{SCE}$ for 300 s. Silver oxide films were grown potentiostatically by applying $0.4 V_{SCE}$ to the silver electrode. The total charge used to grow the starting Ag₂O film, $(Q_{Ag_2O})_0$, was measured and is related to the initial quantity of Ag₂O in the film by

$$\frac{(m_{Ag_2O})_o}{2} = \frac{(Q_{Ag_2O})_0}{F} = \frac{\int i_{Ag_2O} \cdot t \cdot dt}{F} \quad (4.1)$$

where $(m_{Ag_2O})_o$ is the amount of Ag₂O in the starting film in mol and F is the Faraday constant, 96 485 C·mol⁻¹. Films with different amounts of Ag₂O were prepared by varying $(Q_{Ag_2O})_0$ from 0.035 to 0.063 C (or 0.090 to 0.16 C·cm⁻²). To confirm the accuracy of the film mass determined by this method, reference tests were performed in which the anodically grown Ag₂O was cathodically reduced and the charges for the two

processes were compared. In all cases the two values were the same (within 5%), indicating that the anodic charge used during the potentiostatic film growth is a very good measure of the amount of Ag_2O present in the film.

The Ag_2O covered electrode was then transferred to a NaH_2PO_4 or NaOH solution containing a pre-determined concentration of KI . The KI concentration was in the range of 4×10^{-5} to $5 \times 10^{-3} \text{ mol}\cdot\text{dm}^{-3}$. After transferring the Ag_2O -coated electrode to the KI solution, the progress of the reaction between Ag_2O and $\Gamma(\text{aq})$ was monitored by measuring the E_{OC} as a function of time. At different reaction times, the conversion was terminated by removing the Ag electrode from the KI solution, gently rinsing it with deionized water, and introducing it back into the KI -free solution for further electrochemical testing. Cathodic stripping voltammetry was performed, which entailed scanning the potential from the E_{OC} to $-1.1 \text{ V}_{\text{SCE}}$ at a scan rate of $0.17 \text{ mV}\cdot\text{s}^{-1}$. The CSV measurements were performed at different reaction times, and the reduction currents of un-reacted Ag_2O and the reaction product AgI were measured.

The morphologies of silver electrodes at different reaction times were obtained with a Leo 440 scanning electron microscope (SEM). Prior to SEM analysis, Ag electrodes were removed from the electrolyte solution, rinsed with deionized water, and dried under argon gas.

X-ray diffraction (XRD) data of the Ag_2O films grown in NaOH and NaH_2PO_4 solutions were collected on a BrukerTM D8 Discover diffractometer in an off-coupled scan mode where $\theta_1 = 6^\circ$, and $\theta_2 = 16.5^\circ$ and the beam diameter was $300 \mu\text{m}$. The diffractometer was operated with $\text{Cu } K \alpha$ radiation generated at 40 kV and 40 mA .

4.3 *Results and Discussion*

4.3.1 *Characterization of Electrochemically Grown Ag₂O Films*

To provide a starting point for the kinetic study of $\Gamma(\text{aq})$ with Ag_2O , a known amount of Ag_2O was grown potentiostatically on Ag electrodes in NaH_2PO_4 and NaOH solutions. The SEM micrographs of the Ag_2O films were shown above in Figure 3.2. Slightly different Ag_2O crystal structures were observed. A possible reason for the discrepancy in surface morphology is the incorporation of phosphate anion into the Ag_2O matrix during the anodic Ag_2O film growth in phosphate solutions. Analysis by XRD supports the hypothesis that incorporation of phosphate into the Ag_2O matrix occurred. A clear difference in the X-ray diffraction pattern, Figure 4.1, observable as a peak at $2\theta = 18^\circ$, appears in the diffraction pattern of the Ag_2O film grown in phosphate-containing solutions. This peak was absent from the pattern of the Ag_2O film grown in NaOH and does not correspond to NaH_2PO_4 which may precipitate on the surface in the event of insufficient electrode rinsing. The diffraction pattern did not match Ag_3PO_4 or any of the patterns available in the XRD database, so a positive identification was not made.

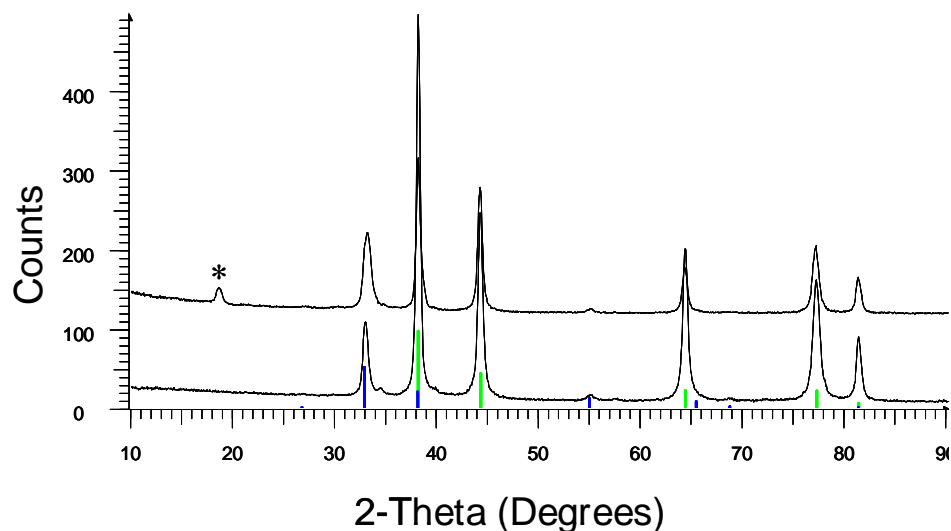


Figure 4.1 XRD patterns recorded for the oxides grown ($(Q_{Ag_2O})_0 = 0.050$ C) in the presence of $0.02 \text{ mol}\cdot\text{dm}^{-3} \text{ NaH}_2\text{PO}_4$ (top pattern) and in $0.01 \text{ mol}\cdot\text{dm}^{-3} \text{ NaOH}$ (bottom pattern). The blue diffraction lines correspond to Ag, and the green diffraction lines correspond to Ag_2O . The asterisk highlights the peak not present in the phosphate-free Ag_2O diffraction pattern.

4.3.2 E_{OC} Behaviour Observed During the Reaction of Ag_2O in $\Gamma(\text{aq})$ Solutions

The time-dependent behaviour of E_{OC} observed during the reaction of Ag_2O with $\Gamma(\text{aq})$ phosphate-free (NaOH) solutions under stagnant conditions for various $\Gamma(\text{aq})$ concentrations is shown in Figure 4.2a. Similar experiments were conducted in phosphate solutions. Since the E_{OC} behaviour observed in NaOH and NaH_2PO_4 was similar, only the data collected in NaOH is presented here. A comparison of the kinetic parameters obtained in both electrolyte solutions is discussed in section 4.4.

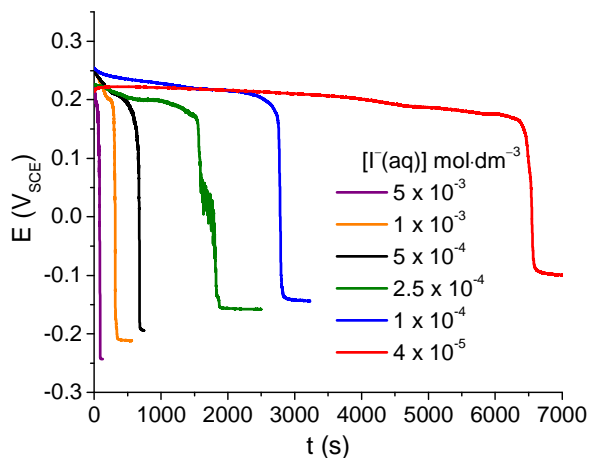


Figure 4.2 Open circuit potential as a function of reaction time and its dependence on $[\Gamma(\text{aq})]_0$ in NaOH solutions where $(Q_{\text{Ag}_2\text{O}})_0$ was constant at 0.050 C. The concentration of $\Gamma(\text{aq})$ ranged from 4×10^{-5} to 5×10^{-3} mol·dm $^{-3}$.

In the second set of experiments, Ag₂O films were potentiostatically grown to different anodic charges, which was accomplished by extending or shortening the duration of polarization at 0.4 V_{SCE}. The Ag₂O films were exposed to a solution containing $\Gamma(\text{aq})$ and the E_{OC} was followed as a function of time. The dependence of E_{OC} on $(Q_{\text{Ag}_2\text{O}})_0$ is shown in Figure 4.3.

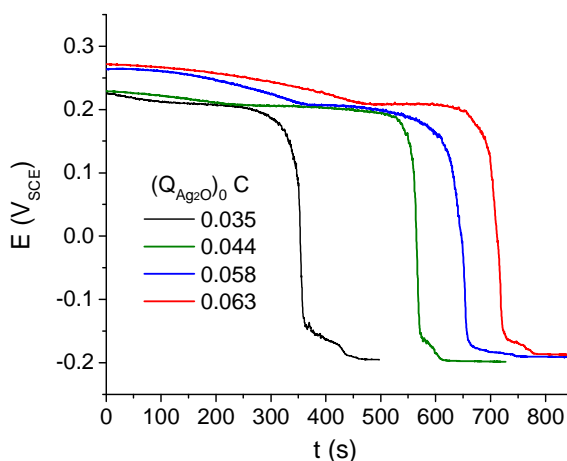


Figure 4.3 Open circuit potential as a function of reaction time and its dependence on $(Q_{Ag_2O})_0$ in NaOH solutions. For these experiments, $[I^-]_0$ was constant at $5 \times 10^{-4} \text{ mol}\cdot\text{dm}^{-3}$ and $(Q_{Ag_2O})_0$ ranged from 0.035 to 0.063 C.

In both sets of experiments (Figure 4.2 and 4.3), the initial value of E_{OC} was very close to the equilibrium potential, $(E^e)_{Ag_2O/Ag}$, for the Ag_2O system. The $(E^e)_{Ag_2O/Ag}$ was calculated by the Nernst equation to be 0.22 V_{SCE} at pH 12. The results presented in Figure 4.2 show that the initial value of E_{OC} was independent of $[I^-]_0$, and varied only marginally for different initial oxide film thicknesses, Figure 4.3. The E_{OC} decreased slowly with time, until it reached a second plateau at a time dependent on $(Q_{Ag_2O})_0$, before undergoing a final abrupt transition to a much lower value, which was close to $(E^e)_{AgI/Ag}$. The time taken to reach the final transition decreased as $[I^-]_0$ increased and $(Q_{Ag_2O})_0$ decreased. The time at which the potential transition occurs is termed the total reaction time, τ_f . This is the time required for complete conversion of Ag_2O to AgI . These values will be used for the kinetic analysis discussed in section 4.4.

The final value of E_{OC} was close to $(E^e)_{AgI/Ag}$ values calculated from the Nernst equation, as shown in Figure 4.4 [7,8]. Note that the final E_{OC} value decreased with higher $\Gamma(aq)$ concentrations, a result that is in agreement with the Nernst equation. Clearly, once the final potential transition has occurred, redox conditions on the Ag surface are dominated by the AgI/Ag redox reaction. Once the potential dropped to a value close to $(E^e)_{AgI/Ag}$ it remained constant.

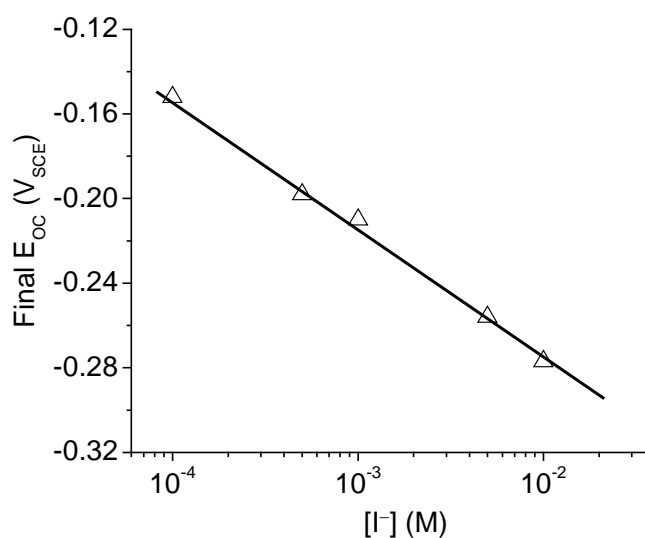


Figure 4.4 Final steady-state E_{OC} values (symbols) observed for various $[I(aq)]_0$ compared to calculated equilibrium potential values for the $Ag + I(aq) \rightarrow AgI + e^-$ reaction (line).

4.3.3 Amounts of Ag_2O and AgI as a Function of Reaction Time

The conversion of Ag_2O to AgI was studied by terminating the reaction at different times by transferring the electrode to an iodide-free solution and performing cathodic stripping voltammetry to determine the amounts of un-reacted Ag_2O that remained and product AgI that formed, Figure 4.5. The results show that the progress of

conversion was clearly monitored. The peak for AgI reduction increased, while that for Ag_2O reduction decreased with an increase in reaction time. Once the transition to the final steady-state E_{OC} value occurred, no Ag_2O remained on the electrode surface and no additional AgI was formed. This confirmed that the potential transition signaled the complete conversion of Ag_2O to AgI.

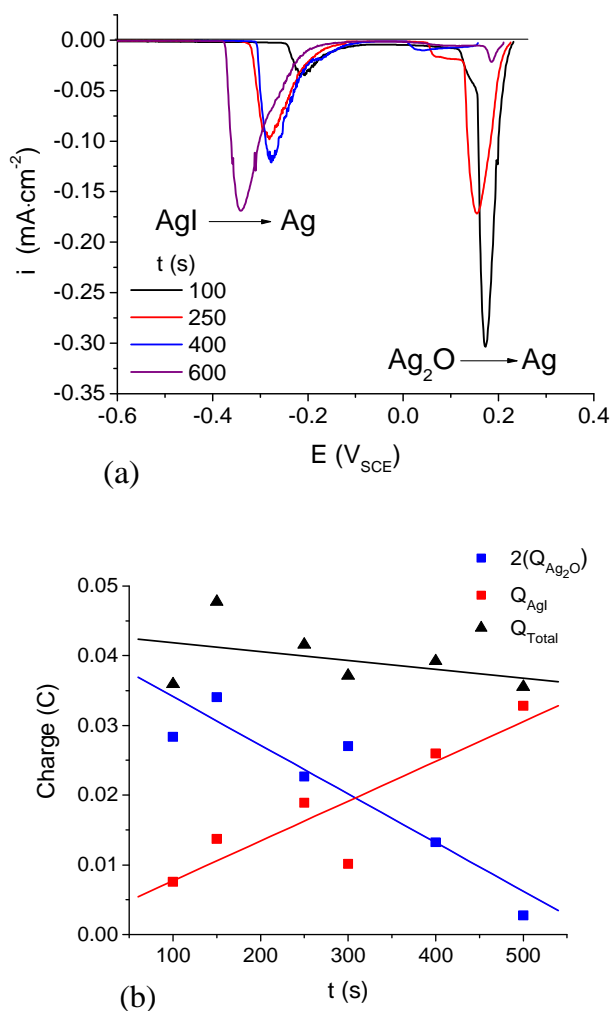


Figure 4.5 (a) Cathodic stripping voltammograms performed on the $\text{Ag}_2\text{O}/\text{AgI}$ covered electrodes following termination of the reaction at various times, and (b) cathodic charges used for the reduction of Ag_2O to Ag and AgI to Ag determined from the CSV. For these experiments $(Q_{\text{Ag}_2\text{O}})_0$ was 0.050 C and $[\Gamma(\text{aq})]_0$ was constant at 5×10^{-4} mol·dm⁻³.

Integration of the two reduction peaks in Figure 4.5a yielded values of $(Q_{Ag_2O})_t$ and $(Q_{AgI})_t$ as a function of reaction time. The values are inversely related, and $(Q_{Ag_2O})_t = 0$ at τ_f , which further confirms there was no residual Ag_2O oxide on the Ag surface at $t = \tau_f$. Therefore, the relationship,

$$2(Q_{Ag_2O})_t + (Q_{AgI})_t = 2(Q_{Ag_2O})_0 \quad (4.2)$$

was maintained throughout the potential transient, confirming the near 100% efficiency of the conversion reaction. There was a small loss of the overall mass of silver, which may be due to some dissolution of Ag_2O .

The cathodic stripping voltammetry results indicate that the rate of the decrease in Ag_2O was approximately equal to the rate of increase in AgI, and the rates were constant with time, Figure 4.5b. The slopes of the two lines in Figure 4.5b were also used to determine reaction rate constants, as described below.

The constant conversion rate (Figure 4.5b), while E_{OC} remained at a value near $(E^e)_{Ag_2O/Ag}$ (Figures 4.2 and 4.3), until the reaction was over, suggests that the progression of the surface reaction of Ag_2O with $\Gamma(aq)$ was linear (i.e., one-dimensional), and that the concentration of $\Gamma(aq)$ reaching the Ag substrate was small. This suggests that the amount of AgI formed from the galvanic coupling reaction (reaction pathway 3) was also small. The small decrease in E_{OC} to a second plateau suggests some contribution of the galvanic coupling reaction (reaction pathway 3) to the overall rate. However, it is believed that the contribution was insignificant [9].

The cathodic stripping study also showed that once the final transition of E_{OC} to $(E^e)_{AgI/Ag}$ occurred, any further exposure of the electrode to the $\Gamma(aq)$ solution does not lead to an increase in AgI.

Images of the Ag electrode surface were also acquired at various reaction times. The time during the E_{OC} transient when the electrode was removed from the $\Gamma(aq)$ solution and an SEM image acquired is shown in Figure 4.6a. Micrographs of the surface were recorded: (b) prior to exposure to $\Gamma(aq)$, (c) after the first short potential transition, and (d) on completion of the reaction ($t = \tau_f$). As the reaction proceeds, the surface becomes progressively covered by small particulates of AgI. The micrograph in (4.6c) shows the coexistence of Ag_2O and AgI particles, confirming that AgI does not form a protective layer on top of Ag_2O and that the underlying Ag_2O was continuously exposed to $\Gamma(aq)$ solution.

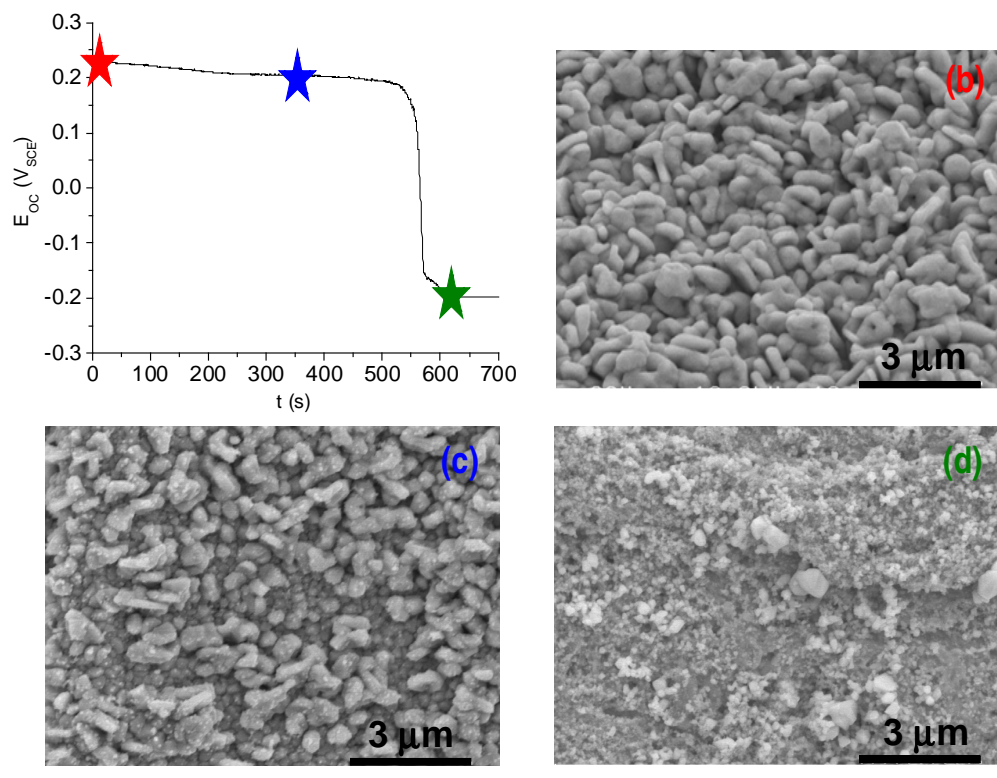


Figure 4.6 SEM images of the Ag electrode surface obtained after various reaction times. The times when the reaction was terminated, and the SEM images taken, are shown in (a), and the corresponding micrographs are shown in (b-d).

4.4 Reaction Kinetic Analysis

4.4.1 Reaction Orders

For a surface reaction, the rate can be expressed as

$$-\frac{1}{2} \cdot \frac{d(m_{Ag_2O})_t}{dt} = k_{Net}^X \cdot (A_{Ag_2O})_t \cdot [X^-(aq)]_t \quad (4.3)$$

where $(m_{Ag_2O})_t$ is the amount of reactant Ag_2O at time t (mol), k_{Net}^X is the net rate coefficient per surface area in units of $cm \cdot s^{-1}$, $(A_{Ag_2O})_t$ is the area of the available Ag_2O reaction sites at time t in units of cm^2 ; and $[X^-(aq)]_0$ is the aqueous halide concentration (in this case $\Gamma(aq)$) of $X^-(aq)$ at time t in units of $mol \cdot dm^{-3}$. Note that $(m_{Ag_2O})_0$ is related

to $(Q_{Ag_2O})_o$ by equation (4.1). Since surface reactions are often limited by the rate of diffusion of aqueous species, a net rate coefficient, which is a function of mass transport and surface reaction rate coefficients, is used in the equation.

As the surface area of the electrodes in our experiments is small compared to the volume of electrolyte in the electrochemical cell (and therefore the amount of halide ion that can be deposited on the electrode surface is small) it can be assumed that the halide aqueous concentration will remain constant.

$$[X^-(aq)]_t \approx [X^-(aq)]_0 \quad (4.4)$$

The thickness of the deposited Ag_2O layer is approximately 440 nm. If the reaction uniformly consumes Ag_2O , then the effective surface area of Ag_2O that is available to the aqueous phase is effectively constant until the last monolayer of Ag_2O is consumed.

Since this monolayer represents a very small fraction of the total film thickness, its consumption can be neglected. Hence, it can be assumed that the area of the available Ag_2O reaction sites at the oxide/solution interface do not vary as the reaction progresses:

$$(A_{Ag_2O})_t \approx (A_{Ag_2O})_0 \approx \text{constant} \quad (4.5)$$

The surface reaction rate becomes constant with time and the rate can be integrated to give:

$$(m_{Ag_2O})_t - (m_{Ag_2O})_0 = -2 \cdot \{k_{Net}^X \cdot (A_{Ag_2O})_0 \cdot [X^-(aq)]_0\} \cdot t \quad (4.6)$$

When the reaction is complete, $t = \tau_f$ and $(m_{Ag_2O})_t = 0$ and

$$\tau_f = \frac{(m_{Ag_2O})_0}{2 \cdot k_{Net}^X \cdot (A_{Ag_2O})_0 \cdot [X^-(aq)]_0} \quad (4.7)$$

Since the amount of Ag_2O is related to the charge used to grow the film, $(Q_{\text{Ag}_2\text{O}})_0$ by equation 4.1, equation 4.7 can be rewritten as

$$\tau_f = \frac{(Q_{\text{Ag}_2\text{O}})_0}{F \cdot k_{\text{Net}}^X \cdot (A_{\text{Ag}_2\text{O}})_0 \cdot [X^-(aq)]_0} \quad (4.8)$$

We have assumed that the electrochemically grown Ag_2O film is uniform, and therefore the thickness depends on the total charge used to grow the film and the electrode surface area:

$$\frac{(Q_{\text{Ag}_2\text{O}})_0}{F} = n_{\text{mol}} \cdot A_{\text{Elec}} \cdot (d_{\text{Ag}_2\text{O}})_0 \quad (4.9)$$

where A_{Elec} is the geometric surface area of the electrode, $(d_{\text{Ag}_2\text{O}})_0$ is the Ag_2O film thickness, F is the Faraday constant, and n_{mol} is the number of moles of Ag_2O per unit volume of Ag_2O film in $\text{mol}\cdot\text{cm}^{-3}$. If we assume that the area of reactive sites is proportional to the electrode surface area the total reaction time can then be expressed using the two known experimental variables, the total charge, $(Q_{\text{Ag}_2\text{O}})_0$, and the halide concentration, $[X^-(aq)]_0$

$$\tau_f = \frac{1}{F \cdot A_{\text{Elec}} \cdot k_{\text{App}}} \cdot \frac{(Q_{\text{Ag}_2\text{O}})_0}{[X^-(aq)]_0} \quad (4.10)$$

where k_{App} is the apparent rate constant for the reaction and has units $\text{cm}\cdot\text{s}^{-1}$.

A more generalized rate equation for a surface reaction can be expressed by allowing the reaction order dependences other than first order dependences:

$$\tau_f = \frac{1}{F \cdot A_{\text{Elec}} \cdot k_{\text{App}}} \cdot \frac{((Q_{\text{Ag}_2\text{O}})_0)^p}{([X^-(aq)]_0)^q} \quad (4.11)$$

This equation states that the reaction orders, p and q, can be obtained from the slope of a $\log \tau_f$ vs. $(Q_{Ag_2O})_o$ or $\log \tau_f$ vs. $[X^-(aq)]_0$ graph.

In the derivation of equation 4.10, it was assumed that the reaction has a first order dependence on $[\Gamma(aq)]_0$ and the Ag_2O surface area. This assumption was based on the cathodic stripping results. However, as mentioned above, the reaction orders can be further confirmed from the relationship between τ_f and $[\Gamma(aq)]_0$ for a given $(Q_{Ag_2O})_o$ or between τ_f and $(Q_{Ag_2O})_o$ for a given $[\Gamma(aq)]_0$, since from equation (4.10)

$$\log \tau_f = const - \log [I^-]_0 \quad (4.12)$$

$$\log \tau_f = const + \log (Q_{Ag_2O})_o \quad (4.13)$$

That is, the slopes of the plots of $\log \tau_f$ vs. $\log [\Gamma(aq)]_0$ and $\log \tau_f$ vs. $\log (Q_{Ag_2O})_o$ should be -1 and $+1$ if there is a first order dependence on $[\Gamma(aq)]_0$ and $(A_{Ag_2O})_o$, respectively.

The τ_f observed as a function of $(Q_{Ag_2O})_o$ and $[\Gamma(aq)]_0$ are shown in log-log plots in Figures 4.7a and 4.7b. These plots yield slopes of -0.9 ± 0.1 and 1.0 ± 0.1 , further confirming first-order dependence on $[\Gamma(aq)]_0$ and $(A_{Ag_2O})_o$. The scatter in the $\log \tau_f$ vs. $\log (Q_{Ag_2O})_o$ plot may be attributed to a small dependence of the surface area on the total charge used to grow the Ag_2O film. Similar experiments performed in phosphate solution provided similar values from the log-log plots, which yielded slopes of -0.9 ± 0.1 and 1.2 ± 0.07 . In both solutions, the conversion of Ag_2O to AgI exhibited a first-order dependence on both $[\Gamma(aq)]_0$ and $(A_{Ag_2O})_o$, indicating that the presence of phosphate in solution, and/or the potential incorporation had a negligible effect on the reaction kinetic orders.

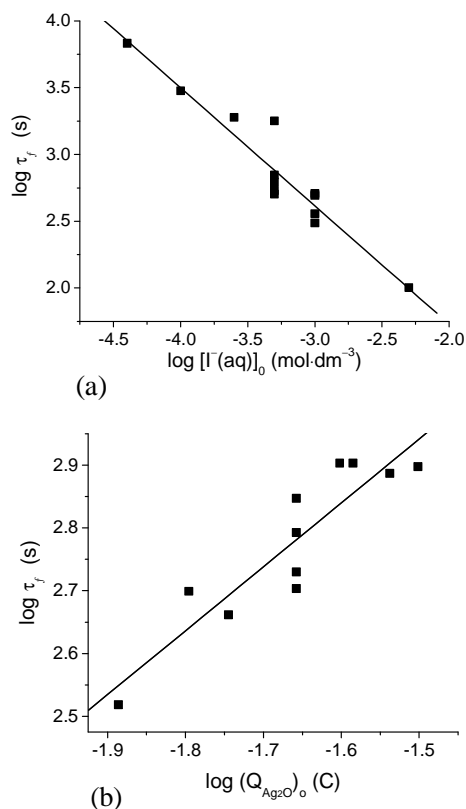


Figure 4.7 (a) Plot of the log of the total reaction time vs. log of $[\Gamma(\text{aq})]_0$. (b) Plot of the log of the total reaction time vs. log $(Q_{\text{Ag}_2\text{O}})_0$.

4.4.2 Apparent Reaction Rate Constant

Since the true surface area of Ag_2O has not been determined, the apparent rate constant, k_{app} , was obtained using the geometric surface area of the electrode. A value for k_{app} can be extracted from the total reaction time observed as a function of $[\Gamma(\text{aq})]_0$. The apparent reaction rate constant was then obtained using equation 4.10 and all of the experimentally obtained τ_f values. For the Ag_2O grown in phosphate-free NaOH solutions, the average rate constant was $(4.6 \pm 1.6) \times 10^{-3} \text{ cm}\cdot\text{s}^{-1}$. This compares well with the k_{app} value of $5.4 \times 10^{-3} \text{ cm}\cdot\text{s}^{-1}$ obtained in the presence of phosphate buffer.

Alternatively, k_{app} can be obtained from $(Q_{Ag_2O})_t$ and $(Q_{AgI})_t$ as a function of reaction time from:

$$(Q_{AgI})_t = ((Q_{Ag_2O})_0 - (Q_{Ag_2O})_t) = k_{app} \cdot F \cdot ([I^-]_0) \cdot A_{Elec} \cdot t \quad (4.14)$$

Hence, Figure 4.5b yields a k_{app} of $3.8 \times 10^{-3} \text{ cm} \cdot \text{s}^{-1}$ and is in good agreement (within 50%) with the k_{app} value obtained from the total reaction time. A more rigorous kinetic study to determine the rate constant more accurately has been completed and is presented in Chapter 5.

Although the XRD analysis results suggest that there was some incorporation of phosphate into the Ag_2O matrix during the initial anodic Ag_2O film growth in phosphate solutions, this study suggests that its presence does not seem to have any influence on the mechanism or kinetics of the conversion. Considering there is some variability in the morphologies of the Ag_2O films as shown by SEM micrographs, the E_{OC} behaviour and CSV results show that neither the incorporation of phosphate into the Ag_2O film, nor its presence during the interaction of Ag_2O with $\Gamma(\text{aq})$, significantly affects the reaction orders or the rate constant.

4.5 Conclusions

The chemical conversion of Ag_2O with $\Gamma(\text{aq})$ to AgI in aqueous iodide solutions has been studied by following the reaction on open circuit. The amounts of oxide and iodide on the Ag substrate were determined at intermediate reaction times by cathodic stripping voltammetry. The reaction was nearly 100% efficient since both the oxide and the iodide are very insoluble under the experimental conditions.

Complete conversion was indicated by an abrupt transition in the E_{OC} from a value close to the equilibrium potential for the Ag_2O/Ag redox pair to a value close to the equilibrium potential for the AgI/Ag redox pair. This abrupt change in E_{OC} allowed for an easy determination of the total reaction time required for complete conversion. The time to complete the reaction was inversely proportional to the iodide concentration, and nearly proportional to the amount of oxide electrochemically grown on the Ag surface.

The rate of the chemical conversion, determined by cathodic stripping voltammetry as a function of time, was constant, indicating that the effective surface area of Ag_2O available for the reaction was constant. This constant surface area was attributable to the fact that the AgI product did not form a protective layer on the Ag_2O surface.

A detailed kinetic analysis established the relationship between the total reaction time and the reaction orders. From the total reaction times as a function of iodide concentration and initial Ag_2O inventory, the rate was found to be first order in iodide concentration and first order in oxide surface area in both electrolyte solutions. This indicates that the presence of phosphate in solution, and/or the potential incorporation of phosphate anions into the Ag_2O oxide phase did not affect the reaction kinetics.

The kinetic analysis discussed in this chapter was published in 2007 in the Journal of the Electrochemical Society [3]. Based on the kinetic data obtained, rate equations were derived which can be used in models developed to predict the fate of radioiodine in various proposed nuclear reactor accident scenarios.

4.6 References

1. A.M. Zaky, F.H. Assaf, S.S. Abd El Rehim, and B.M. Mohamed, *Applied Surface Science*, **221**, 349 (2004).
2. T.U. Hur, and W.S. Chung, *J. Electrochem. Soc.*, **152**, A996 (2005).
3. J.G. Becerra, R.C. Salvarezza, and A.J. Arvia, *Electrochim. Acta.*, **33**, 1431 (1988).
4. J.M. Droog, P.T. Arderliesten, and G.A. Bootsma, *J. Electroanal. Chem.*, **99**, 173 (1979).
5. B.M. Jovic, and G.R. Strafford, *Electrochem. Commun.*, **1**, 247 (1999).
6. B.J. Murray, O. Li, J.T. Newberg, E.J. Menke, J.C. Hemminger, and R.M. Penner, *Nano Letters*, **5**, 2319 (2005).
7. X. Zhang, S.D. Stewart, D.W. Shoesmith, and J.C. Wren, *J. Electrochem. Soc.*, **154**, F70 (2007).
8. A.J. Bard, and L.R. Faulkner, *Electrochemical Methods: Fundamentals and Applications*, 2nd ed., John Wiley & Sons Inc., Hoboken, NJ, 2001, pp 337-339.
9. X. Zhang, D.W. Shoesmith, and J.C. Wren, *Corr. Sci.*, **50**, 490 (2008).
10. R.L. Flemming, *Can. J. Earth Sci.*, **44**, 1333 (2007).

Chapter 5

Investigation of Interfacial Reaction Kinetics of $\Gamma(\text{aq})$ with $\text{Ag}_2\text{O}(\text{s})$ on Ag

Substrate: Determining Mass Transport and Surface Reaction Rates

5.1 Introduction

In this chapter we examine the effect of $\Gamma(\text{aq})$ transport to the Ag_2O surface by measuring the total reaction time (τ_f) as a function of electrode rotation rate. By studying the conversion as a function of electrode rotation rate we are able to separate transport effects from the reaction kinetics. The interfacial reaction follows kinetics typical of a sequential binary-reaction system of mass transport followed by reaction at the surface. Varying the rotation rate allows a quantitative extrapolation of the data to the infinite rotation rate to determine the chemical reaction rate at the surface.

5.2 Experimental Details

The working electrodes were silver with an exposed surface area of 0.385 cm^2 . A platinum mesh counter electrode and saturated calomel reference electrode (SCE) were used for all electrochemical measurements. Experiments were conducted at room temperature in Ar-sparged $0.01 \text{ mol}\cdot\text{dm}^{-3}$ NaOH or $0.02 \text{ mol}\cdot\text{dm}^{-3}$ NaH_2PO_4 with the pH adjusted to 12 with NaOH. Potassium iodide solutions were prepared with deionized water and had a final concentration of $5 \times 10^{-4} \text{ mol}\cdot\text{dm}^{-3}$.

Silver electrodes were polished following the polishing procedure described in Chapter 2, section 2.1.3. Electrodes were rinsed, and cathodically reduced at $-1.1 \text{ V}_{\text{SCE}}$ for 300 s. Silver oxide films were grown by applying $0.4 \text{ V}_{\text{SCE}}$ until the total anodic

charge reached 0.050 C. The Ag₂O-covered electrode was then mounted on a rotating shaft, and electrode rotation was initiated prior to transferring the Ag₂O-coated electrode in the NaOH or NaH₂PO₄ solution containing Γ(aq). The progress of the reaction was monitored by measuring the E_{OC} with time.

5.3 Results and Discussion

5.3.1 Mass Transport Rate and Surface Reaction Rate

The rate of a solid-solution interaction is determined by both the transport of the aqueous reactant, Γ(aq), to the reactant surface, and the kinetics of the reaction between Γ(aq) and Ag₂O on the surface. The overall rate constant, k_{app}, of the binary kinetic system is typically expressed as

$$\frac{1}{k_{app}} = \frac{1}{k_{mass}} + \frac{1}{k_{surf}} \quad (5.1)$$

where k_{mass} is the mass transport coefficient and k_{surf} is the surface reaction rate constant. The results discussed in Chapter 4 were performed under stagnant conditions, and the observed rate constant approached values that were typical of an aqueous diffusion-controlled reaction. This indicated that the apparent reaction rate might have been mass transport limited. To determine whether this was the case, the Ag₂O to AgI conversion kinetics were studied as a function of electrode rotation rate.

Figure 5.1a shows the effect of electrode rotation rate on the E_{OC} behaviour. The general trend in E_{OC} was similar to the behaviour observed under stagnant conditions (Chapter 4, Figure 4.4 and 4.3). Initially the E_{OC} was close to $(E^e)_{Ag_2O/Ag}$, but dropped to $(E^e)_{AgI/Ag}$ upon completion of the conversion. The total reaction time, determined by the

transition in E_{OC} , however, is a strong function of the rotation rate. The solution to the convective-diffusion equation describing transport at a rotating disk is well established [1] and provides the diffusion boundary layer thickness, δ_{diff} , as a function of electrode angular velocity, ω :

$$\delta_{diff} = 1.61 \cdot D^{1/3} \cdot \omega^{-1/2} \cdot \nu^{1/6} \quad (5.2)$$

where ν is the kinematic viscosity and has units of $\text{cm}^2 \cdot \text{s}^{-1}$, and $\omega = 2\pi f$, where f is the rotation frequency and ω is otherwise known as angular rotation frequency or rate. Since the mass transport rate is inversely proportional to δ_{diff} ,

$$\frac{1}{k_{mass}} \propto \omega^{-1/2} \quad (5.3)$$

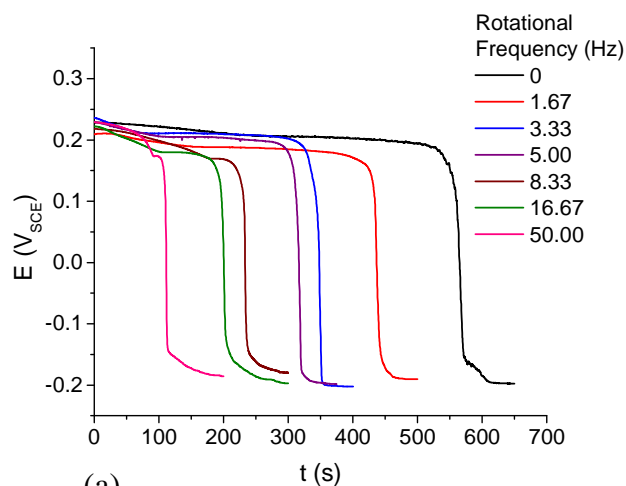
From Equations 5.1, 4.10, and 5.3,

$$\tau_f = C_{diff} \cdot \omega^{-1/2} + \tau_{surf} \quad (5.4)$$

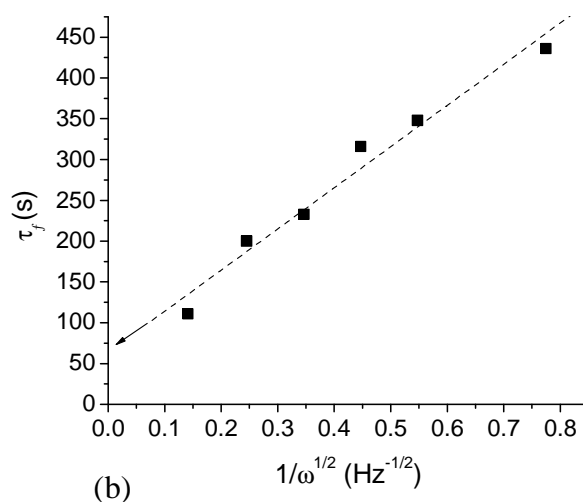
with,

$$\tau_{surf} = \frac{(Q_{Ag_2O})_0}{F \cdot (A_{Elec}) \cdot [I^-]_0} \cdot \frac{1}{k_{surf}} \quad (5.5)$$

where τ_{surf} is the total reaction time at infinitely fast electrode rotation rate and C_{diff} is a proportionality constant.



(a)



(b)

Figure 5.1 (a) E_{OC} as a function of reaction time and its dependence on electrode rotation rate, and (b) total reaction time τ_f vs. $1/\omega^{-1/2}$. The experimental conditions were $0.01 \text{ mol}\cdot\text{dm}^{-3}$ NaOH, $(Q_{Ag_2O})_0$ was constant at 0.050 C and $[\Gamma(\text{aq})]_0$ was $5 \times 10^{-4} \text{ mol}\cdot\text{dm}^{-3}$ for all cases. Electrode rotation rate ranged from 0 to 50 Hz.

Equation 5.4 states that τ_f would increase linearly with $\omega^{-1/2}$, and the intercept of a τ_f vs. $\omega^{-1/2}$ plot provides a value of τ_{surf} from which the surface reaction rate constant, k_{surf} , can be obtained. The τ_{surf} value was obtained using the least-square analysis for data collected in phosphate-free NaOH solutions (Figure 5.1b). The τ_{surf} value (the y-intercept

of Figure 5.1b) was determined to be 64 s. The apparent surface reaction rate constant was calculated to be $k_{\text{surf}} = 4.2 \times 10^{-2} \text{ cm}\cdot\text{s}^{-1}$. This value was approximately an order of magnitude larger than the net rate constant obtained under stagnant conditions [2]. Therefore, under our experimental conditions, aqueous transport of $\Gamma(\text{aq})$ to the Ag_2O surface was the rate-determining step under stagnant conditions.

After developing this relatively simple method to separate mass transport and surface reaction rates, experiments were also performed with phosphate present. For these experiments phosphate was present during both the growth of the Ag_2O film and during the chemical conversion under electrode rotation. The results obtained with phosphate present also show the same electrode-rotation dependence of τ_f ; an increase in electrode rotation rate results in a decrease in τ_f , Figure 5.2a. From the τ_f vs. $\omega^{-1/2}$ plot (Figure 5.2b), k_{surf} in phosphate solution was determined to be $7.5 \times 10^{-2} \text{ cm}\cdot\text{s}^{-1}$. This value was ~20 times larger than the net rate constant obtained with no rotation in phosphate solution [2,3].

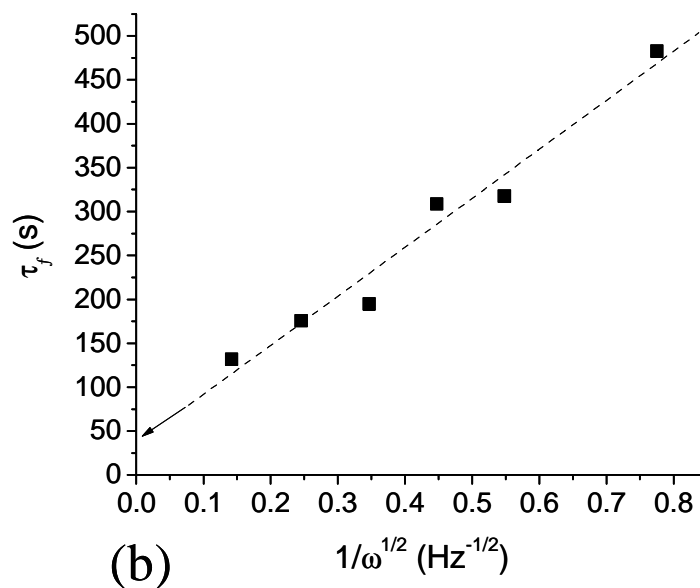
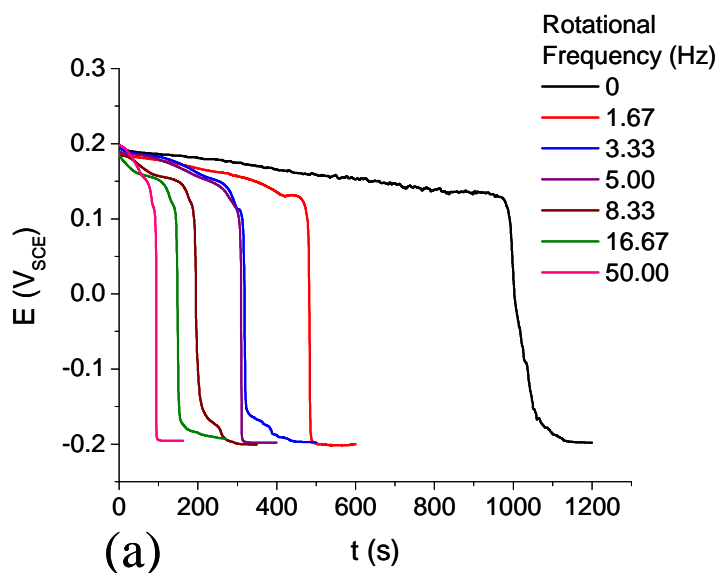


Figure 5.2 (a) E_{OC} as a function of reaction time and its dependence on electrode rotation rate, and (b) total reaction time $\nu s. 1/\omega^{-1/2}$. The experimental conditions were $0.02 \text{ mol}\cdot\text{dm}^{-3} \text{ NaH}_2\text{PO}_4$, $(Q_{Ag_2O})_0$ was constant at 0.050 C and $[\Gamma(\text{aq})]_0$ was $5 \times 10^{-4} \text{ mol}\cdot\text{dm}^{-3}$ for all cases. Electrode rotation rate ranged from 0 to 50 Hz.

The surface reaction rate constant observed in the presence of phosphate was approximately twice that observed in the absence of phosphate: $7.5 \times 10^{-2} \text{ cm}\cdot\text{s}^{-1}$ vs. $4.2 \times 10^{-2} \text{ cm}\cdot\text{s}^{-1}$. The difference may be partially attributed to the difference in the initial surface area ($A_{\text{Ag}_2\text{O}})_0$ of the Ag_2O films grown in the presence and absence of phosphate.

5.4 Comparison of Kinetic Parameters to Established Literature Values

In 2005 Güntay et al. [4], investigated the radiation-induced decomposition of AgI colloids under a variety of conditions. Experiments included reactions in the presence of an initial excess of $\text{Ag}^+(\text{aq})$ and $\Gamma(\text{aq})$, at pH 2 and 5, and with N_2O or Argon sparging [4]. The results of this study showed that volatile iodine species could be formed via the decomposition of AgI by reaction with oxidizing free radicals such as $\bullet\text{OH}$, $\bullet\text{Cl}$ and $\bullet\text{Cl}_2^-$ but the production of these radicals is completely suppressed when a large excess of $\text{Ag}^+(\text{aq})$ is present [4]. While the authors were particularly thorough in their investigation, the possibility of the formation of Ag_2O and its subsequent reaction with $\Gamma(\text{aq})$ was not evaluated. Due to the highly oxidizing conditions expected during irradiation it is reasonable to expect that Ag would be in contact with O_2 , thus, allowing for the formation of both AgI and Ag_2O . It is well known that the degree of oxidation of Ag will have a significant influence on the interaction of Ag species with $\Gamma(\text{aq})$ [5]. However, the interaction of Ag with I_2 remains unaffected by Ag oxidation [6].

The interactions of Ag with I_2 and Ag_2O with $\Gamma(\text{aq})$ have also been investigated by Krausmann et al. [6]. They developed a model to investigate the influence of a variety of factors on the silver oxide to silver iodide reaction kinetics including: pH, temperature,

initial iodine and iodide concentration, and agitation of the test solution. Their model showed that the accumulation of AgI monolayers on top of the Ag₂O film was not rate limiting; therefore, diffusion or migration of either Ag(I) or I⁻ through the AgI film was not rate-limiting. This is in agreement with our results discussed in Chapter 4, section 4.4. The substrate in our work does differ, as we electrochemically oxidized the Ag electrode to a pre-determined degree, while they allowed an Ag mesh to air-oxidize, and were thus unable to determine the exact amount or surface area of the reactant, Ag₂O, for their model calculations. They reported a rate constant of $(8.2 \pm 3.6) \text{ mol}\cdot\text{m}^{-2}\cdot\text{s}^{-1}$ for the chemical reaction of Ag₂O with I⁻(aq) [6], which is approximately two orders of magnitude lower than the value obtained in this study. In our study, the rate constant was obtained using the geometric area of the electrode, and the true surface area may be many times larger than the geometric area due to roughening during Ag₂O film growth [7,8]. The difference between the rate constant reported by Krausmann et al. and what we have reported is still larger than the difference that we expect when the geometric vs. true surface area is taken into account. It should be noted that Krausmann et al. investigated the homogeneous reaction of Ag₂O powders/colloids dispersed in the aqueous phase with I⁻(aq) to form AgI, whereas the value we report is for the conversion of a Ag₂O film. These authors also concluded that pH had little to no effect on the reaction kinetics, which is somewhat surprising since the dissolution of Ag₂O increases by a factor of 10 with a pH change of ± 1.0 away from pH 12, where Ag₂O solubility is at a minimum [9].

Presently, we are not aware of any other reports using these particular techniques to examine the separate contributions of the interfacial chemical reaction kinetics and diffusion of a metal oxide-metal halide system. While there is a significant amount of

work available regarding the oxidation or reduction kinetics of small molecules or anions at metal surfaces [10,11], it appears that the techniques and the kinetic analysis used in this study are, in fact, a novel method for determining interfacial reaction kinetics.

5.5 *Summary and Conclusions*

The effect of mass transfer on the reaction kinetics was investigated by measuring the total reaction time as a function of electrode rotation rate. The total reaction time was found to be inversely proportional to the square root of the rotation rate, and extrapolation of the rotation rate dependence to infinite rotation enabled us to determine a surface chemical reaction rate with reasonable accuracy. This surface reaction rate constant was approximately an order of magnitude larger than the net conversion rate constant obtained under stagnant conditions (Chapter 4), indicating that the conversion is largely mass-transfer limited under stagnant conditions.

The influence of phosphate in electrolytes on the conversion reaction was also investigated. The surface reaction rate constant in phosphate solutions was approximately twice that in the absence of phosphate: $7.5 \times 10^{-2} \text{ cm}\cdot\text{s}^{-1}$ vs. $4.2 \times 10^{-2} \text{ cm}\cdot\text{s}^{-1}$. This difference is small, and is partially attributed to the difference in the initial surface area or surface structure ($A_{\text{Ag}_2\text{O}})_0$ of the Ag_2O films grown in the presence and absence of phosphate (Chapter 4, section 4.3.1). Although the XRD analysis results suggest the incorporation of phosphorous into the Ag_2O matrix during the initial anodic Ag_2O film growth in phosphate solutions, this study suggests that its presence does not seem to have any influence on the kinetics of the conversion.

5.6 *References*

1. A.J. Bard, L.R. Faulkner, *Electrochemical Methods: Fundamentals and Applications*, 2nd ed., John Wiley & Sons Inc., Hoboken, NJ, 2001, pp 337-339.
2. X. Zhang, S.D. Stewart, D.W. Shoesmith, and J.C. Wren, *J. Electrochem. Soc.*, **154**, F70 (2007).
3. S.D. Pretty, P.G. Keech, X.Zhang, J.J. Noël, and J.W. Wren, *Electrochim. Acta*, **56**, 2754 (2011).
4. S. Güntay, R.C. Cripps, B. Jäckel, and H. Bruchertseifer, *Nucl. Tech.*, **150**, 303 (2005).
5. R.S. Neves, E. De Robertis, and A.J. Motheo, *App. Surf. Sci.*, **253**, 1379 (2006).
6. E. Krausmann, and Y. Drossinos, *J. Nucl. Mat.*, **264**, 113 (1999).
7. V.I. Birss, and G.A. Wright, *Electrochim. Acta*, **27**, 1439 (1982).
8. B.M. Jovic, V.D. Jovic, and G.R. Stafford, *Electrochim. Commun.*, **1**, 247 (1999).
9. Lide, David R. (1998). *Handbook of Chemistry and Physics*, 87th ed., Boca Raton, FL: CRC Press. pp. 4–83.
10. G. Cohn, *Chem. Rev.*, **42**, 527 (1948).
11. M. Fleischmann, K. Korinek, D. Pletcher, *J. Chem. Soc., Perkin Trans. 2*, 1396 (1972).

Chapter 6

In Situ Conversion of Silver Oxide-Halide Films Studied by Neutron Reflectometry

6.1 Introduction

As described in Chapters 4 and 5, the surface reaction of $\Gamma(\text{aq})$ with Ag_2O to form AgI is fast and the net conversion under stagnant conditions is limited by diffusion of $\Gamma(\text{aq})$ to the oxide surface [1,2]. The observed dependences of the total reaction time on the concentration of $\Gamma(\text{aq})$ and the amount of Ag_2O initially present on the Ag substrate were successfully modeled using a simple reaction kinetic model.

Two key assumptions were made when developing the reaction kinetic model described in Chapter 4. The first assumption of a first order dependence on the concentration of $\Gamma(\text{aq})$ was easily verified by performing experiments as a function of $\Gamma(\text{aq})$ concentration. The second assumption was that the available Ag_2O surface area did not change as the reaction progressed, and that the Ag_2O surface area is proportional to the electrode surface area. This second assumption has led to the linear dependence of the total reaction time on the total charge used to grow the initial amount of Ag_2O . It was hypothesized that the surface area was constant because the conversion of Ag_2O to AgI proceeded mainly by the chemical reaction pathway, and the resulting AgI formed individual molecules, not a coherent solid AgI phase. Consequently, the AgI formed by this process does not protect the Ag_2O surface from reacting with $\Gamma(\text{aq})$.

The linear dependence of the total reaction time on the initial Ag_2O film thickness, and hence total anodic charge used to grow the film, suggested that conversion progressed in a layer-by-layer fashion. However, we have not been able to test the validity of the layer-by-layer

conversion using conventional surface analytical techniques because of the instability of AgI under light [3].

Other researchers have shown that specular neutron reflectometry (NR) is a powerful technique that can be used to study the structure of surfaces, thin films, or layered structures, and it can be used to investigate changes at surface interfaces (e.g., corrosion or adsorption/adhesion [4–13]). Hence, we have employed the use of NR to probe the Ag/Ag₂O/AgI interfaces during the conversion reaction to determine the relative locations of Ag₂O and AgI films formed during conversion of Ag₂O to AgI, as well as to identify, or rule out, participation by any other possible surface species (e.g., AgO or AgOH). If conversion occurs via a layer-by-layer mechanism as we have previously surmised [1,2], the neutron reflectometry results should be consistent with the presence of discrete Ag₂O/AgI layers. However, if conversion occurs in patches or through pores in the surface film, discrete layers would not be expected.

Additionally, we have been unsuccessful in determining the change in surface area (for example, due to surface roughening) that occurs during the anodic growth of Ag₂O on our starting Ag electrodes [1,2]. Currently, we use the geometric area of the electrode as the area of Ag₂O for modeling our experimental results. This is a known over-simplification, as researchers have shown that the Ag/Ag₂O electrode surface roughness increases significantly during Ag₂O film growth [14]. Neutron reflectometry is also a tool that can provide information on changes in the structure or compactness (density) of the oxide grown atop silver as a function of anodization time, which can be related to the effective surface area of the electrode.

Specular neutron reflectometry probes variations in the neutron scattering length density (SLD) perpendicular to the sample surface at depths up to 10s of microns [4–13]. Beyond the critical scattering vector (Q_c), i.e. the wave vector above which neutrons are partially reflected by

the sample, normalized reflectivity (R) is obtained by dividing the number of neutrons reflected from the sample by the number of neutrons incident upon the surface.

As prescribed by both kinematic approximation and dynamical scattering theory, the reflection of neutrons occurs at the interface of any two materials with different SLD values. The SLD is defined as the product ρb , where ρ is the density of atoms and b the coherent scattering length of a particular isotope [4–13]. The experimentally observable reflectivity of a sample depends on the variation in the SLD, which in turn is determined by the isotopic composition and density of the constituent layers. Characteristic Kiessig fringes will appear in the reflectivity, provided the sample consists of sufficiently flat interfaces. If a sample consists of many interfaces, then the reflectivity spectra will show modulations or fringes of several periodicities.

6.2 *Experimental Details*

6.2.1 *Stand-Alone Electrochemistry and XPS Measurements*

The working electrode was silver with a flat surface area 0.385 cm^2 . Electrodes were polished according to the polishing procedure described in Chapter 2, section 2.1.3. The electrolyte was $0.01 \text{ mol}\cdot\text{dm}^{-3}$ NaOH solution that was made using ultra-pure water and deaerated using argon for 60 min prior to an experiment. Prior to exposure to halide solutions, the reactant (Ag_2O film) was grown potentiostatically at $0.4 \text{ V}_{\text{SCE}}$ in the NaOH solution until the total charge, $(Q_{\text{Ag}_2\text{O}})_0$, reached 0.050 C . The Ag_2O -coated electrode was then transferred to a solution containing $\Gamma(\text{aq})$ or $\text{Cl}^-(\text{aq})$ and the E_{OC} was monitored. Two halide concentrations were used, $1 \times 10^{-3} \text{ mol}\cdot\text{dm}^{-3}$ and $5 \times 10^{-3} \text{ mol}\cdot\text{dm}^{-3}$. In a second experiment the Ag_2O -coated electrode was exposed to a NaOH solution containing equal amounts of $\Gamma(\text{aq})$ and $\text{Cl}^-(\text{aq})$ (at

$3 \times 10^{-3} \text{ mol}\cdot\text{dm}^{-3}$). The E_{OC} was monitored for 500 s, followed by a potential scan from 0.20 to $-1.1 \text{ V}_{\text{SCE}}$ at a scan rate of $0.17 \text{ mV}\cdot\text{s}^{-1}$ to obtain the cathodic stripping currents.

The XPS data was acquired on a KRATOS Axis Ultra spectrometer using monochromatic Al K_{α} radiation and operating at 150 W with a base pressure of 10^{-8} Pa. Under normal analysis conditions, the analysis spot size was approximately $400 \mu\text{m} \times 700 \mu\text{m}$. The binding energies were calibrated with respect to C-1s (285.0 eV). A broad spectrum survey determined the average surface composition and high resolution spectra were used to examine specific bands of 5 elements in detail: Ag-3d (at binding energies 368 and 374 eV), O-1s (530 eV), I-3d (619 eV), Cl-2p (198 eV) and C-1s (285 eV).

6.2.2 *Neutron Reflectometry Coupled with In Situ Electrochemistry*

A thin-film silver working electrode was prepared specially for the neutron reflectometry measurements by magnetron sputtering of metallic Ag, in an Ar atmosphere. To prevent delamination of the resulting silver film from the circular, phosphorous-doped Si(111) wafer substrate (6 mm thick and 10 cm in diameter), the wafer was prepared with an initial thin layer of Cr sputtered at a rate of $0.03 \text{ \AA}\cdot\text{s}^{-1}$ to a thickness of 20 \AA . The thin silver film of thickness $\sim 600 \text{ \AA}$ was then sputter deposited at a rate of $1 \text{ \AA}\cdot\text{s}^{-1}$. This electrode was exposed to ambient air when it was removed from the sputtering chamber and no attempt was made to prevent oxide/hydroxide formation on the silver surface.

A schematic of the electrochemical cell used for the reflectometry experiments is shown in Figure 6.1. A cylindrically machined PTFE cell was clamped to the Ag working electrode and electrical contact was made via a platinum foil placed between the O-ring seal of the PTFE cell

and the Ag electrode surface. NR scans were recorded prior to, and after, the addition of $0.01 \text{ mol}\cdot\text{dm}^{-3}$ of the NaOH electrolyte solution to the electrochemical cell.

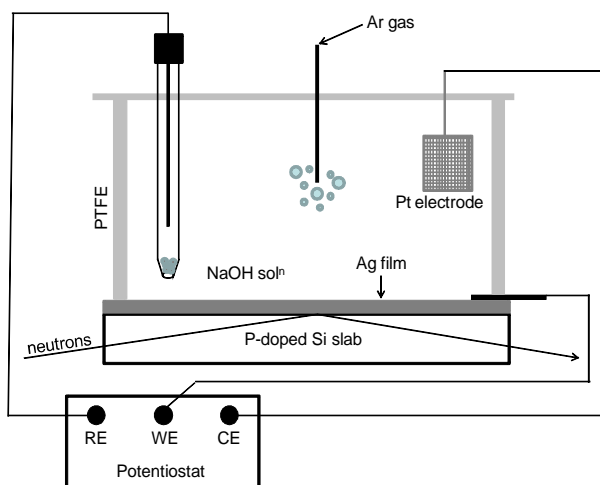


Figure 6.1 A schematic view of the experimental set-up used during the in situ neutron reflectometry experiments. The set-up was designed to study a Ag thin film, sputter deposited on a conductive Si slab on one side and exposed to a liquid medium on the other side.

The experiment consisted of two parts: (1) the anodic growth of an Ag_2O film, and (2) exposure of this Ag_2O film to an $\Gamma(\text{aq})$ solution (shown schematically in Figure 6.2). NR scans were recorded throughout the anodic growth of the Ag_2O film at $0.25 \text{ V}_{\text{SCE}}$ at 100, 200, 700 and 1200 s (as indicated by * in Figure 6.2). After oxide growth $\Gamma(\text{aq})$ was added to a concentration of $1 \times 10^{-5} \text{ mol}\cdot\text{dm}^{-3}$. The E_{OC} was continuously monitored and NR scans were recorded every 15 min. After 8 h the electrode potential was scanned from 0.2 to $-1.1 \text{ V}_{\text{SCE}}$ at $0.50 \text{ mV}\cdot\text{s}^{-1}$ and the cathodic stripping current was measured. A final NR scan was recorded after the complete reduction of the Ag films. All electrochemical control was maintained using an Autolab PGSTAT128N potentiostat.

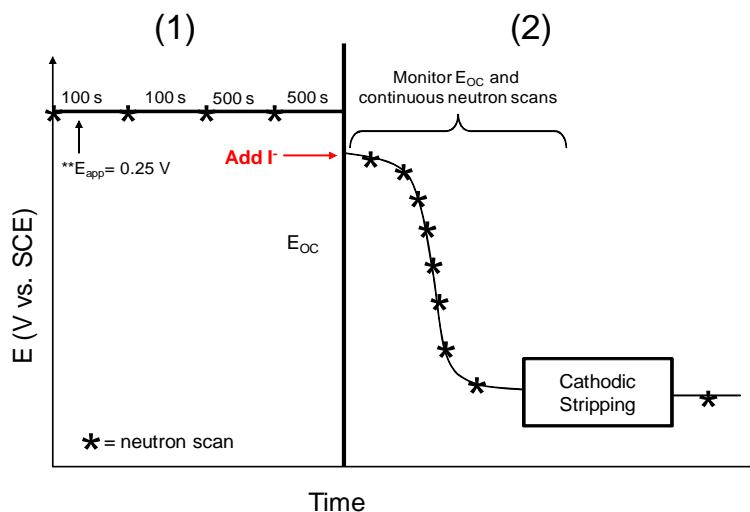


Figure 6.2 Potential vs. time plot of the experimental approach used to study: (1) the anodic growth of Ag_2O , and (2) the chemical reaction of a Ag_2O film with $\Gamma(\text{aq})$ resulting in the formation of a AgI film. Each * on the plot represents the time at which a neutron scan was initiated.

Reflectivity measurements were carried out on the Platypus time-of-flight reflectometer, at the Bragg Institute, Australian Nuclear Science and Technology Organisation (ANSTO) in Sydney, Australia. This time-of-flight instrument, with 20 Hz neutron pulse frequencies, was operated in the medium resolution mode ($\Delta\lambda/\lambda = 4.3\%$) and reflected neutrons were recorded on a 2-dimensional helium-3 detector, with an active area 500 mm wide \times 250 mm high. In order to achieve sufficient dynamic range, data was collected at two incident grazing angles: $\theta = 0.6^\circ$ for 5 min and $\theta = 2.4^\circ$ for 10 min. The total collection time for each NR scan was 15 minutes, and in some cases, these 15 minute scans have been added together and averaged in order to reduce the measurement error. Reduction and analysis of the data, as log normalized reflectivity (R) vs. scattering vector (Q_z), was performed with Motofit reflectometry analysis software. A more detailed description of the complete instrumentation, data collection, and analysis techniques can be found in Chapter 2, section 2.4.4.

The NR results are analyzed by comparing the observed reflectivity to a proposed model profile, where each discrete layer/interface is represented in the model. There are three adjustable parameters per layer: SLD, thickness, and roughness of the interface to the adjacent layer in the model. Least-squares refinement is used to minimize the differences between the calculated and measured reflectivity. A scattering length density profile graphically shows the thickness, roughness, and relative position of discrete layers that are incorporated into the model. The as-prepared Ag film was first examined with x-ray reflectometry to ensure sample quality (free of macroscopic bending and of sufficiently sharp interfaces) and further characterized by X-ray photoelectron spectroscopy (XPS) prior to electrochemical treatment. A Hitachi S-4500 field emission scanning electron microscope (SEM) was used to examine the morphology of the Ag electrode following cathodic stripping, as a compliment to neutron reflectometry measurements.

6.3 *Results and Discussion*

6.3.1 *Neutron Reflectometry – As-Prepared Film*

One aspect of non-linear least-squares fitting is that the model it yields may not be correct if the refinement has converged to a false minimum. Mindful of this possibility, we have chosen to propose a model that is simplest (i.e. no additional features unless they actually lead to a significantly better fit), and consistent with results obtained from other thin-film and surface characterization techniques [1,2]. For instance, we propose the outermost layer as AgOH instead of Ag₂O or other oxides since XPS results described below indicate the presence of hydroxide.

To obtain a baseline for later measurements, the as-prepared Ag film on the Si substrate was characterized using NR prior to electrolyte exposure. The model for the layering on the as-prepared sample consists of Si as the incident medium, a layer of metallic Ag, a layer of AgOH, and air. The SLD values for all relevant species used during the fitting procedure corresponded with the expected (calculated) values. In order to obtain information that confirms or disputes the hypothesis that conversion occurs by a layer-by-layer process, a second fitting of the data will be completed where variance in the SLD values will be allowed. Therefore, the results presented here are preliminary.

Notably absent from the proposed layer profile are: (1) an expected thin SiO₂ layer located between the Si and Cr layers, and (2) the Cr layer that was deposited on Si before the Ag layer. Inclusion of these layers did not improve the fit of the model, indicating that they are too thin to be resolved with our data that reaches a maximum scattering vector of $Q_{\max} = 0.15 \text{ \AA}^{-1}$. Resolution between films can also be lost if the two materials have similar SLD values. Consequently, they are “hidden” within the relatively broad interface ($\sim 50 \text{ \AA}$) between Ag and Si in our model.

Figure 6.3 shows the layer profile corresponding to the best-fit model of the Ag electrode in air. The measured (black symbols with error bars of 1 estimated standard deviation (e.s.d.)) and calculated (red curve) reflectivity for the least-squares refined model are shown in the inset. The numerical values for all of the fitting parameters (film thickness, SLD, and interface roughness) are given in Table 6.1. The error listed represents 1 e.s.d. for parameters that were allowed to vary during the fitting procedure while those held constant (e.g. the SLD of Si) appear without errors.

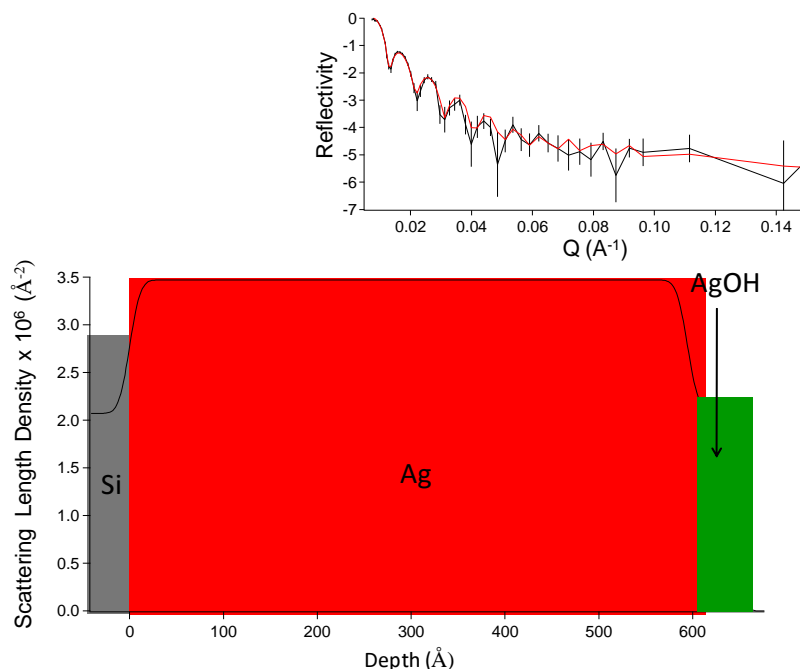


Figure 6.3 Least-squares fitted SLD profile of the as-prepared sample. The numerical parameters of the model, consisting of four distinct layered species: Si, Ag, AgOH and air are given in Table 6.1. The normalized neutron reflectivity spectra of the sample (black line) and proposed model (red line) are inset to the SLD profile. Graphical representation for the layer thicknesses for this specimen is indicated within Figure 6.5 by ❶.

Table 6.1 Numerical parameters of the least squares fitted model representing the as-prepared sample in air, electrolyte, and throughout step-wise anodization. Non-variable parameters are indicated in bold, and an uncertainty is given for the variable parameters, the infinity symbol is used for all layers with thickness assumed > 300 – 500 nm. The results are plotted graphically in Figure 6.5.

Condition	Layer	SLD $\rho b \times 10^6$ (\AA^{-2})	Layer thickness (\AA)	Interface thickness (\AA)
As-prepared, in air	Si	2.07	∞	5.5
	Ag	3.47	601 ± 4	13 ± 8
	Ag ₂ O	3.27	0	0
	AgOH	2.1	51 ± 5	14 ± 8
	Air	0	∞	
In solution, at E _{OC}	Si	2.07	∞	5.5
	Ag	3.47	604 ± 7	13 ± 8
	Ag ₂ O	3.27	0	0
	AgOH	2.1	39 ± 11	38 ± 10
	Water	-0.55	∞	

100 s polarization	Si	2.07	∞	5.5
	Ag	3.47	582 ± 9	13 ± 6
	Ag ₂ O	3.27	39 ± 2	–
	AgOH	2.1	12 ± 1	64 ± 5
	Water	-0.55	∞	
200 s polarization	Si	2.07	∞	5.5
	Ag	3.47	522 ± 16	16 ± 5
	Ag ₂ O	3.27	99 ± 23	–
	AgOH	2.1	10 ± 8	61 ± 6
	Water	-0.55	∞	
700 s polarization	Si	2.07	∞	5.5
	Ag	3.47	411 ± 13	24 ± 4
	Ag ₂ O	3.27	199 ± 21	–
	AgOH	2.1	29 ± 15	60 ± 12
	Water	-0.55	∞	
1200 s polarization	Si	2.07	∞	5.5
	Ag	3.47	410 ± 13	41 ± 5
	Ag ₂ O	3.27	207 ± 41	–
	AgOH	2.1	15 ± 4	100 ± 9
	Water	-0.55	∞	

Analysis by XPS supports our inclusion of a AgOH layer on the as-prepared sample surface in our model. This feature has also been observed and extensively discussed in literature [15–22]. Figure 6.4 shows the survey spectra results, and characteristic peaks for Ag (3d), O (1s) and C (1s) are indicated on the plot. The narrow Ag 3d peak at 368.1 eV is due to the presence of predominantly metallic Ag [15]. Deconvolution of this peak into Ag and Ag₂O signals showed a small amount of oxidized Ag. Deconvolution produced a ratio of 93:7 for Ag:Ag₂O. Unfortunately, the small separation between Ag and Ag₂O, and the location of AgOH between these positions, makes quantifying the amounts of each species (Ag/AgOH/Ag₂O) difficult.

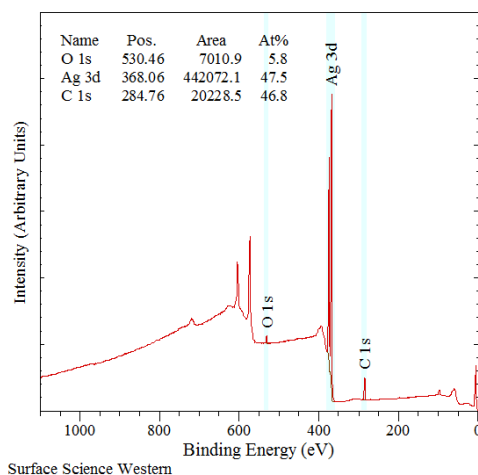


Figure 6.4 XPS survey spectra of the as-prepared Ag sample after sputter deposition.

6.3.2 Neutron Reflectometry – As-Prepared Film in Solution at E_{OC}

The reflectivity of the silver electrode in NaOH at E_{OC} was very similar to that of the air-exposed electrode. The same model employed in Figure 6.3 was used for the wet sample, with the air layer replaced by a water layer (compare first two bars in Figure 6.5). The fitting results (layer thickness, roughness, and SLD values) are tabulated in Table 6.1 and plotted in Figure 6.5, where each bar represents a specific experimental condition and each layer thickness and roughness was given a unique colour and pattern. The bulk materials (Ag, Ag_2O and AgOH) are represented by solid bars and the thatched bars represent roughness at the particular interface. The only observable difference between the sample exposed to air and initially exposed to solution was a slight increase in the AgOH layer roughness observed after the addition of NaOH. We have postulated that the increase in roughness of the AgOH interface after wetting was likely due to swelling caused by hydration of the outer AgOH film.

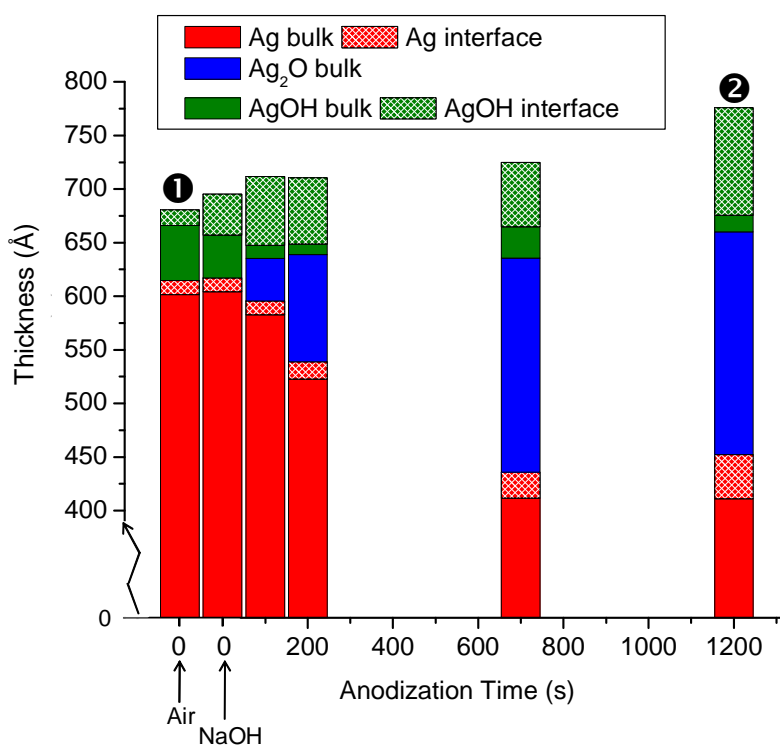


Figure 6.5 Graphical representation of the numerical values presented in Table 6.1 indicating the progression of Ag₂O film growth. For simplicity, only the upper three (of the five) distinct layers are shown: Ag (red), Ag₂O (blue) and AgOH (green). The Si and air/water layer remain constant and are not represented here.

6.3.3 *In Situ Ag₂O Film Growth*

Neutron reflectivity scans were recorded while a Ag₂O film was grown electrochemically after each anodization step to monitor the progression of Ag₂O film growth. The bar graph in Figure 6.5 allows for easy visualization of how the film thickness changed as a function of anodization time.

Anodization at 0.25 V_{SCE}, a value slightly above $(E^e)_{Ag_2O/Ag}$, results in the conversion of Ag to Ag₂O via the following electrochemical reaction [14,23–27]:



A second electrochemical reaction, namely the formation of AgOH via the following reaction:



proposed by Nagle et al. may also occur at this potential [27]. In equation (6.2) Ag^* is defined as high energy, superactive, surface metal atoms [27]. The key finding in Nagle et al.'s study was that an outer AgOH layer, formed via the process in equation (6.2), was extremely porous.

Hence, subsequent Ag_2O formation was not expected to be hindered by the presence of this AgOH film. Our NR results are consistent with Nagle's AgOH outer layer, since they show that Ag_2O grows below a rough ($\sim 40 \text{ \AA}$) AgOH film.

Figure 6.6 shows the SLD profile, and observed (black line) and calculated (red line) reflectivity for the Ag film at the completion of anodization. This is the last of the four steps of anodization, shown as an example. Although only one reflectometry result is shown, all least-squares fitted parameters for each anodization step are listed in Table 6.1. Our model of the electrode surface consists of five layers: Si, metallic Ag, Ag_2O , AgOH, and water. Figure 6.5 shows how the thicknesses of these layers change during the anodization process. After 1200 s of anodization the Ag thickness markedly decreased (by $\sim 200 \text{ \AA}$) and the Ag_2O thickness increased by a similar amount ($\sim 200 \text{ \AA}$). The total AgOH thickness varied slightly, but compared to Ag and Ag_2O was considered to remain nearly constant throughout the duration of the anodization process.

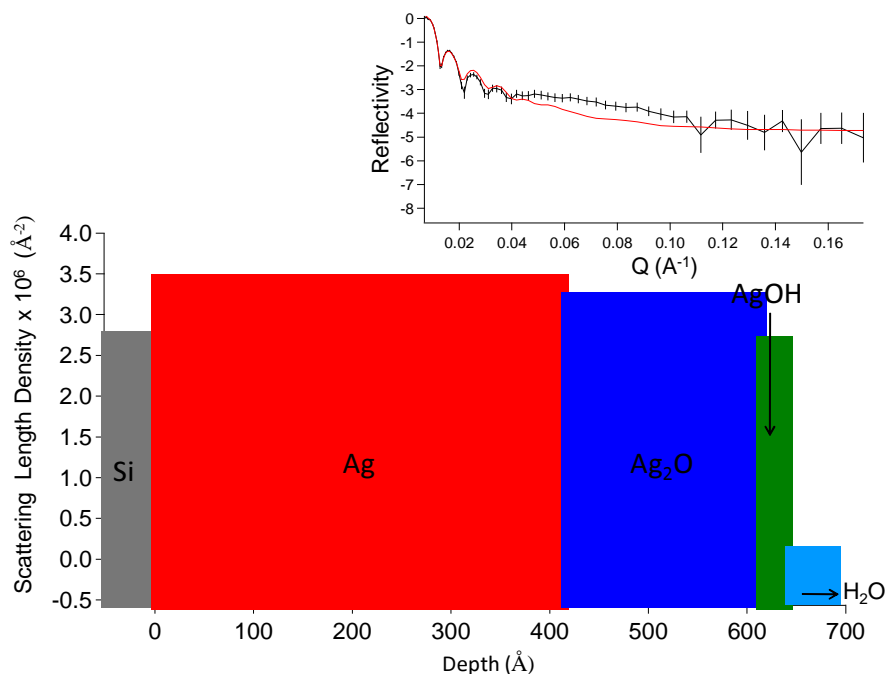


Figure 6.6 SLD profile and normalized reflected neutron counts (black line) and calculated reflectivity (red line) for the Ag film at the completion of 1200 s anodization. Graphical representation for the layer thicknesses for this specimen is indicated within Figure 6.5 by ②, and numerical values are given in Table 6.1.

The Pilling-Bedworth ratio for a metal-oxide is given by:

$$R_{PB} = \frac{V_{oxide}}{V_{metal}} = \frac{M_{oxide} \cdot \rho_{metal}}{n \cdot M_{metal} \cdot \rho_{oxide}} \quad (6.3)$$

where M is the molar mass, ρ the density, and V the molar volume, of oxide or metal respectively, and n is the number of atoms of metal per molecule of oxide [28]. The calculated R_{PB} for Ag_2O is 1.58. Using this ratio, one can estimate the change in oxide thickness that would correspond to the consumption of a certain thickness of Ag metal. The loss of 200 Å of Ag should lead to the formation of 316 Å of Ag_2O . However, we measured (based on model analysis of the NR results) an Ag_2O film thickness of 200 Å. This suggests that almost one-third of the oxidized Ag was lost to dissolution.

Previous researchers have observed a significant increase in Ag roughness after the formation of Ag₂O by electrochemical anodization [14, 23–26], which is consistent with the results presented in Table 6.1. The measured neutron reflectometry results show an almost four-fold increase in Ag film roughness at the completion of anodization. Additionally, the roughness of the AgOH interface increased from 40 to 100 Å. Unfortunately, the proposed model was not sensitive to changes in roughness at the Ag₂O/AgOH interface; therefore, we cannot determine exactly how the Ag₂O roughness changed as a function of anodization time.

In addition to being in good agreement with observed reflectivity, the proposed model leads to results that make sense chemically. The number of moles of metallic Ag consumed and the number of moles of Ag₂O produced can be calculated from film thicknesses (obtained from NR data), sample surface area, density, and molar mass of each species. The amount of Ag consumed was found to be 1.1×10^{-5} mol and the amount of Ag₂O formed was found to be 3.8×10^{-6} mol. This gives a Ag:Ag₂O ratio of 2.9:1. This ratio is likely higher than the expected 2:1 ratio due to dissolution of some of the oxidized Ag.

6.3.4 *In Situ Conversion of Ag₂O to AgI*

After the anodic growth of a Ag₂O layer, I⁻(aq) was added to the electrochemical cell to initiate the conversion of Ag₂O to AgI. The E_{OC} was monitored while the conversion reaction occurred and NR scans were acquired continually for the next 8 hours. The most dramatic changes in reflectivity were observed in the first 45 minutes after the addition of I⁻(aq). All of the reflectivity scans collected over the course of the remainder of the 8-hour experiment looked very similar. For this reason only one SLD profile and reflectivity scan are presented in Figure

6.7. The reflectivity plot is the sum of 6 scans recorded over a 1.5-hour period, beginning after the large transition in E_{OC} , when the chemical system had nearly achieved a steady-state.

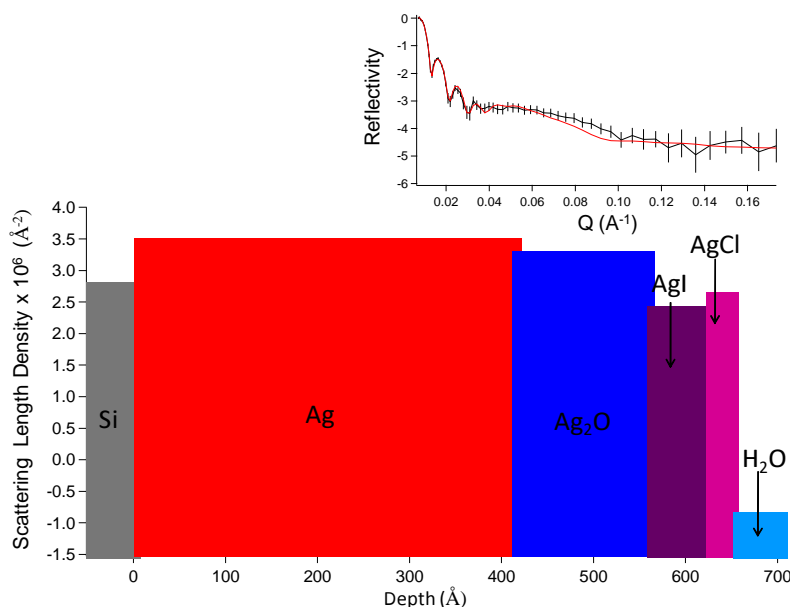


Figure 6.7 SLD profile of the Ag electrode recorded in $1 \times 10^{-5} \text{ mol}\cdot\text{dm}^{-3}$ of $\Gamma(\text{aq})$. The observed neutron reflectivity spectrum (black line) and the predictions of our proposed model (red line) with five distinct layers is inset. Graphical representation for the layer thicknesses for this specimen is indicated within Figure 6.8 by **⑤**, and numerical values are given in Table 6.2.

The model that was used to analyze the reflectivity data consists of Si substrate (incident medium encountered by neutrons), a metallic Ag film, a Ag_2O film, a AgI film, a AgCl film, and water. The AgCl film is necessary because an unknown amount of $\text{Cl}^-(\text{aq})$ was released from the SCE reference electrode into the cell solution and this resulted in the conversion of some Ag_2O to AgCl. The time at which $\text{Cl}^-(\text{aq})$ leaked into the cell is not known. Inclusion of a AgCl layer used to model the surface during Ag_2O film growth led to a significant increase in error between the measured and calculated reflectivity profiles, hence it was not included in the model.

The minimum concentration of $\text{Cl}^{\text{-(aq)}}$ that would result in $(E^e)_{\text{AgCl}/\text{Ag}} < (E^e)_{\text{Ag}_2\text{O}/\text{Ag}}$ is $3 \times 10^{-4} \text{ mol}\cdot\text{dm}^{-3}$. This corresponds to an $(E^e)_{\text{AgCl}/\text{Ag}}$ of 0.19 V_{SCE}. Release of only 15 μL of solution from the SCE electrode would be sufficient to exceed the minimum $\text{Cl}^{\text{-(aq)}}$ concentration required for Ag_2O conversion to AgCl . The volume of solution that leaked from SCE was visibly apparent, and regions of the Ag electrode close to the reference electrode appeared tarnished or blackened. The sequence of the layers (i.e., AgI on AgCl vs. AgCl on AgI) was easily determined by NR because the SLD values for AgCl ($3.68 \times 10^6 \text{ \AA}^{-2}$) and AgI ($1.53 \times 10^6 \text{ \AA}^{-2}$) are different enough that the layers can clearly be distinguished.

Changes to the layered species on the electrode surface as a function of exposure time are shown in Figure 6.8 and SLD, thickness, and roughness data for each layer are tabulated in Table 6.2. A decrease in the Ag_2O layer thickness from 207 to 140 \AA was observed within the first 15 minutes after the addition of the KI solution to the electrochemical cell. The Ag_2O layer thickness remained constant for the remainder of the experiment. An AgI film was added to the model on top of the Ag_2O , which resulted from the conversion of Ag_2O to AgI. The AgI layer had a thickness of 80 \AA and an average roughness of 15 \AA .

A 15 \AA -thick AgCl layer was added to the model after 30 minutes of E_{OC} measurement. This AgCl film may have formed by the precipitation of AgCl from the dissolved $\text{Ag}^{\text{(aq)}}$ (discussed in section 6.3.3) with $\text{Cl}^{\text{(aq)}}$ entering the solution from the leaking SCE. Fitting of the reflectivity data indicates that the AgCl film was rough (40 \AA). This nominal roughness may indicate the film formed unevenly or in patches over the electrode surface.

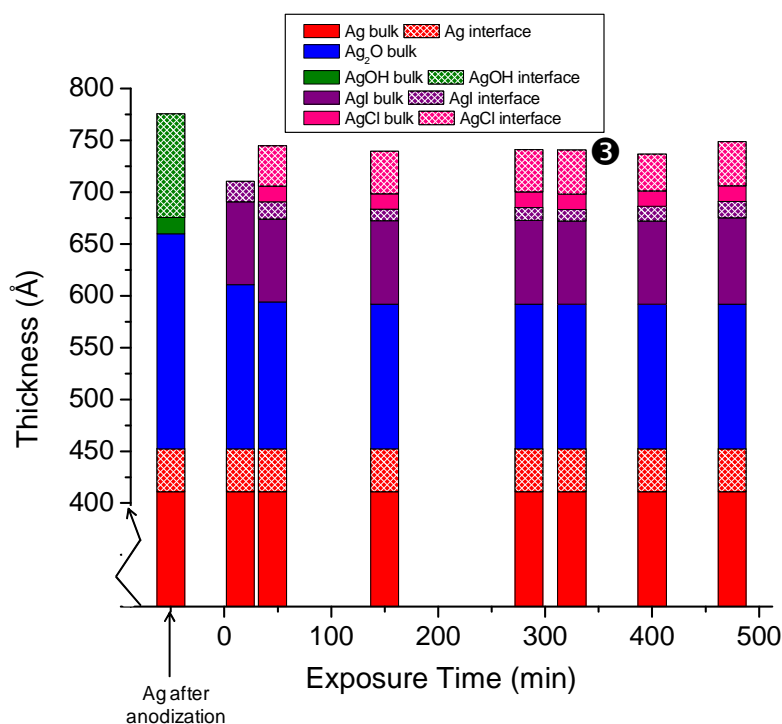


Figure 6.8 Graphical representation of the calculated Ag (red), Ag₂O (blue), AgI (purple), and AgCl (pink) thickness and roughness values after the addition of $\Gamma(\text{aq})$. The numerical values are given in Table 6.2.

Table 6.2 Numerical parameters of the least squares fitted model, representing the sample after the addition of KI. The model is shown in Figure 6.7, and the results are plotted graphically in Figure 6.8. Non-variable parameters are indicated in bold, and an uncertainty is given for variable parameters.

Condition	Layer	SLD $\rho b \times 10^6 (\text{\AA}^{-2})$	Layer thickness (\AA)	Interface thickness (\AA)
15 min exposure	Si	2.07	∞	5.5
	Ag	3.47	410	41
	Ag ₂ O	3.27	158 ± 7	–
	AgI	1.53	80 ± 5	19 ± 1
	Water	-0.55	∞	
30 min exposure	Si	2.07	∞	5.5
	Ag	3.47	410	41
	Ag ₂ O	3.27	141 ± 12	–
	AgI	1.53	80 ± 3	16 ± 12
	AgCl	3.68	15	38 ± 12

	Water	-0.55	∞	
150 min exposure	Si	2.07	∞	5.5
	Ag	3.47	410	41
	Ag ₂ O	3.27	139 ± 3	–
	AgI	1.53	80 ± 2	11 ± 4
	AgCl	3.68	15	41 ± 3
	Water	-0.55	∞	
255 min exposure	Si	2.07	∞	5.5
	Ag	3.47	410	41
	Ag ₂ O	3.27	139 ± 3	–
	AgI	1.53	80 ± 2	12 ± 4
	AgCl	3.68	15	41 ± 3
	Water	-0.55	∞	
345 min exposure	Si	2.07	∞	5.5
	Ag	3.47	410	41
	Ag ₂ O	3.27	139 ± 4	–
	AgI	1.53	80 ± 2	11 ± 6
	AgCl	3.68	15	42 ± 4
	Water	-0.55	∞	
420 min exposure	Si	2.07	∞	5.5
	Ag	3.47	410	41
	Ag ₂ O	3.27	139 ± 4	–
	AgI	1.53	83 ± 2	14 ± 5
	AgCl	3.68	15	35 ± 4
	Water	-0.55	∞	
495 min exposure	Si	2.07	∞	5.5
	Ag	3.47	410	41
	Ag ₂ O	3.27	139 ± 3	–
	AgI	1.53	83 ± 2	15 ± 4
	AgCl	3.68	15	42 ± 3
	Water	-0.55	∞	

Cathodic stripping voltammetry was performed at the end of the experiment and the results showed the presence of two poorly-separated cathodic reduction peaks (Figure 6.9). The more positive reduction peak centered around 0.00 V_{SCE} was attributed to the reduction of Ag₂O

to Ag and the more negative peak at -0.20 V_{SCE} was due to the reduction of AgI to Ag. Poor separation of the cathodic reduction peaks may have resulted from contamination by Cl^- (aq), since the reduction of AgCl occurred at a potential between $(E^e)_{\text{Ag}_2\text{O}/\text{Ag}}$ and $(E^e)_{\text{AgI}/\text{Ag}}$, as shown in the cyclic voltammograms discussed in Chapter 3, section 3.3.5 [29–31]. The amount of $\text{Ag}_2\text{O}/\text{AgCl}$ and AgI was estimated from the voltammogram, however due to the closeness of $(E^e)_{\text{Ag}_2\text{O}/\text{Ag}}$ to $(E^e)_{\text{AgCl}/\text{Ag}}$, the amount of Ag_2O and AgCl could not be distinguished by this method. This result also indicated that the conversion reaction did not go to completion and unreacted Ag_2O was still present on the electrode surface.

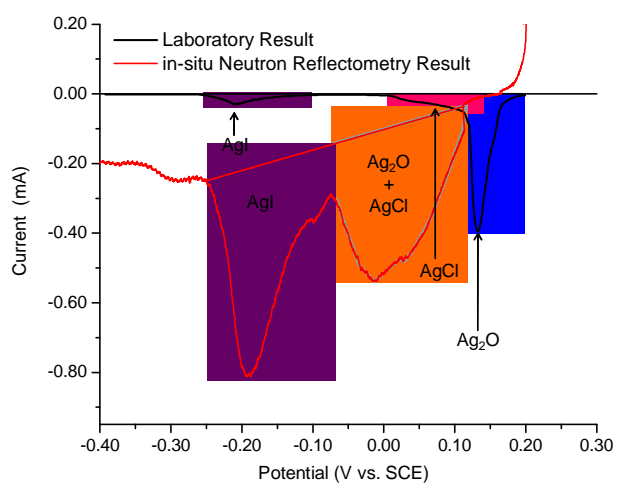


Figure 6.9 Cathodic stripping voltammogram recorded at the completion of the experiment. The concentration of $\Gamma^-(\text{aq})$ was 1×10^{-5} mol·dm⁻³ (red line, NR results). Cathodic stripping result recorded after a Ag_2O film with $(Q_{\text{Ag}_2\text{O}})_0$ 0.050 C was exposed to a solution containing 3×10^{-3} mol·dm⁻³ of $\Gamma^-(\text{aq})$ and 3×10^{-3} mol·dm⁻³ of Cl^- (aq) (black line).

Due to the contamination observed during NR measurements a second cathodic stripping measurement was performed on a bulk Ag electrode (used for all other electrochemical experiments). An Ag_2O film was exposed to a solution containing a mixture of $\Gamma^-(\text{aq})$ and

$\text{Cl}^-(\text{aq})$. The reaction was terminated by removing the electrode from the halide-containing solution after 500 s, rinsing it with water, placing it in a NaOH solution, and cathodically reducing the films present on the Ag surface (Figure 6.9). The large cathodic peak (at $0.15 \text{ V}_{\text{SCE}}$) corresponds to the reduction of Ag_2O to Ag. The very small peak at $-0.2 \text{ V}_{\text{SCE}}$ is due to reduction of AgI to Ag and the small shoulder on the Ag_2O peak (at $\sim 0.1 \text{ V}_{\text{SCE}}$) was attributed to the reduction of AgCl to Ag. This agrees well with the CVs presented in Chapter 3, section 3.3.5 [29–31] and indicates that the electrochemical behaviour of the thin-film sample is similar to that of a bulk Ag sample.

These results also show that both AgI and AgCl films are formed concurrently. The AgCl film appears to be thinner than the AgI film (based on the areas, or estimated charges, of the cathodic peaks). However, quantifying the amount of AgCl present is not possible from this scan because of the overlap with the larger Ag_2O peak. The thinner AgCl film is expected because the rate of conversion of Ag_2O to AgCl is ~ 2.5 times slower than the rate of conversion of Ag_2O to AgI, as determined by the E_{OC} profiles shown in Figure 6.10.

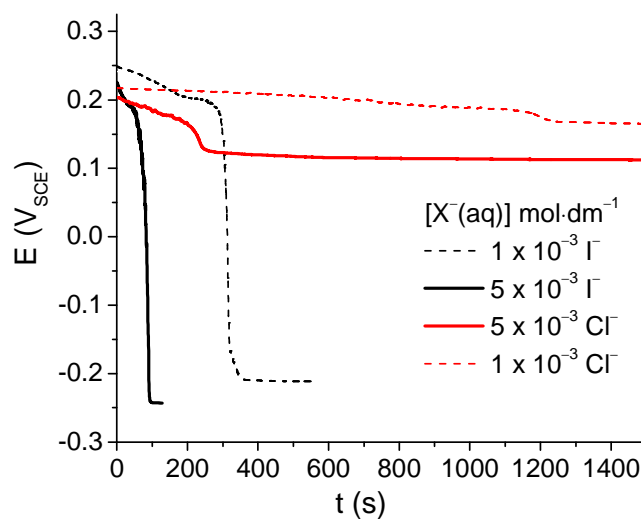


Figure 6.10 Open-circuit potential for a Ag_2O oxide grown at $0.4 \text{ V}_{\text{SCE}}$ to a constant anodic charge $(Q_{\text{Ag}_2\text{O}})_0$ of 0.050 C . The Ag_2O film was exposed to solutions containing 1) $5 \times 10^{-3} \text{ mol}\cdot\text{dm}^{-3} \text{ I}^-(\text{aq})$ (black solid line), 2) $1 \times 10^{-4} \text{ mol}\cdot\text{dm}^{-3} \text{ I}^-(\text{aq})$ (black dashed line), 3) $5 \times 10^{-3} \text{ mol}\cdot\text{dm}^{-3} \text{ Cl}^-(\text{aq})$ (red solid line) and 4) $1 \times 10^{-4} \text{ mol}\cdot\text{dm}^{-3} \text{ Cl}^-(\text{aq})$ (red dashed line).

The amounts of Ag_2O , AgCl and AgI present on the surface calculated from the NR results and cathodic stripping analyses are given in Table 6.3. As mentioned earlier, the reduction of Ag_2O cannot be distinguished from the reduction of AgCl and a combined value is given for these species. The NR and electrochemical results agree quite well. The total amount of Ag from Ag_2O , AgCl and AgI determined from NR was $6.8 \times 10^{-6} \text{ mol}$ and that determined by cathodic stripping was $7.4 \times 10^{-6} \text{ mol}$. These values are both close to the amount of silver initially oxidized to Ag_2O ($7.6 \times 10^{-6} \text{ mol}$). The measured post-test film quantities are slightly smaller due to dissolutive losses of Ag_2O . The close agreement between all of these values shows that we have a good understanding of the silver film and its reactions.

Table 6.3 Summary of the calculated amount of Ag_2O , AgI and AgCl from the NR experiment using: 1) neutron reflectometry (top block) 2) cathodic stripping voltammetry (centre block) and 3) a comparison of the amount of Ag in the film calculated from NR, cathodic stripping voltammetry and the initial Ag_2O film growth (bottom block).

Neutron Reflectometry			
Species	Ag_2O	AgCl	AgI
Film Thickness (\AA)	140	15	80
Amount (mol)	2.6×10^{-6}	3.5×10^{-7}	1.2×10^{-6}
Amount Ag (mol)	5.2×10^{-6}	3.5×10^{-7}	1.2×10^{-6}
Total Amount of Ag (mol)		6.8×10^{-6}	
Cathodic Stripping Voltammetry			
Species	Ag_2O	AgI	

Charge (mC)	347	373
Amount Ag (mol)	3.6×10^{-6}	3.8×10^{-6}
Total Amount of Ag (mol)	7.4×10^{-6}	
Comparison of Neutron Reflectometry and Cathodic Stripping Voltammetry		
Amount of Ag from Cathodic Stripping (mol)	7.4×10^{-6}	
Amount of Ag from Neutron Reflectometry (mol)	6.8×10^{-6}	
Amount of Ag Initially Anodized (mol)	7.6×10^{-6}	

A final NR scan on the reduced electrode was collected after cathodic stripping, however, the spectrum was featureless. SEM micrographs (Figure 6.11) taken after the Ag electrode was cathodically stripped show that the electrode surface was covered with very fine particulates. Cathodic reduction led to an increase in surface roughness that was uniform over the entire electrode surface.

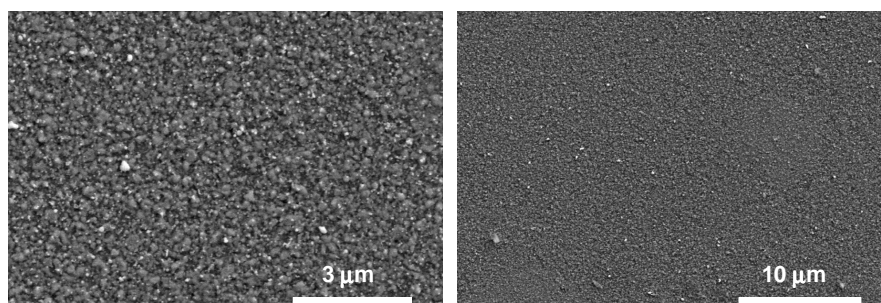


Figure 6.11 SEM image of the Ag thin film electrode after Ag_2O film growth, film conversion and cathodic stripping.

6.4 Conclusions

We have shown that the progression of the anodic growth of a Ag_2O film on an Ag substrate can be followed successfully using neutron reflectometry. The anodization of a Ag

film in a NaOH solution results in the growth of an inner Ag₂O film with a rough AgOH outer layer. We cannot extract changes in the roughness of the Ag₂O film as it grows, but our preliminary results show an increase in roughness of the AgOH film at the water interface and a much smaller change in roughness at the Ag/Ag₂O interface. If these findings are confirmed after re-analysis of the data, they provide a basis for modifying the effective surface used in kinetic models of electrochemistry on silver electrodes.

Neutron reflectometry has also been used effectively to study the conversion of AgOH/Ag₂O to AgI. Our preliminary NR results show that distinct Ag₂O and AgI layers are present on the electrode surface. This confirms the conversion process that we had previously postulated based only on our prior electrochemistry studies. We would like to confirm this by removing the restriction that the SLD values are exactly equal to the calculated values. Changes in the SLD values away from calculated values can provide information that will further our understanding of the film conversion process. For example, a decrease in the Ag₂O SLD as the reaction progresses may indicate diffusion of $\Gamma(\text{aq})$ through the film to the Ag substrate.

6.5 References

1. X. Zhang, S.D. Stewart, D.W. Shoesmith, and J.C. Wren, *J. Electrochem. Soc.*, **154**, F70 (2007).
2. S. Pretty, P.G. Keech, X. Zhang, J.J. Noël, and J.C. Wren, *Electrochim. Acta*, **56**, 2754 (2011).
3. S.E. Reynolds, W. Hume, B. Vonnegut, and J.V. Schaefer, *Bull. Am. Meteor. Soc.*, **32**, 47 (1951).
4. Z. Tun, J.J. Noël and D.W. Shoesmith, *J. Electrochem. Soc.*, **146**, 988 (1999).
5. J.J. Noël, H.L. Jensen, Z. Tun and D.W. Shoesmith, *Electrochem. Solid-State Lett.*, **3**, 473 (2000).

6. Z. Tun, J.J. Noël and D.W. Shoesmith, *Pramana – J. Phys.*, **71**, 769 (2008).
7. J.J. Noël, B.M. Ikeda, N.H. Miller, S.R. Ryan, D.W. Shoesmith, S. Sunder and Z. Tun, *Electrochem. Soc. Proc.*, **96**, 246 (1996).
8. M. James, A. Nelson, J.C. Shulz, M.J. Jones, A.J. Studer and P. Hathaway, *Nucl. Instr. and Meth. Phys. A*, **536**, 165 (2005).
9. M. James, A. Nelson, S.A. Holt, T. Saerbeck, W.A. Hamilton and F. Klose, *Nucl. Instr. and Meth. Phys. A*, **632**, 112 (2011).
10. A. Nelson, *J. App. Crsyt.*, **39**, 273 (2006).
11. A.S. Brown, S.A. Holt, P.M. Saville and J.C. White, *Aust. J. Phys.*, **50**, 391 (1997).
12. J. Penfold, R.M. Richardson, A. Zorbakhsh, J.R.P. Webster, D.G. Bucknall, A.R. Rennie, R.A.L. Jones, T. Cosgrove, R.K. Thomas, J.S. Higgins, P.D.I. Fletcher, E. Dickinson, S.J. Roser, I.A. McLure, A.R. Hillman, R.W. Richards, E.J. Staples, A.N. Burgess, E.A. Simister and J.W. White, *J. Chem. Faraday Trans.*, **93** 3899 (1997).
13. R.K. Thomas, *Curr. Opin. Solid State Mater. Sci.*, **1**, 636 (1996).
14. B.M. Jovic, V.D. Jovic, and B.R. Stafford, *Electrochem. Commun.*, **1**, 247 (1999).
15. J.M.M. Droog, P.T. Alderliesten, and G.A. Bootsma, *J. Electroanal. Chem.*, **99**, 173 (1979).
16. M. Lopez Teijelo, J.R. Vilche and A.J. Arvia, *J. Electroanal. Chem.*, **131**, 331 (1982).
17. M. Lopez Teijelo, J.R. Vilche and A.J. Arvia, *J. Electroanal. Chem.*, **162**, 207 (1984).
18. R.H. Müller and C.G. Smith, *Surf. Sci.*, **96**, 375 (1980).
19. M.F. Kuhali, *J. Phys. D. Appl. Phys.*, **40**, 2847 (2007).
20. M. Biemann, P. Schwaller, P. Ruffieux, O. Gröning, L. Schlapbach, and P. Gröning, *Phys. Rev. B*, **65**, 65 (2002).
21. D. Hecht, and H.-H. Strehblow, *J. Electroanal. Chem.*, **436**, 109 (1997).
22. D. Lutzenkirchen-Hechta, and H.-H. Strehblow, *Electrochim. Acta*, **43**, 2957 (1998).
23. T.U. Hur, and W.S. Chung, *J. Electrochem. Soc.*, **152**, A996 (2005).
24. M. Hepel, and M. Tomkiewicz, *J. Electrochem. Soc.*, **131**, 1288 (1984).

25. G.T. Burstein, and R.C. Newman, *Electrochim. Acta.*, **25**, 1009 (1980).
26. J. Kunze, H.H. Strehblow, and G. Staikov, *Electrochem. Commun.*, **6**, 132 (2004).
27. L.C. Nagle, A.J. Ahern, L. Declan Burke, *J. Solid State Electrochem.*, **6**, 320 (2002).
28. N. Perez, *Electrochemistry and Corrosion Science*, Kluwer Academic Publishers, Norwell, MS, p.316 (2004).
29. X. Jin, J. Lu, P. Liu, and H. Tong, *J. Electroanal. Chem.*, **542**, 85 (2003).
30. M.F.L. de Mele, R.C. Salvarezza, V.D. Vasquez Moll, H.A. Videla, and A.J. Arica, *J. Electrochem. Soc.*, **133**, 746 (1986).
31. V.I. Birss, and C.K. Smith, *Electrochim. Acta*, **32**, 259 (1987).

Chapter 7

Comparison of the Interfacial Reaction Kinetics of Bromide and Iodide Anion with Silver Oxide on an Ag Substrate

7.1 Introduction

The three reaction pathways were introduced in and described in some detail in Chapter 1 section 1.2.1. Briefly, the conversion of Ag_2O on an Ag substrate to AgX by $\text{X}^-(\text{aq})$ (where $\text{X}^-(\text{aq})$ represents $\text{I}^-(\text{aq})$ or $\text{Br}^-(\text{aq})$) can occur via one of three of the following reaction pathways: (1) chemical reaction of X^- with Ag_2O in the oxide surface, (2) a galvanic coupling of Ag_2O reduction to Ag with the oxidation of Ag with $\text{X}^-(\text{aq})$ to AgX on the surface of the Ag substrate, or (3) dissolution of $\text{Ag}^+(\text{aq})$ from Ag_2O , followed by the reaction of $\text{Ag}^+(\text{aq})$ and $\text{X}^-(\text{aq})$ in the aqueous phase. In this study, the reaction of $\text{Br}^-(\text{aq})$ with Ag_2O on Ag are examined and the results are compared with the previously reported data on the reaction of $\text{I}^-(\text{aq})$ (Chapters 4 and 5). In this chapter we extend our study to include the interfacial reaction kinetics of the aqueous bromide anion with Ag_2O on a Ag substrate. The objective of this study is to explore how the different reaction thermodynamics and mass transport properties of the different halide ions affect interfacial reaction kinetics.

The interfacial reaction kinetics were followed by monitoring the open circuit potential (E_{OC}) after the reaction was initiated by exposing electrochemically-formed Ag_2O films to solutions containing $\text{Br}^-(\text{aq})$. The total reaction time, the time required to completely convert Ag_2O to AgBr , was easily determined since the E_{OC} dropped from the

equilibrium potential for the $\text{Ag}_2\text{O}/\text{Ag}$ redox pair to that of the AgBr/Ag redox pair. A similar change was observed in the conversion of Ag_2O to AgI , as discussed in Chapters 4 and 5. Galvanostatic reduction was performed to determine the amount of Ag_2O that remained and amount of AgBr formed as a function of reaction time. By measuring the total reaction time as a function of halide concentration, the anodic charge used to grow Ag_2O , and the electrode rotation rate, various reaction kinetic parameters were obtained. The kinetic analysis revealed that all three reaction pathways contributed significantly to the removal of the Ag_2O film for the bromide case. This is different from the behaviour observed for the conversion of Ag_2O to AgI . The $\Gamma(\text{aq})$ reaction occurs mainly via the chemical reaction pathway while the bromide system experiences a more complex kinetic analysis. The kinetic analysis results of the two halide systems are compared and the differences discussed.

7.2 *Experimental Details*

Electrochemical measurements were conducted in a three-electrode electrochemical cell where the working electrode was a silver disc (area of 0.385 cm^2), the counter electrode was platinum, and the reference electrode was a saturated calomel electrode (SCE). Measurements were conducted at room temperature in Ar-sparged $0.01 \text{ mol}\cdot\text{dm}^{-3}$ NaOH. Potassium bromide solutions were prepared with concentrations in the range of 5×10^{-4} to $3 \times 10^{-3} \text{ mol}\cdot\text{dm}^{-3}$.

Prior to electrochemical tests, the silver electrodes were abraded following the procedure described in Chapter 2, section 2.1.3. A cathodic cleaning at $-1.1 \text{ V}_{\text{SCE}}$ for 300 s removed any air-formed oxide from the Ag surface. The initial Ag_2O films were

grown potentiostatically at $0.4 V_{SCE}$. The total charge used to grow the starting Ag_2O film, $(Q_{Ag_2O})_0$, was measured and is related to the initial mass of Ag_2O in the film by equation 4.1. Films with different amounts of Ag_2O were prepared by varying $(Q_{Ag_2O})_0$ from 0.036 to 0.064 C.

The conversion of Ag_2O to $AgBr$ was initiated by transfer of the Ag_2O -coated electrode to an electrochemical cell with a solution containing $Br^-(aq)$. The reaction was then followed by monitoring the open circuit potential, E_{OC} . The effect of electrode rotation rate on the conversion kinetics was investigated over a range of 0 to 50 Hz.

The amounts of reactant Ag_2O and product $AgBr$ on the electrode as a function of time were determined by galvanostatic reduction, see schematic presented in Figure 7.1. In these experiments, the conversion reaction was terminated after a desired reaction time by transferring the electrode from a solution containing $Br^-(aq)$ to a solution containing only NaOH at the same pH. A constant negative current was then applied to the working electrode and the potential was monitored as a function of time. The negative current reduced the Ag_2O and/or $AgBr$ that was present on the Ag electrode surface. The reduction of Ag_2O and $AgBr$ was easily separated because Ag_2O will reduce at $0.22 V_{SCE}$ and $AgBr$ will reduce at $0.050 V_{SCE}$. The charge required to reduce Ag_2O and $AgBr$ can be obtained by multiplying the applied current ($-3.85 \times 10^{-5} A \cdot cm^2$) times the potential residence time at $0.22 V_{SCE}$ and $0.050 V_{SCE}$, respectively.

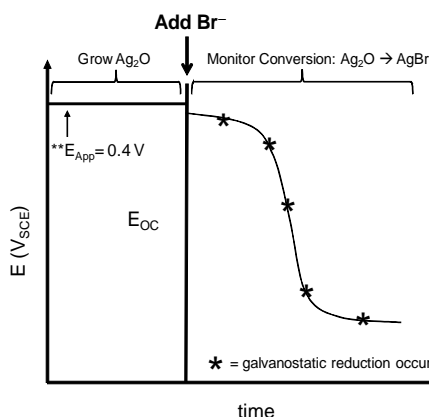


Figure 7.1 Schematic representation of the potential vs. time profile used for the kinetic analysis of Ag_2O on Ag with aqueous Br^- species.

If no dissolution of $\text{Ag}^+(\text{aq})$ has occurred during the reaction, then the charge used to grow the initial amount of Ag_2O , $(Q_{\text{Ag}_2\text{O}})_0$ should be equal to the sum of the charges used to reduce Ag_2O and AgBr present on the electrode at reaction time t , $(Q_{\text{Ag}_2\text{O}})_t$ and $(Q_{\text{AgBr}})_t$, respectively. Any difference between $(Q_{\text{Ag}_2\text{O}})_0$ and $(Q_{\text{Ag}_2\text{O}})_t + (Q_{\text{AgBr}})_t$ is attributed to the dissolution of $\text{Ag}^+(\text{aq})$ to the bulk aqueous phase, $(Q_{\text{Diss}})_t$:

$$(Q_{\text{Diss}})_t = (Q_{\text{Ag}_2\text{O}})_0 - ((Q_{\text{Ag}_2\text{O}})_t + (Q_{\text{AgBr}})_t) \quad (7.1)$$

The rate of dissolution of Ag_2O in a NaOH-only solution was also determined by galvanostatic reduction measurements. For these experiments Ag_2O was grown in a NaOH solution until the total charge reached 0.05 C (or $0.13 \text{ C}\cdot\text{cm}^{-2}$). After oxide film growth, the E_{OC} was monitored while the electrode was held in the cell for a desired dissolution time. After this period, the amount of Ag_2O that had dissolved was determined by measuring the charge required to remove the remaining Ag_2O .

The morphologies of Ag₂O and AgBr films were analyzed at various times during the conversion reaction. The electrodes were removed from the electrochemical cell, rinsed with deionized water, and dried with argon. Samples were stored under vacuum before being transferred to a Hitachi S-4500 field emission scanning electron microscope (SEM) equipped with a Quartz Xone energy dispersive X-ray (EDX) analysis system. This was used to examine the surface topography and analyze the elements present on the electrode surface.

7.3 Results

7.3.1 *E_{OC} Behaviour Observed During the Reaction of Ag₂O in Br⁻ Solutions*

A typical example of the time profile of E_{OC} is shown in Figure 7.2a. The E_{OC} shows three distinct stages of conversion. In stage 1, the initial E_{OC} starts close to the equilibrium potential for the Ag₂O/Ag redox pair, $(E^e)_{Ag_2O/Ag}$, and decreases slowly with time. In stage 2, the E_{OC} reaches and remains at a nearly constant value. In stage 3, the E_{OC} abruptly drops and quickly reaches a steady value close to the equilibrium potential for the AgBr/Ag redox pair, $(E^e)_{AgBr/Ag}$. The change in stage 3 indicates that the conversion from Ag₂O to AgBr was complete.

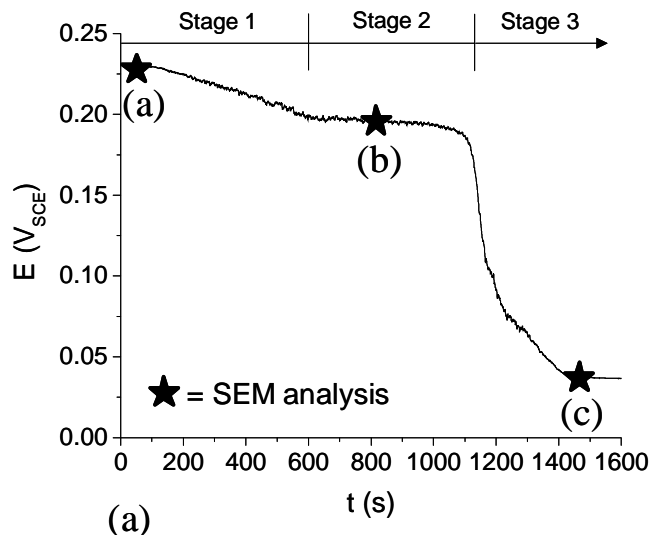


Figure 7.2 (a) A typical open circuit potential (E_{OC}) measurement observed of a Ag_2O film exposed to a solution containing $5 \times 10^{-4} \text{ mol}\cdot\text{dm}^{-3}$ of $Br^-(aq)$. The stars indicate the times at which a test coupon was removed for SEM analysis (see Figure 7.8).

7.3.2 Observed Dependence of Total Reaction Time on $[X^-(aq)]_0$ and $(Q_{Ag_2O})_o$

The abrupt drop in E_{OC} signals the completion of the Ag_2O to AgX conversion process and the time at which the drop occurs is the total reaction time, τ_f . The inverse of the reaction time gives the reaction rate. The E_{OC} profiles obtained with different $Br^-(aq)$ concentrations, but at a constant $(Q_{Ag_2O})_o$ are shown in Figure 7.3a, and the E_{OC} profiles obtained with various $(Q_{Ag_2O})_o$ and a constant $[Br^-(aq)]_0$, are shown in Figure 7.3b.

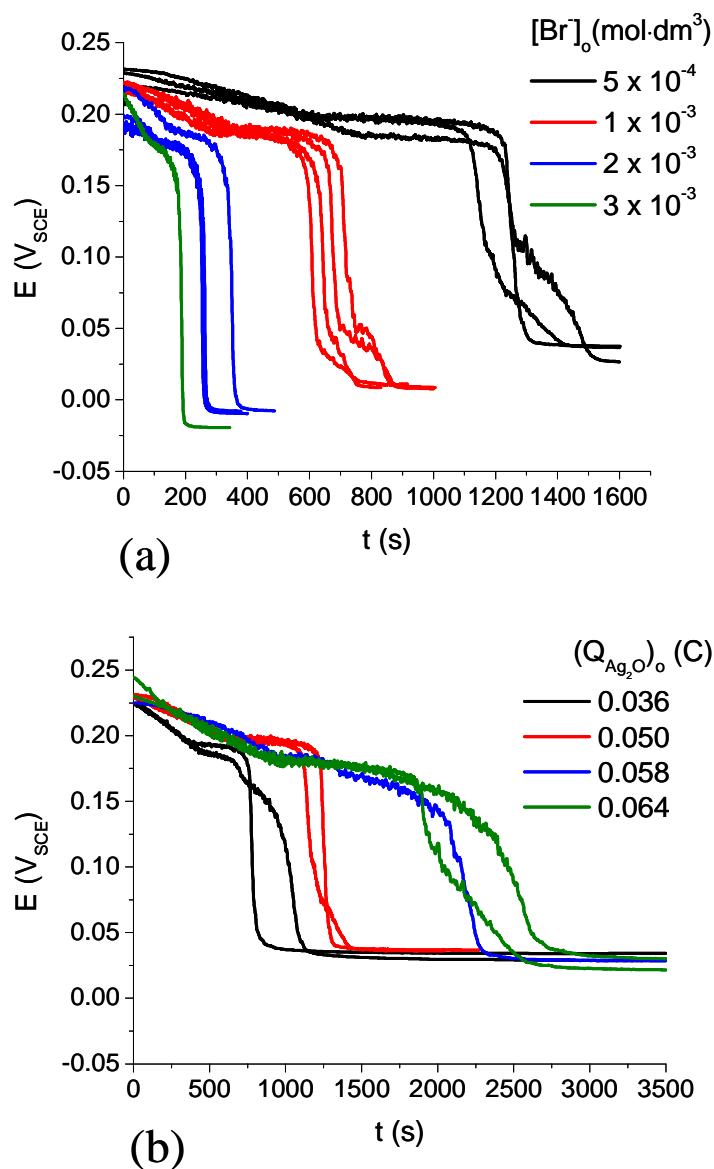
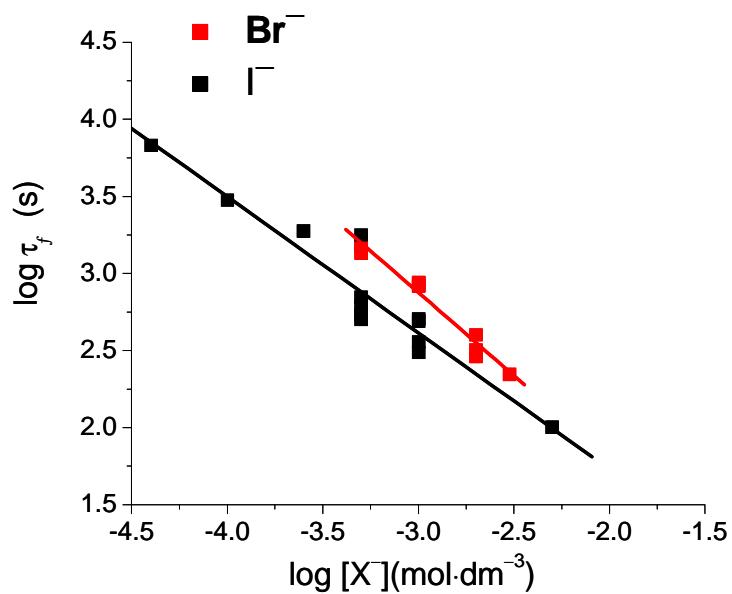


Figure 7.3 (a) A series of open circuit potential measurements performed at various Br^- (aq) concentrations where $(Q_{\text{Ag}_2\text{O}})_0$ is constant at 0.050 C. (b) Open circuit potential measurements carried out with different amounts of Ag_2O exposed to 5×10^{-4} mol·dm⁻³ Br^- (aq).

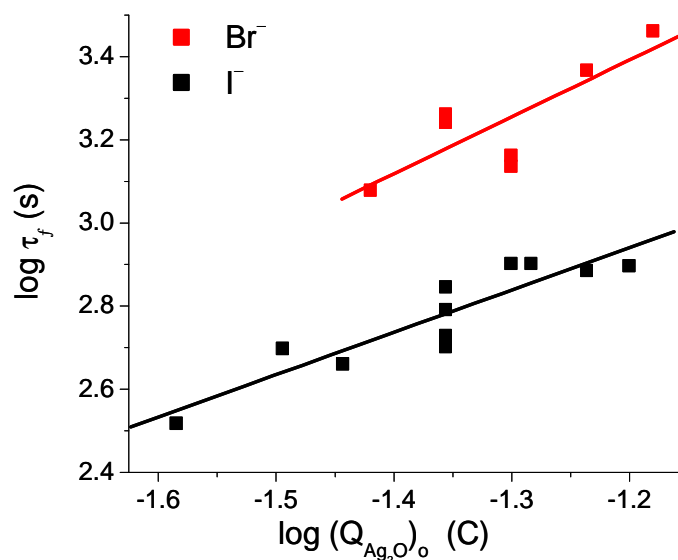
The τ_f observed as a function of $(Q_{\text{Ag}_2\text{O}})_0$ and $[\text{Br}^-](\text{aq})_0$ are shown in log-log plots in Figures 7.4a and 7.4b. Also shown in Figure 7.4 are the earlier reported data for the

reaction of Ag_2O with $\Gamma(\text{aq})$ for comparison. The slopes of the $\log \tau_f$ vs. $\log [\text{X}^-(\text{aq})]_0$ plots for both bromide and iodide reactions are $-1.0 (\pm 0.1)$, indicating that, over the studied concentration range, the surface reaction has a first order dependence on $[\text{X}^-(\text{aq})]_0$. On the other hand, the slopes for the $\log \tau_f$ vs. $(Q_{\text{Ag}_2\text{O}})_o$ plots of the two halides are slightly different. The slope is 1.4 ± 0.4 and 1.2 ± 0.1 for the bromide and iodide reactions, respectively. Although the uncertainties in the slope in the bromide case are larger than iodide, both results indicate that the reaction rate deviates from a first order dependence on $(Q_{\text{Ag}_2\text{O}})_o$. The reasons for the differences observed for the two halide systems are discussed in section 7.4.

The apparent rate constant $k_{\text{App}}^{\text{Br}}$ for the conversion of Ag_2O to AgBr was also calculated using the total reaction times from the E_{OC} measurements. Under stagnant conditions the $k_{\text{App}}^{\text{Br}}$ was $(1.61 \pm 0.33) \times 10^{-3} \text{ cm}\cdot\text{s}^{-1}$. This is approximately two times smaller than the $k_{\text{App}}^{\text{I}}$ determined for the conversion of Ag_2O to AgI , $(3.67 \pm 1.08) \times 10^{-3} \text{ cm}\cdot\text{s}^{-1}$ previously measured (Chapter 4).



(a)

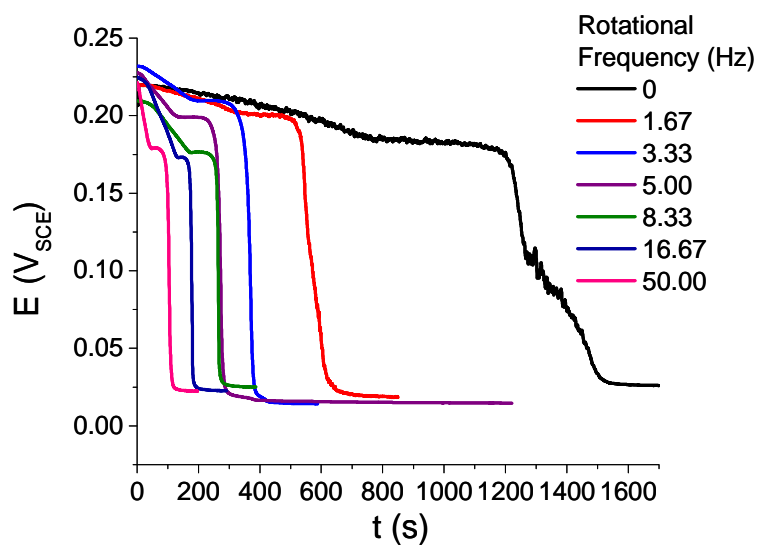


(b)

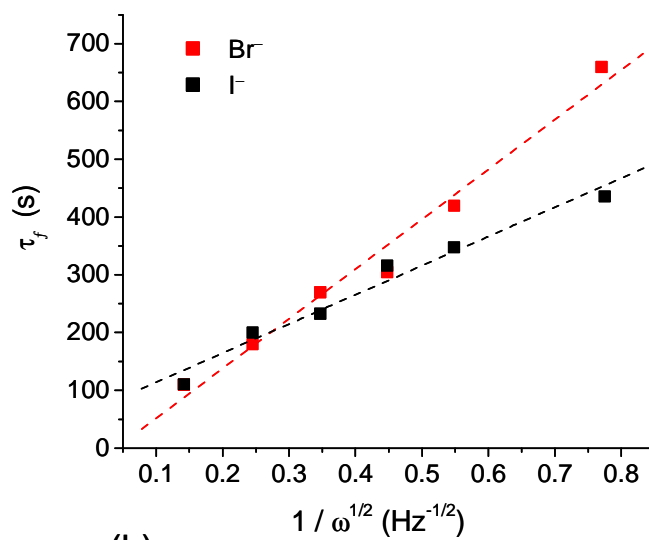
Figure 7.4 (a) Plot of the log of the total reaction time (τ_f) vs. $\log [X^-(aq)]_0$. (b) Plot of the log of the total reaction time (τ_f) vs. $\log (Q_{Ag_2O})_0$. Data for $I^-(aq)$ taken from Chapter 4.

7.3.3 *Observed Dependence of Total Reaction Time on Electrode Rotation Speed*

The open circuit potential profiles observed at different electrode rotation rates is shown in Figure 7.5a and the dependence of the total reaction time on $\omega^{-1/2}$ observed for the bromide reaction is shown in Figure 7.5b. Previously reported iodide data obtained under the same conditions are also shown in Figure 7.5b for comparison (Chapter 5). Both halides show a linear dependence on $\omega^{-1/2}$. The bromide shows a slightly steeper slope (733, compared to 504 for the iodide case) and a significantly lower intercept at infinite rotation.



(a)



(b)

Figure 7.5 (a) E_{OC} plotted as a function of reaction time for different electrode rotation speeds, ω , and (b) total reaction time vs. $(\omega^{-1/2})$. For this data $(Q_{Ag_2O})_0$ was 0.050 C and $[Br^-(aq)]_0$ was $5 \times 10^{-4} \text{ mol}\cdot\text{dm}^{-3}$. The results obtained in iodide solutions under the same experimental conditions are also included in (b) data taken from Chapter 5.

The surface reaction rate coefficients, k_{Surf}^X , obtained using the intercept extracted from Figure 7.5b and using equation (5.5) are $7.8 \times 10^{-1} \text{ cm}\cdot\text{s}^{-1}$ for bromide and $4.2 \times 10^{-2} \text{ cm}\cdot\text{s}^{-1}$ for iodide. These surface reaction rate coefficients are about one to two orders of magnitude larger than the net reaction rate coefficients k_{Net}^X measured under stagnant conditions.

7.3.4 Galvanostatic Reduction Measurements

Galvanostatic reduction measurements were performed to determine the amounts of reactant Ag_2O remaining, product AgBr formed, and Ag_2O lost due to dissolution as a function of reaction time. The potential as a function of time observed during the galvanostatic reduction is shown in Figure 7.6 for Ag_2O films exposed to a $\text{Br}^-(\text{aq})$ solution for different reaction times. The amounts of Ag_2O and AgBr present on the electrode were calculated using the method described in section 7.2 and these values are listed in Table 7.1. The sum of the Ag_2O and AgBr present on the electrode are plotted as a percentage of the initial Ag_2O film and are shown in Figure 7.7. Also shown in Figure 7.7 is the percentage of an Ag_2O film that does not dissolve after exposure of the film to a halide-free NaOH solution for different times.

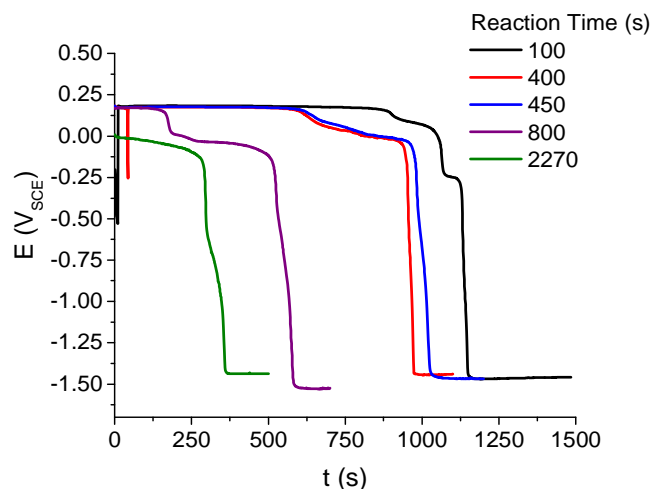


Figure 7.6 Potential as a function of time for galvanostatic reduction of Ag_2O and AgBr films. Prior to reduction, the Ag_2O films were grown to a constant anodic charge of 0.050 C and then exposed to solutions containing $[\text{Br}^-(\text{aq})]_0$ at $5 \times 10^{-4}\text{ mol}\cdot\text{dm}^{-3}$ for different reaction times.

Table 7.1 Measured quantities of Ag_2O and AgBr on an electrode and amount of $\text{Ag}^+(\text{aq})$ dissolved for different reaction times.

t_{rxn} (s)	$(Q_{\text{Ag}_2\text{O}})_t$ (C)	$(Q_{\text{AgBr}})_t$ (C)	$(Q_{\text{Diss}})_t$ (C)	% $\text{Ag}^+_{\text{Diss}}$
100	0.040	0.005	0.005	10
200	0.032	0.012	0.006	12
400	0.027	0.011	0.012	24
800	0.006	0.017	0.027	54
1480	0	0.014	0.036	72

Without $\text{Br}^-(\text{aq})$ present, the rate of loss of Ag_2O due to dissolution of Ag_2O in a halide-free solution at pH 12 was small. With $\text{Br}^-(\text{aq})$ present the rate of Ag_2O lost from the film was much faster. This is very different behaviour than what was observed for similar experiments in iodide solutions. The rate of Ag_2O loss from the Ag_2O film was small and comparable to the rate of loss due to Ag_2O dissolution alone [1–3]. The higher

rate of Ag_2O loss with Br^- (aq) present suggests the dissolution reaction pathway (reaction path 3) is an important contributor to the overall conversion of Ag_2O to AgBr .

The high rate of Ag loss from the Ag_2O film during the bromide reaction was somewhat surprising since the solubility of Ag_2O is very low at pH 12 (that was the reason for performing tests at this pH). Possible explanations for the Ag loss are discussed in section 7.4.

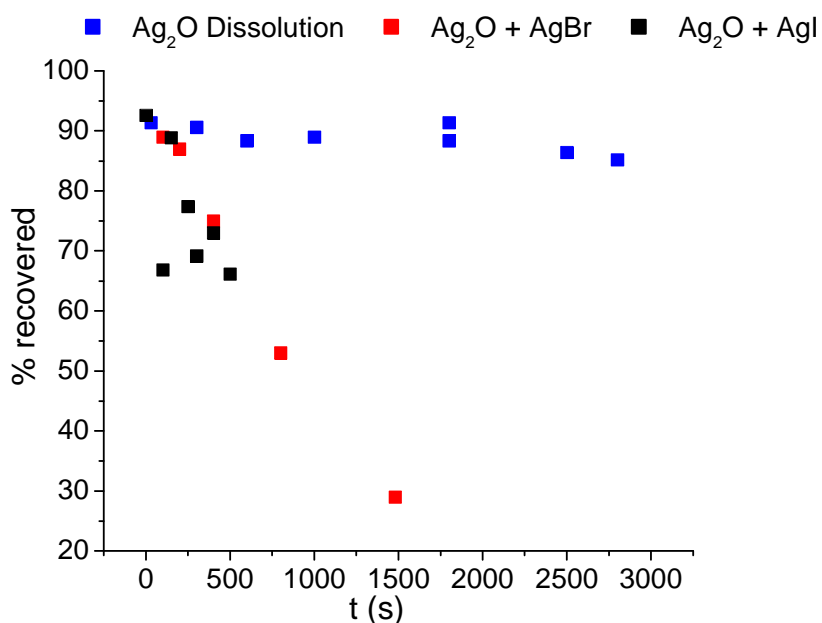


Figure 7.7 Fraction of Ag remaining on the Ag substrate as determined by the amounts of Ag_2O and AgBr present. Also shown is the fraction of the initial Ag_2O after exposure of a film to a $0.01 \text{ mol}\cdot\text{dm}^{-3}$ NaOH solution as a function of time and the amounts of Ag_2O and AgI calculated from the cathodic stripping results shown in Figure 4.5b.

7.3.5 *Surface Analysis*

The changes in surface morphology as the reaction progressed were examined by SEM and EDX. The SEM micrographs of the surface of the silver electrode taken at each of the three stages of conversion are shown in Figure 7.8 and the corresponding EDX spectra are shown in Figure 7.9. The times at which samples were removed from the cell for the SEM analysis are indicated on Figure 7.2a. The SEM micrographs show a decrease in the size of the Ag₂O crystals on the electrode as the reaction progressed. At the beginning of stage 1 the surface was covered by a compact film of relatively uniform ‘spherical’ Ag₂O crystals ranging in size from 180–200 nm in diameter. The EDX spectrum for these crystals contains two prominent peaks attributed to Ag and O and no other measurable peaks. By the beginning of stage 2, the Ag₂O crystals are smaller and additional irregularly-shaped, longer crystals can be seen inter-dispersed on the surface (circled in Figure 7.8b). The EDX spectrum of the irregularly-shaped crystals shows strong Ag and Br peaks and a negligible O peak. The electrode in stage 3 is quite different. Large areas of the electrode surface appeared to be covered by few or no crystals. The remaining crystals are found in unevenly distributed larger clusters on the Ag substrate. This change is reflected in the EDX spectrum which shows a strong Ag peak and a very weak Br peak (Figure 7.9c).

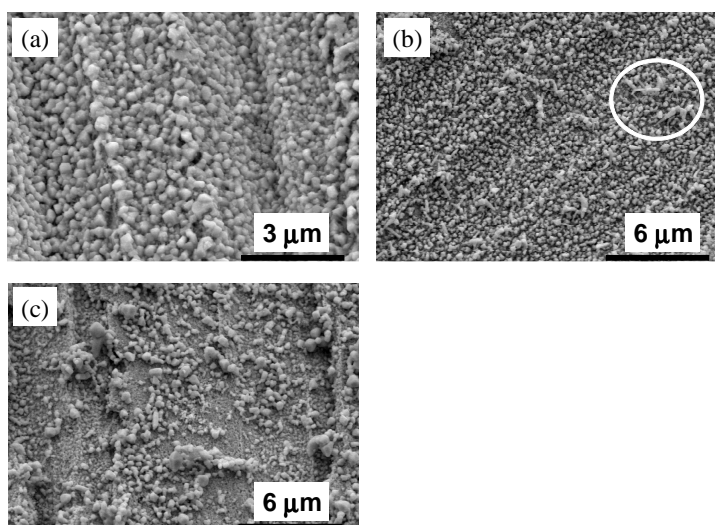


Figure 7.8 SEM images of the Ag electrode surface obtained after different reaction times (see Figure 7.2a).

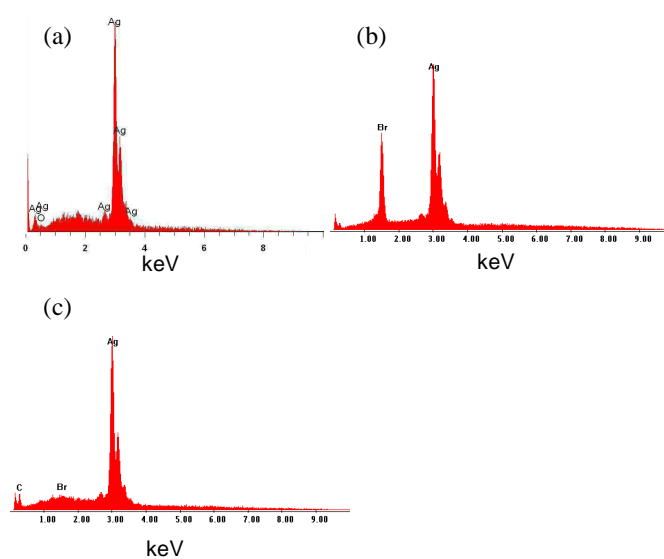


Figure 7.9 EDX analysis carried out on the Ag electrode surface corresponding to the SEM images shown in Figure 7.8 and reaction times shown in Figure 7.2a.

7.4 Discussion

As stated in section 7.1, there are three reaction pathways for the conversion of Ag_2O to AgX on conducting a Ag substrate. The differences observed for the reactions of Br^- (aq) and I^- (aq) with Ag_2O indicate that different kinetic paths are involved for the different halides.

7.4.1 Chemical Reaction Path (1)

The rates of reaction pathway (1), surface chemical reaction, and reaction pathway (2), galvanic coupling, can be controlled by the diffusion of the reacting halide from the bulk solution to the reacting film. Experiments performed at various electrode rotation rates showed that ion mass transport in the aqueous phase does influence the reaction rate. By extrapolating to infinite rotation, we have obtained the surface reaction rate coefficient, k_{Surf}^X . Since the surface reaction of halide with Ag_2O on Ag can occur via both reaction paths (1) and (2), k_{Surf}^X consists of two components:

$$k_{\text{Surf}}^X \approx k_{\text{Surf-Chem}}^X + k_{\text{Surf-Galv}}^X \quad (7.2)$$

We found the k_{Surf}^X value was $4.2 \times 10^{-2} \text{ cm}\cdot\text{s}^{-1}$ for iodide and $7.8 \times 10^{-1} \text{ cm}\cdot\text{s}^{-1}$ for bromide.

The results reported earlier, and additional research performed in our laboratory suggests that the reaction of I^- (aq) with Ag_2O on Ag occurs mainly via the chemical reaction pathway (reaction path 1) [1–3] (i.e., $k_{\text{Surf-Chem}}^{\text{I}} \gg k_{\text{Surf-Galv}}^{\text{I}}$). For Br^- (aq) the rate of the similar chemical reaction could be slower than the rate for I^- (aq) because the Gibbs free energy of reaction, $\Delta_r G$, is smaller for the bromide reaction than for the iodide

reaction. From the thermodynamic properties of the reactants and products (given in Table 7.2), the $\Delta_r G$ values for the reactions of Ag_2O and $\text{X}^-(\text{aq})$ forming AgI and AgBr are $-255.7 \text{ kJ}\cdot\text{mol}^{-1}$ and $-213.3 \text{ kJ}\cdot\text{mol}^{-1}$, respectively [4].

Table 7.2 Thermodynamic parameters for species involved in the $\text{Ag}_2\text{O}/\text{AgX}$ reactions.

Thermo. Parameter	$\text{Ag}_2\text{O}(\text{s})$	$\Gamma(\text{aq})$	$\text{Br}^-(\text{aq})$	$\text{AgI}(\text{s})$	$\text{AgBr}(\text{s})$	$\text{H}_2\text{O}(\text{aq})$	$\text{OH}^-(\text{aq})$	$\text{Ag}^+(\text{aq})$
ΔH_f° ($\text{kJ}\cdot\text{mol}^{-1}$)	-31.1	-56.7	-121.4	-61.8	-100.4	-285.8	-230.0	105.6
S° ($\text{J}\cdot\text{mol}^{-1}$)	121.3	106.4	82.5	115.5	107.1	69.9	-10.8	72.7

The activation energy for a reaction, which tends to control the reaction rate, is not dependent on the Gibbs free energy of reaction, but for a reversible system, with a low activation energy, a more highly favoured reaction will tend to make the approach to equilibrium faster and yield a higher chemical reaction rate. Clearly this is an important consideration here because the surface reaction rate for bromide is faster than that for iodide. Additionally, we have no reason to expect that the activation energy for the surface chemical reaction between Ag_2O and $\text{X}^-(\text{aq})$ will be higher for $\Gamma(\text{aq})$ compared to $\text{Br}^-(\text{aq})$ to explain the higher reaction rate. For example, the electron affinity of Br^- is greater than that of Γ^- ($-324 \text{ kJ}\cdot\text{mol}^{-1}$ for Br^- and $-295 \text{ kJ}\cdot\text{mol}^{-1}$ for Γ^- [5]) and the chemical reaction (reaction pathway 1) might not be expected to proceed faster with the halide that can most easily give up its electron (Γ^-).

If the higher k_{Surf}^X value observed for the bromide reaction is not due to a higher chemical reaction rate, then pathway 2 must be making a large contribution to the overall reaction of $Br^-(aq)$ with Ag_2O .

7.4.2 Galvanic Coupling Reaction Path (2)

The galvanic coupling reaction can begin when the halide ion diffuses through the Ag_2O film to the Ag substrate. In the iodide system, where the chemical reaction path dominates the interaction, the concentration of iodide reaching the Ag substrate is negligible until most of the Ag_2O film is converted to AgI. The bromide ion has a smaller ionic radius than the iodide ion (1.96 Å for Br^- and 2.2 Å for I^- [6]) and this will make diffusion through the Ag_2O lattice easier and faster for Br^- . This will allow the galvanic coupling reaction to start to make a contribution to the overall reaction rate at an earlier time and lead to an overall faster rate in the bromide reaction.

The presence of a significant rate of the galvanic coupling reaction in the bromide system can be seen from the E_{OC} behaviour. The E_{OC} is determined by the potential at which the anodic and cathodic reaction rates must be equal, and a change in the E_{OC} indicates a change in the redox rates. In the bromide system, the E_{OC} starts to decrease immediately (Figure 7.2b) until it reaches a pseudo steady-state value in stage 2. In $I^-(aq)$ solutions, the E_{OC} remained at a constant value close to the equilibrium potential of the Ag_2O/Ag pair, $(E^e)_{Ag_2O/Ag}$ for most of stage 1, indicating that the concentration of $I^-(aq)$ reaching the Ag substrate was negligible during stage 1.

The transition from stage 1 to stage 2 also occurred at an earlier time in the Br^- (aq) solution, compared to that observed in the Γ (aq) solution. Although E_{OC} remained relatively constant during stage 2 in both halide solutions, its value was lower during the reaction with Br^- (aq), despite the more positive $(E^e)_{\text{AgBr}/\text{Ag}}$.

The time-dependent behaviour of E_{OC} as a function of electrode rotation rates shows that rotation not only shortens the durations of stages 1 and 2 (and hence τ_f), but also increases the rate of change in E_{OC} in stage 1. Faster rotation will increase the Br^- (aq) concentration at the film surface and hence the concentration of Br^- (aq) through the Ag_2O film. This would support a faster galvanic coupling reaction rate.

When the chemical reaction is slow, the concentration of X^- (aq) at the oxide/solution interface is close to its concentration in the bulk aqueous phase. Under these conditions,

$$[\text{X}^-(m)]_t \propto \frac{[\text{X}^-(aq)]_0}{\sqrt{(d_{\text{Ag}_2\text{O}})_t}} \quad (7.3)$$

where $[\text{X}^-(m)]_t$ is defined as the concentration of X^- (aq) at the Ag substrate, and

$(d_{\text{Ag}_2\text{O}})_t$ is the thickness of the Ag_2O film [7]. Additionally, the initial oxide thickness

$(d_{\text{Ag}_2\text{O}})_0$ is related to the charge used to grow the initial Ag_2O film by equation 4.1.

Thus, if the electrochemical reaction is the dominant reaction path, the total reaction time will have a 1.5-order dependence on $(Q_{\text{Ag}_2\text{O}})_0$:

$$\tau_f \propto \frac{(Q_{\text{Ag}_2\text{O}})_0 \cdot \sqrt{(Q_{\text{Ag}_2\text{O}})_0}}{[\text{X}^-(aq)]_0} \quad (7.4)$$

The dependence of τ_f on $(Q_{Ag_2O})_0$ observed in the bromide reaction was 1.4, closer to 1.5, while that observed for I^- was 1.2, closer to 1.0. These observations are consistent with a greater contribution from the galvanic coupling reaction pathway to the overall reaction for the bromide case.

7.4.3 Ag^+ Dissolution Path (3)

In the bromide case, we have observed much greater loss of Ag_2O from the electrode compared to the loss seen in NaOH or iodide solutions. This was somewhat surprising since the reaction conditions (pH, temperature) were identical. We attribute the increase in silver dissolution in $Br^-(aq)$ solutions to the reaction of $Ag^+(aq)$ and $Br^-(aq)$ to form $AgBr(aq)$. This will result in a steeper $Ag^+(aq)$ concentration gradient in the oxide/solution interfacial region, thus increasing the $Ag^+(aq)$ dissolution rate. The solubility products of Ag_2O , $AgBr$ and AgI are $K_{sp}^{Ag_2O} = 3.6 \times 10^{-11}$, $K_{sp}^{AgBr} = 5.3 \times 10^{-13}$ and $K_{sp}^{AgI} = 8.3 \times 10^{-17}$, respectively [4]. Reaction of $Ag^+(aq)$ from Ag_2O to form a lower solubility product silver halide will decrease the $Ag^+(aq)$ concentration in the aqueous phase via precipitation of AgX . Because the AgI solubility is extremely low, any AgI formed will tend to precipitate immediately on the adjacent Ag_2O film. More soluble $AgBr$ can diffuse away from film in the aqueous phase. We did not observe any silver bromide colloidal particles in the aqueous phase because there was not enough present in the large volume of the electrolyte solutions used in the experiments.

The effect of $AgBr$ loss to the solution on the bromide reaction kinetics can be seen in the dependence of the total reaction time on the electrode rotation rate. While

both halide reactions have a τ_f with a linear dependence on $\omega^{-1/2}$, the bromide case shows a steeper slope of 733, compared to a slope of 504 for the iodide case. Since the diffusion coefficients of $\text{Br}^-(\text{aq})$ and $\text{I}^-(\text{aq})$ in the aqueous phase are nearly the same [4], mass transport of another species in the interface region must be causing the different dependences. We attribute the difference to diffusion of AgBr from the interface region.

7.5 Conclusions

The conversion of Ag_2O on Ag to AgBr by $\text{Br}^-(\text{aq})$ anion has been studied and the results have been interpreted in terms of three different reaction pathways. The results have also been compared with the previously reported results for the conversion of Ag_2O to AgI by $\text{I}^-(\text{aq})$. Under stagnant conditions, the bromide reaction was found to be slower than the iodide reaction. However, experiments performed as a function of electrode rotation rate determined that the reaction with bromide was faster compared to iodide. The reaction of Ag_2O with $\text{I}^-(\text{aq})$ to AgI occurred mainly by a chemical reaction path and alternative galvanic coupling and dissolution pathways did not contribute significantly to the overall reaction of Ag_2O . Very different kinetic behaviour was observed for the reaction with bromide. The smaller Br^- anion size permitted faster diffusion of Br^- through the Ag_2O film to the Ag substrate. The presence of Br^- at the Ag/oxide substrate enabled the galvanic coupling reaction to occur faster and compete with the chemical reaction pathway. Also, dissolution of Ag_2O which released $\text{Ag}^+(\text{aq})$ near the $\text{Ag}_2\text{O}/\text{solution}$ interface led to the formation of $\text{AgBr}(\text{aq})$ which is more soluble than the similarly formed AgI . The higher AgBr solubility allows it to diffuse into the bulk

solution, as opposed to immediate precipitation on the $\text{Ag}_2\text{O}/\text{AgBr}$ film and thereby cause a high loss of Ag. Both the electrochemical results and SEM micrographs of the $\text{Ag}/\text{Ag}_2\text{O}$ surface confirmed that formation of AgBr via the dissolution pathway is more prevalent in the $\text{Br}^-(\text{aq})$ system compared to the $\text{I}^-(\text{aq})$ system.

Overall, the results of this study show that the $\text{Ag}/\text{Ag}_2\text{O}$ films are particularly stable with respect to reaction with $\text{I}^-(\text{aq})$ compared to other halides. This means that $\text{Ag}/\text{Ag}_2\text{O}$ films can be used in applications where reactive trapping of iodine (and particularly trace levels of radioactive iodine) are required. The work also shows that contamination of the system by $\text{Br}^-(\text{aq})$, and likely Cl^- , is undesirable because it could lead to higher loss rates of an $\text{Ag}/\text{Ag}_2\text{O}$ film.

7.6 References

1. X. Zhang, S.D. Stewart, D.W. Shoesmith, and J.C. Wren, *J. Electrochem. Soc.*, **154**, F70 (2007).
2. X. Zhang, D.W. Shoesmith, and J.C. Wren, *Corr. Sci.*, **50**, 490 (2008).
3. S. Pretty, P.G. Keech, X. Zhang, J.J. Noël, and J.C. Wren, *Electrochim. Acta*, **56**, 2754 (2011).
4. *CRC Handbook of Chemistry and Physics*, 92nd ed.; CRC Press: Boca Raton, FL., 2011.
5. R.S. Berry, C.W. Reinmann, and G.N. Spokes, *J. Chem. Phys.*, **37**, 2278 (1962).
6. R.D. Shannon, *Acta Cryst.*, **A32**, 751 (1976).
7. A.J. Bard, L.R. Faulkner, *Electrochemical Methods: Fundamentals and Applications*, 2nd ed., John Wiley & Sons Inc., Hoboken, NJ, 2001.

Chapter 8

Investigating the Galvanic Coupling Reaction Pathway During the Conversion of Ag_2O to AgX

8.1 Introduction

The reaction of $\text{X}^-(\text{aq})$ with Ag_2O (where $\text{X}^-(\text{aq})$ is $\text{I}^-(\text{aq})$ or $\text{Br}^-(\text{aq})$) on an Ag substrate to form AgX occurs via one or more of three pathways: (1) chemical reaction where $\text{X}^-(\text{aq})$ reacts with Ag_2O on the oxide surface, (2) a galvanic coupling of Ag_2O reduction to Ag coupled with the oxidation of Ag with $\text{X}^-(\text{aq})$ forming AgX on the surface of the Ag substrate, or (3) dissolution of $\text{Ag}^+(\text{aq})$ from Ag_2O , followed by the reaction of $\text{Ag}^+(\text{aq})$ and $\text{X}^-(\text{aq})$ in the aqueous phase. In Chapter 7 we explored the reaction kinetics for the bromide system, and compared it with the kinetics of the iodide system discussed in Chapters 4 and 5. These investigations led us to conclude that the chemical reaction path (1) is the dominant path for the reaction of $\text{I}^-(\text{aq})$ with Ag_2O , but contributes less for the reaction with $\text{Br}^-(\text{aq})$. The slow chemical reaction results in an increase in the concentration of $\text{Br}^-(\text{aq})$ to the Ag substrate as well as to the Ag_2O surface, thus, promoting the galvanic coupling reaction (pathway 2) and the dissolution reaction (pathway 3). In this chapter, the role of the galvanic coupling reaction in the net conversion of Ag_2O to AgX was investigated by performing potentiostatic polarization and linear polarization measurements at different reaction times.

8.2 *Experimental Details*

Silver working electrodes with a surface area of 0.385 cm^2 were polished following procedure described previously (Chapter 2, section 2.1.3). The three-electrode electrochemical set-up included a silver working electrode, a platinum mesh counter electrode and a saturated calomel (SCE) reference electrode. All potentials are quoted against the SCE scale ($0.241 \text{ V vs. the SHE}$). Experiments were conducted at room temperature in $0.01 \text{ mol}\cdot\text{dm}^{-3}$ NaOH electrolyte solutions. Prior to electrochemical tests, electrolyte solutions were Ar-sparged for 1 h, and purging was maintained for the duration of the measurement. Potassium bromide and potassium iodide solutions were added to the electrochemical cell after Ag_2O film growth.

8.2.1 *Reaction of Ag_2O with $X^-(aq)$*

After a cathodic cleaning at $-1.1 \text{ V}_{\text{SCE}}$, a Ag_2O film was grown potentiostatically by applying a potential of $0.4 \text{ V}_{\text{SCE}}$ until the total oxidation charge, $(Q_{\text{Ag}_2\text{O}})_0$, reached 0.050 C . The Ag_2O -covered electrode was then transferred to a solution containing $1 \times 10^{-4} \text{ mol}\cdot\text{dm}^{-3}$ KI or KBr, and the E_{OC} was monitored. At this halide concentration, $(E^e)_{\text{AgI}/\text{Ag}}$ and $(E^e)_{\text{AgBr}/\text{Ag}}$ were $-0.16 \text{ V}_{\text{SCE}}$ and $0.067 \text{ V}_{\text{SCE}}$, respectively.

8.2.2 *Potentiostatic Control Measurements*

To explore the reaction mechanism further, potentiostatic control experiments were conducted at different times during the E_{OC} drop. In the first set of experiments, a potential of $0.22 \text{ V}_{\text{SCE}}$, the equilibrium potential for the $\text{Ag}_2\text{O}/\text{Ag}$ redox pair at pH 12, was applied immediately after immersing a Ag_2O -covered electrode in a solution

containing $5 \times 10^{-4} \text{ mol}\cdot\text{dm}^{-3} \text{X}^{-}(\text{aq})$. This fixed potential was applied for the length of time required for the E_{OC} to drop from the equilibrium potential for the $\text{Ag}_2\text{O}/\text{Ag}$ redox pair to the equilibrium potential for the AgX/Ag redox pair. The length of time that the fixed potential was applied for was determined by kinetic experiments described above and in Chapters 4–7. Note that this time varied depending on halide type and concentration (see Figure 8.1). The E_{OC} was monitored after potentiostatic control, until it decreased to the equilibrium potential of the AgX/Ag redox pair; $0.050 \text{ V}_{\text{SCE}}$ for reactions in $\text{Br}^{-}(\text{aq})$, or $-0.20 \text{ V}_{\text{SCE}}$ for reactions in $\text{I}^{-}(\text{aq})$.

In the second experiment, a Ag_2O -covered electrode was exposed to a solution containing $5 \times 10^{-4} \text{ mol}\cdot\text{dm}^{-3} \text{X}^{-}(\text{aq})$ and the reaction was allowed to proceed at E_{OC} for a desired reaction time (until the end of stage 1). A fixed potential, equal to the E_{OC} at the end of stage 1 ($0.20 \text{ V}_{\text{SCE}}$), was applied for the time required for complete conversion of Ag_2O to AgX to occur. The E_{OC} was then monitored until it decreased to the equilibrium potential mentioned above.

Silver bromide and silver iodide films were grown potentiostatically on Ag_2O -free Ag electrodes. The AgBr films were grown at $0.20 \text{ V}_{\text{SCE}}$ ($\eta = 0.15 \text{ V}$) and AgI films at $0.0 \text{ V}_{\text{SCE}}$ ($\eta = 0.20 \text{ V}$), in both cases the halide concentration was $5 \times 10^{-4} \text{ mol}\cdot\text{dm}^{-3} \text{X}^{-}(\text{aq})$.

8.2.3 Linear Polarization Resistance Measurements

Linear polarization resistance measurements were acquired approximately every 30 min after exposure of Ag_2O -covered Ag electrodes to solutions containing

$1 \times 10^{-4} \text{ mol}\cdot\text{dm}^{-3}$ KI or KBr. The LPR measurement consisted of a potential scan $\pm 15 \text{ mV}$ vs. the E_{OC} at a scan rate of $0.17 \text{ mV}\cdot\text{s}^{-1}$.

8.3 Results and Discussion

8.3.1 Open Circuit Behaviour Observed During the Conversion of Ag_2O to AgX

A typical example of the time profile of E_{OC} observed during the reaction of Ag_2O with $\Gamma(\text{aq})$ or $\text{Br}^-(\text{aq})$ is shown in Figure 8.1. In both halide solutions the Ag_2O film undergoes three distinct stages of conversion, as indicated by the E_{OC} behaviour in Figure 8.1, which have been discussed in detail in Chapters 4, 5 and 7. Briefly, in stage 1, the initial E_{OC} was close to the equilibrium potential for the $\text{Ag}_2\text{O}/\text{Ag}$ redox pair, $(E^e)_{\text{Ag}_2\text{O}/\text{Ag}}$, but continually decreased with time. This was followed by stage 2, where E_{OC} remained nearly constant, until it dropped abruptly to a value closer to the equilibrium potential for the AgX/Ag redox pair, $(E^e)_{\text{AgX}/\text{Ag}}$, which indicated that the conversion from Ag_2O to AgX was complete. Once the E_{OC} reached $(E^e)_{\text{AgX}/\text{Ag}}$, in the final stage (stage 3), E_{OC} did not change any further.

As discussed in detail in Chapter 7, the net reaction of Ag_2O with $\text{Br}^-(\text{aq})$ under stagnant conditions was slower than the reaction with $\Gamma(\text{aq})$. This is reflected in the total reaction times (τ_f) observed in Figure 8.1. For the same halide concentration and initial amount of Ag_2O , $(Q_{\text{Ag}_2\text{O}})_0$, the τ_f for the reaction of Ag_2O with $\text{Br}^-(\text{aq})$ was 6300 s and with $\Gamma(\text{aq})$ was 2700 s. Replacement of $\Gamma(\text{aq})$ with $\text{Br}^-(\text{aq})$ lengthened the duration of stages 1 and 2, and hence a longer total reaction time was observed.

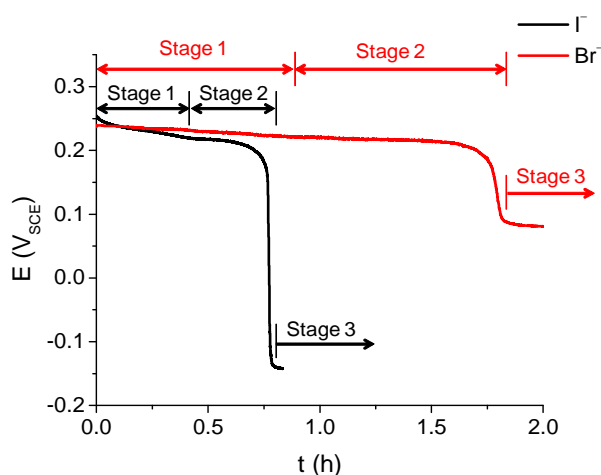


Figure 8.1 Open circuit potential as a function of reaction time and its dependence on halide type. For these experiments, $(Q_{Ag_2O})_0$ was constant at 0.050 C and the halide concentration was $1 \times 10^{-4} \text{ mol}\cdot\text{dm}^{-3}$.

8.3.2 Reaction of Ag_2O with $Br^-(aq)$

8.3.2.1 Potentiostatic Polarization at $(E^e)_{Ag_2O/Ag}$

Polarization at 0.22 V_{SCE} of an Ag_2O -covered Ag electrode in bromide solutions resulted in a current that increased steadily, which eventually reached a maximum magnitude of $0.08 \text{ mA}\cdot\text{cm}^{-2}$, Figure 8.2a. This current was attributed mainly to the anodic oxidation of Ag to AgBr at the Ag substrate. In addition, the maximum current was almost equal in magnitude to the steady-state current observed during the anodic growth of a AgBr film on a bare Ag electrode, which is also shown in Figure 8.2a for comparison. The steady-state current in the latter case has been observed to be independent of potential in the range from $(E^e)_{AgX/Ag}$ to $(E^e)_{Ag_2O/Ag}$ but dependent on the $X^-(aq)$ concentration [1]. The magnitude of the steady-state current was limited by the aqueous diffusion of halide ion to the electrode surface [2–4]. The slow and steady

increase in current during polarization at 0.22 V_{SCE} observed for the Ag₂O-covered Ag electrode (Figure 8.2a) was attributed to an increase in Br⁻(aq) concentration at the Ag substrate with time, as Br⁻(aq) diffused through the Ag₂O film. Once the concentration of Br⁻(aq) at the Ag substrate equalled that of the bulk aqueous concentration of Br⁻(aq) the anodic current reached the same magnitude as the diffusion-limited current observed during AgBr growth on a bare Ag electrode.

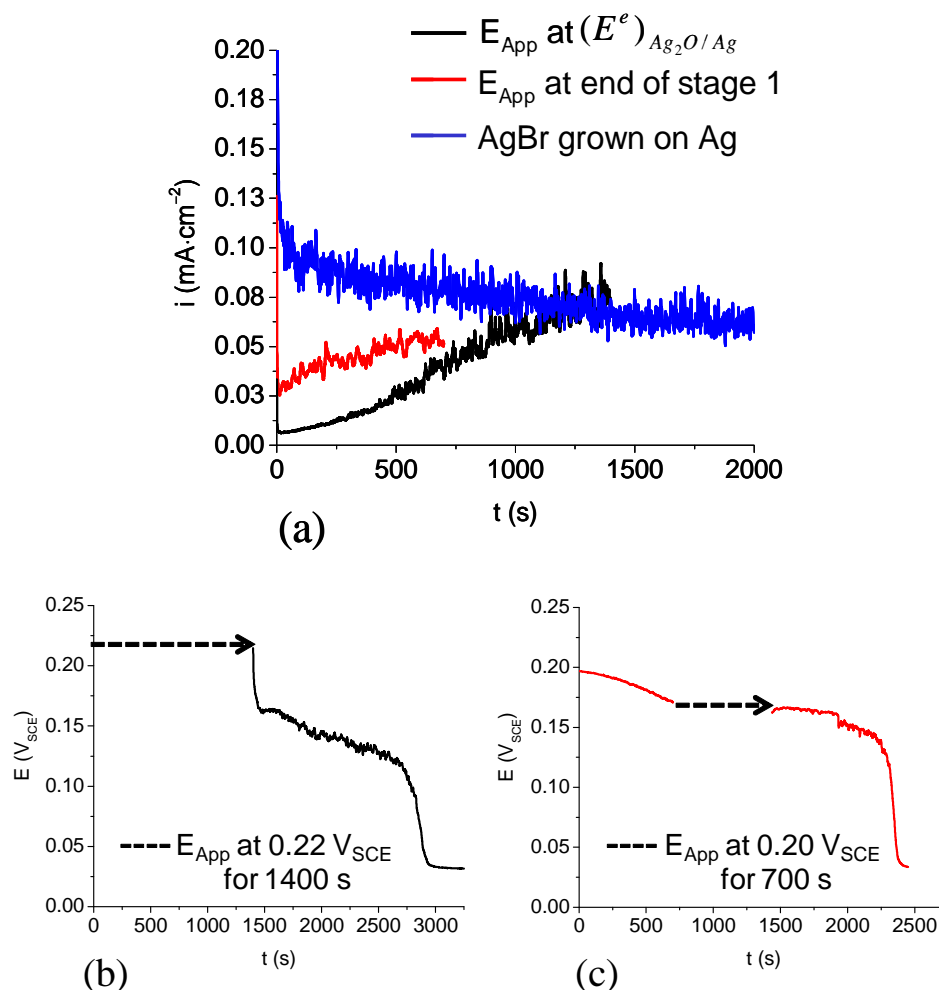


Figure 8.2 (a) Currents observed during the potentiostatic periods of the partial control experiments as described in section 8.3.2.1 and 8.3.2.2. The current observed during anodization at 0.20 V_{SCE} of an oxide-free Ag electrode in 5×10^{-4} mol·dm⁻³ Br⁻(aq) solution is also shown for comparison. Potential profiles recorded during partially controlled potentiostatic experiments; (b) 0.22 V_{SCE} was applied for 1400 s immediately after transfer of the Ag₂O/Ag electrode to the bromide solution, followed by E_{OC} measurement; (c) E_{OC} was measured until the end of stage 1, followed by potentiostatic control at E_{OC} (0.20 V_{SCE}) for 700 s, followed by further measurement at E_{OC} .

The E_{OC} measured following polarization at 0.22 V_{SCE} for 1400 s shows a gradual decrease from 0.15 to 0.10 V_{SCE}, which was slightly more negative (50-100 mV) than the E_{OC} typically observed during the reaction of Br⁻(aq) with Ag₂O/Ag (Chapter 7). Since

the anodic and cathodic reaction rates are the same at E_{OC} and the rates of these half reactions are a function of overpotential (i.e., the potential difference between E_{OC} and $(E^e)_{Ag_2O/Ag}$ or $(E^e)_{AgBr/Ag}$), the change in E_{OC} reflects the change in the galvanic coupling reaction. The different E_{OC} behaviour observed with and without polarization can then be attributed to the different $Br^-(aq)$ concentrations present at the Ag substrate.

It took 1500 s for the E_{OC} to drop to the expected value of 0.050 V_{SCE}, i.e., $(E^e)_{AgBr/Ag}$, Figure 8.2b. This time was similar to the total reaction time observed for the reaction of $Br^-(aq)$ with Ag_2O/Ag on open circuit. These results indicate that during polarization at 0.22 V_{SCE} very little, if any, Ag_2O had reacted with $Br^-(aq)$. At the applied potential near $(E^e)_{Ag_2O/Ag}$, the anodic reaction of Ag with $Br^-(aq)$ to form AgBr was relatively fast, since the overpotential, $\eta = E_{App} - (E^e)_{AgBr/Ag} = 0.17$ V_{SCE}, was relatively large. Thus, most of the $Br^-(aq)$ at or near the electrode surface was consumed by the anodic formation of AgBr, leading to suppression of the chemical reaction (reaction pathway 1). At $(E^e)_{Ag_2O/Ag}$, the cathodic reduction of Ag_2O was negligible which prevented galvanic coupling (reaction pathway 2). The reaction via the dissolution process (reaction pathway 3) may occur, but since the applied potential was 0.22 V_{SCE}, a value close to $(E^e)_{Ag_2O/Ag}$, Ag_2O would be continuously replenished by the oxidation of Ag to Ag_2O . Consequently, the net conversion of Ag_2O to AgBr was suppressed during polarization at $(E^e)_{Ag_2O/Ag}$.

8.3.2.2 Potentiostatic Polarization at the End of Stage 1

The current measured during polarization at the end of stage 1, after 700 s of exposure of the electrode to $\text{Br}^-(\text{aq})$ solution, was initially $0.03 \text{ mA}\cdot\text{cm}^{-2}$ and continued to increase, approaching the steady-state current observed for the anodic oxidation of Ag to AgBr on a bare Ag electrode. This result is consistent with the expectation that the Ag substrate was already exposed to $\text{Br}^-(\text{aq})$ at a considerable concentration when the potential was applied, since sufficient time was allowed for the diffusion of $\text{Br}^-(\text{aq})$.

The E_{OC} behaviour after polarization at the end of stage 1 is shown in Figure 8.2c. The results show that the potential transition occurred ~ 1000 s after the fixed potential was applied. The total time required to complete the reaction of Ag_2O with $\text{Br}^-(\text{aq})$ on open circuit was 1700 s (700 s before polarization plus 1000 s after). As observed in the first set of experiments, this total reaction time was similar to the τ_f measured for the reaction on open circuit without polarization. Therefore, like during the polarization at $0.22 \text{ V}_{\text{SCE}}$, the net conversion of Ag_2O to AgBr appears to be nearly suppressed during the polarization at $0.20 \text{ V}_{\text{SCE}}$, which was still sufficiently higher than $(E^e)_{\text{AgBr}/\text{Ag}}$. At the applied potential of $0.20 \text{ V}_{\text{SCE}}$, the cathodic reduction of Ag_2O to Ag was also possible, but did not appear to be significant.

8.3.2.3 Linear Polarization Resistance Measurements

The contribution of the galvanic coupling reaction to the overall conversion of Ag_2O to AgBr was further investigated by performing linear polarization measurements as a function of reaction time. The linear polarization technique determines the current-potential relationship near the open circuit potential [5–7]. The potential is scanned over

a narrow range centred on the open circuit potential, in these experiments from -15 to $+15$ mV_{E_{oc}}. The polarization resistance can be determined from this curve by:

$$R_p = \left(\frac{\Delta E}{\Delta i} \right)_{E_{oc}} \quad (8.1)$$

where R_p is the polarization resistance determined from the slope of the potential (ΔE) versus current density (Δi) curve at the open circuit potential [5–7].

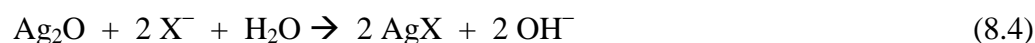
The Butler-Volmer equation (Chapter 2, equation 2.15) describes the measured current as a function of overpotential for a simple half-reaction (i.e., the forward and reverse of the same reaction). In the present case, or in a typical corrosion system, we are looking at two half-reactions, each with kinetics described by a different Butler-Volmer equation. For our particular system, the cathodic half reaction is given by:



and the anodic half reaction is given by:



The total reaction is



The observed current-potential relationship can be described by the sum of the Butler-Volmer relationships for the two half-reactions which is given by the Wagner-Traud equation [5–7]

$$i_{net} = i_{corr} \left[e^{\left(\frac{E-E_{oc}}{b_a} \right)} - e^{\left(\frac{E-E_{oc}}{b_c} \right)} \right] = i_{corr} \left[10^{\left(\frac{E-E_{oc}}{b_a} \right)} - 10^{\left(\frac{E-E_{oc}}{b_c} \right)} \right] \quad (8.5)$$

Note that b_a and b_c are the anodic and cathodic Tafel slopes. This form appears somewhat simpler than the sum of two Butler-Volmer equations because each half

reaction is polarized far enough from its equilibrium potential that the reverse reactions are negligible and the corresponding terms in the Butler-Volmer equation can be dropped.

If the system is polarized away from E_{OC} in either the anodic or cathodic direction a current will result, which has contributions from both the anodic and cathodic reactions. When the potential is polarized over a small range (ΔE), the current-potential relationship is linear (as it is in the individual Butler-Volmer expressions), because

$$e^x \cong 1 + x \text{ as } x \rightarrow 0 \quad (8.6)$$

therefore for small ΔE

$$i_{net} = i_{corr} \left[\left(1 + \frac{2.3\Delta E}{b_a} \right) - \left(1 + \frac{2.3\Delta E}{b_c} \right) \right] \quad (8.7)$$

The slope of the plot of i_{net} versus E is given by $\left(\frac{\Delta E}{\Delta i} \right)$ which is R_p (previously defined in equation 8.1). Using equation 8.1, 8.5 and 8.7 a new equation called the Stern-Geary equation can be defined:

$$i_{corr} = \left(\frac{b_a |b_c|}{2.3(b_a + |b_c|)} \right) R_p \quad (8.8)$$

The Stern-Geary equation relates the slope of the linear current-potential region to the Tafel slopes and corrosion current [8].

Linear polarization measurements are used extensively to determine changes in the corrosion rate [9]. However, caution needs to be taken when performing these measurements, as a number of conditions must be met in order for the results to be valid [6,8–10]. Our system violates a number of these implicit assumptions. Firstly, the surface conditions are constantly changing while the LPR measurements are being made

since the conversion of Ag_2O to AgX is occurring. A drift in the E_{OC} during the LPR measurement can introduce error that cannot be compensated for in the observed current-potential relationship. Another requirement is that the anodic and cathodic reactions must be under kinetic control. We are unsure whether the anodic or cathodic reactions are mass-transfer limited or if the rate-limiting step is mass-transfer limited, therefore we cannot assume that anodic and cathodic currents are under kinetic control. Finally, LPR measurements should usually be made at least 25 mV away from the reversible redox potentials to avoid contributions from the back reactions [8]. This is violated when LPR measurements are acquired in stage 1 and stage 3 of the conversion process.

Linear polarization measurements were used here only as a qualitative, rather than quantitative tool, in order to detect changes at the $\text{Ag}/\text{Ag}_2\text{O}$ and $\text{Ag}_2\text{O}/\text{solution}$ interface during the conversion reaction. Unfortunately, corrosion rates that are specific to our system cannot be determined using this technique, however, information that is complimentary to the potentiostatic polarization results was acquired.

The LPR results recorded during the reaction of Ag_2O with $\text{Br}^-(\text{aq})$ are presented in Figure 8.3. Since the E_{OC} gradually decreases from a value close to $(E^e)_{\text{Ag}_2\text{O}/\text{Ag}}$ to $(E^e)_{\text{AgBr}/\text{Ag}}$, LPR scans collected at the start of the conversion reaction are at potentials close to $0.22 \text{ V}_{\text{SCE}}$ and those collected at the end of conversion are centred around $0.067 \text{ V}_{\text{SCE}}$. Stages 1 through 3 are labelled on Figure 8.3; however, the gradual decrease in E_{OC} made differentiating between the three stages difficult, and therefore these should be taken as approximations only.

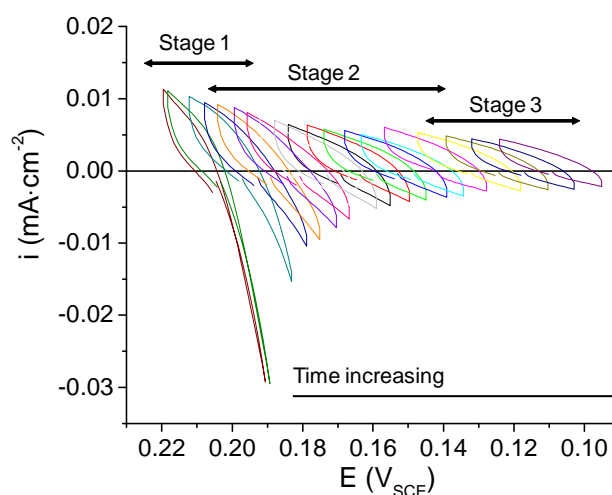


Figure 8.3 Anodic and cathodic currents measured during polarization over the potential range $E_{OC} \pm 15$ mV during the conversion of Ag_2O to AgBr in $1 \times 10^{-4} \text{ mol}\cdot\text{dm}^{-3} \text{ Br}^-(\text{aq})$ solutions.

Initially, the cathodic current showed no hysteresis during the forward and reverse potential scans (first two LPR scans), however the anodic current showed a distinct capacitive loop. We have attributed the capacitive loop to a pseudo-capacitance resulting from $\text{Br}^-(\text{aq})$ adsorption onto the Ag surface on the positive-going scan and $\text{Br}^-(\text{aq})$ desorption on the negative-going scan. The observed pseudo-capacitance may have contributions from the adsorption/desorption of $\text{OH}^-(\text{aq})$ and from $\text{Ag}^+(\text{aq})$ adsorption/desorption, however, we believe that the contributions from these processes are small.

While $\text{Br}^-(\text{aq})$ was desorbing from the Ag surface as the potential was scanned in the negative direction, the oxidation of Ag to AgBr continued to occur, but at a lower rate. At stage 1, the electrochemical process responsible for the cathodic current was reduction of Ag_2O to Ag and $\text{OH}^-(\text{aq})$, and no capacitive behaviour was observed. The Ag_2O film thinned as it was converted to AgBr and the current behaviour of $\text{Br}^-(\text{aq})$

adsorption and desorption became the dominant feature of the voltammogram. As the E_{OC} decreased with time, the linear polarization measurement yielded smaller anodic and cathodic currents. A shift in the E_{OC} to more negative potentials resulted in a decrease in the overpotential for the oxidation of Ag to AgBr. Therefore, we would expect a corresponding decrease in the rate (anodic current) of AgBr formation, since the rate of an electrochemical reaction is related to the overpotential. The adsorption/desorption of $Br^-(aq)$ will also be potential dependent. Therefore, the slight decrease in the anodic branch of the LPR scan indicates a change in the rate of adsorption/desorption. Additional experiments would be required to establish the relationship between the potential and the adsorption/desorption process.

As the E_{OC} shifted to more negative potentials, the overpotential for the reduction of Ag_2O to Ag increased, however, as mentioned above, a decrease in the cathodic current was observed. Since the conversion of Ag_2O to AgBr occurred throughout the LPR measurements, the amount of Ag_2O available to for the cathodic reaction decreased and a smaller cathodic current was observed.

8.3.3 Reaction of Ag_2O with $I^-(aq)$

8.3.3.1 Potentiostatic Polarization at $(E^e)_{Ag_2O/Ag}$

The current observed during polarization at 0.22 V_{SCE} applied immediately after transferring the electrode to a solution containing $I^-(aq)$ is shown in Figure 8.4a. The current quickly reached a steady-state value of 0.08 mA·cm⁻². This steady-state current was equal in magnitude to the diffusion-limited current recorded during the electrochemical growth of AgI on bare Ag, which is shown in Figure 8.4a. We have

attributed this current to the anodic growth of AgI at the Ag₂O/solution interface, and not at the Ag/Ag₂O interface as observed in Br⁻(aq) solutions. Since the porous Ag₂O film was relatively conducting (with a resistance of 416 Ω·cm² (Chapter 3), the anodic oxidation of Ag with X⁻(aq) is possible at the Ag₂O/solution interface if the potential at that interface exceeds the $(E^e)_{AgX/Ag}$ (i.e., an overpotential is required to drive the electrochemical reaction). When a sufficiently large overpotential exists at the Ag₂O/surface, a Ag(I) cation can be injected into the oxide lattice by the oxidation of Ag at the Ag/Ag₂O interface, it can then migrate to the Ag₂O/solution interface and react with X⁻(aq) to form AgX. The exact cation transport mechanism is not known, and could include cation vacancy transport, interstitial migration and/or transport through grain boundaries. In the bromide case, the overpotential is not sufficiently large for this process to occur, due to the small difference between $(E^e)_{Ag_2O/Ag}$ and $(E^e)_{AgBr/Ag}$. The anodic oxidation of Ag by Br⁻(aq), thus, requires the diffusion of Br⁻(aq) to the Ag substrate (see schematic in Figure 8.5).

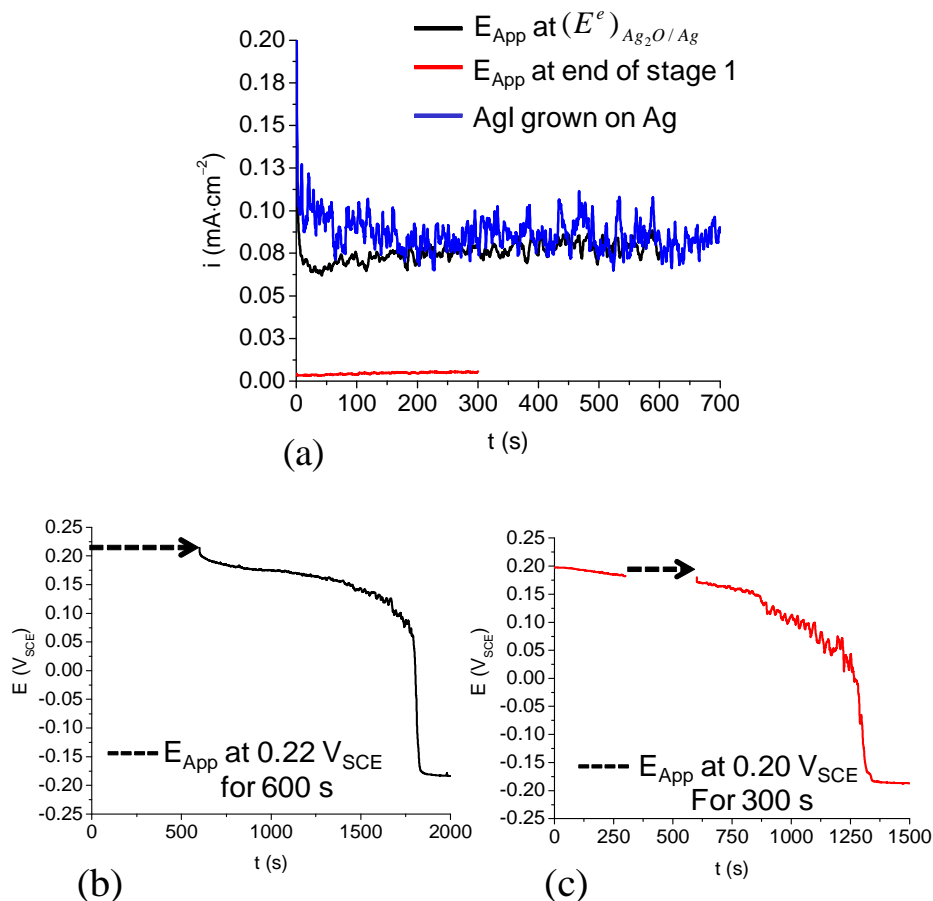


Figure 8.4 (a) Currents observed during the potentiostatic periods of the partial control experiments as described in section 8.3.2.1 and 8.3.2.2. The current observed during anodization at 0.00 V_{SCE} of an oxide-free Ag electrode in 5×10^{-4} mol·dm⁻³ Γ (aq) solution is also shown for comparison. Potential profiles recorded during partially controlled potentiostatic experiments; (b) 0.22 V_{SCE} was applied for 600 s immediately after transfer of the Ag₂O/Ag electrode to the iodide solution, followed by E_{OC} measurement; (c) E_{OC} was measured until the end of stage 1, followed by potentiostatic control at E_{OC} (0.20 V_{SCE}) for 300 s, followed by further measurement at E_{OC} .

The anodic reaction of Ag with Γ (aq) is known to quickly become diffusion limited at relatively small overpotentials (Figure 3.4, Chapter 3, section 3.3.3). The large, constant anodic current during the potentiostatic polarization at 0.22 V_{SCE} is thus

attributed to the anodic formation of AgI on Ag₂O, which depends on the concentration of $\Gamma(\text{aq})$ at the Ag₂O/solution interface and is also diffusion-limited.

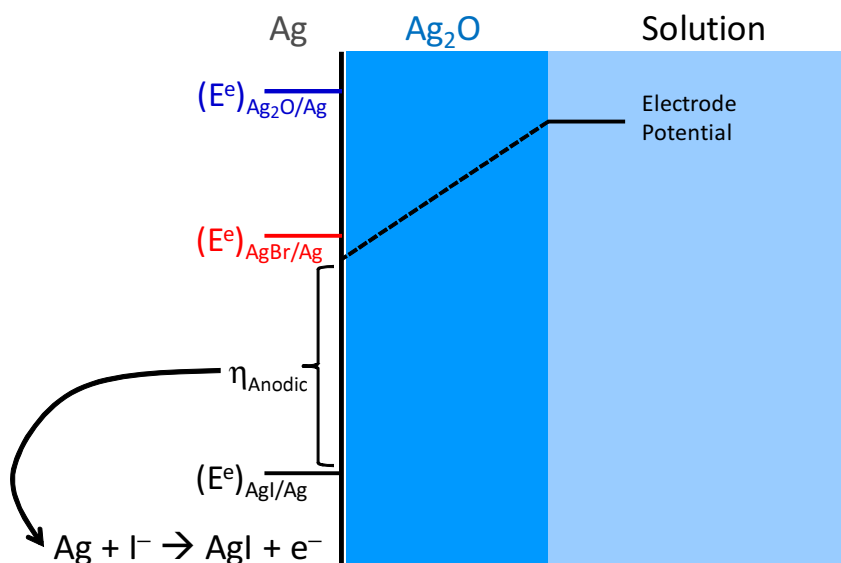


Figure 8.5 Schematic of the Ag/Ag₂O/solution interface in $X^-(\text{aq})$ solutions.

The E_{OC} dropped to $(E^e)_{\text{AgI}/\text{Ag}}$ after 1100 s, as shown in Figure 8.4b. This reaction time was longer than the τ_f of 600 s observed for the reaction of Ag₂O with $\Gamma(\text{aq})$ on open circuit. The time required for complete conversion may have been longer than what is observed without polarization at 0.22 V_{SCE} because the anodic growth of AgI on top of the Ag₂O film may have blocked the Ag₂O reaction sites or restricted the diffusion of $\Gamma(\text{aq})$ to the sites. This hypothesis is further supported by the SEM micrographs of AgI grown potentiostatically on Ag electrodes (shown in Figure 3.8, Chapter 3, section 3.3.6). Images of anodically grown AgI on Ag substrates show that the electrode is covered by a cohesive AgI film.

8.3.3.2 Potentiostatic Polarization at the End of Stage 1

When the reaction was allowed to proceed to the end of stage 1, the current measured during polarization at 0.20 V_{SCE} was negligible (Figure 8.4a). As discussed in Chapters 4 and 5, the reaction of $\Gamma(\text{aq})$ with Ag_2O on open circuit is fast. Thus, the concentration of $\Gamma(\text{aq})$ at the $\text{Ag}_2\text{O}/\text{solution}$ interface will be very small, even during the later stages of conversion. When a potential is applied at the end of stage 1, only a small amount of $\Gamma(\text{aq})$ is available at the $\text{Ag}_2\text{O}/\text{solution}$ interface to support the anodic formation of AgI , therefore the anodic current is small. The reduction of Ag_2O to Ag may also occur at this applied potential, which would further reduce the net current.

These observations are consistent with those reported in our previous study where the reaction was allowed to proceed for a shorter time (until the midpoint of stage 1) [11]. The main difference was the effect of polarization on the reaction time (see below). Zhang et al. also performed polarization experiments during stage 2. In stage 2, the chemical conversion of Ag_2O to AgI progressed significantly and diffusion of $\Gamma(\text{aq})$ to the Ag substrate was no longer negligible. When a fixed potential was applied after the system reached stage 2, the current increased quickly, reaching a maximum magnitude equal to the diffusion-limited current observed for the anodic oxidation of Ag with $\Gamma(\text{aq})$ on a Ag_2O -free Ag electrode [11].

The E_{OC} behaviour observed after partial potentiostatic control is shown in Figure 8.4c. It took another 600 s for E_{OC} to drop to $(E^e)_{\text{AgI}/\text{Ag}}$, resulting in a total reaction time on open circuit of 900 s. This reaction time was shorter than the time observed during polarization at 0.22 V_{SCE}, but still longer than the τ_f of 600 s observed for the reaction of

$\Gamma(\text{aq})$ on $\text{Ag}_2\text{O}/\text{Ag}$ on open circuit. The anodically grown AgI may have blocked some of the available Ag_2O reaction sites or restricted the diffusion of $\Gamma(\text{aq})$ to them, resulting in a longer τ_f . This effect will be much smaller when the polarization is applied at a later stage.

8.3.3.3 Linear Polarization Resistance Measurements

The LPR results recorded during the reaction of Ag_2O with $\Gamma(\text{aq})$ are presented in Figure 8.6. Like the LPR measurements acquired in $\text{Br}^-(\text{aq})$ solutions, scans collected during stage 1 are centred close to $0.20 V_{\text{SCE}}$, those acquired as the reaction approached completion are located at lower potentials, and finally those acquired after conversion was complete overlap at about $-0.16 V_{\text{SCE}}$.

The early capacitive loop observed in the first three LPR scans shown in Figure 8.6 are consistent with the anodic formation of AgI on Ag_2O , which was also observed during potentiostatic polarization at $0.22 V_{\text{SCE}}$. When the potential was scanned in the positive direction, $\Gamma(\text{aq})$ (or $\text{OH}^-(\text{aq})$) at the Ag_2O surface reacted with Ag(I) that originated from the oxidation of Ag at the $\text{Ag}/\text{Ag}_2\text{O}$ interface. Cyclic voltammetric results presented in Chapter 3 have shown that the Ag(I) transport through Ag_2O and AgX films is a relatively fast process, as low resistance values were measured during film reduction. The CV also shows an anodic current that was attributed to $\text{OH}^-(\text{aq})$ adsorption in addition to the $\Gamma(\text{aq})$ diffusion-limited steady-state current for the oxidation of Ag to AgI when the potential was scanned above $0.0 V_{\text{SCE}}$. This is consistent with the claim that the capacitive loop is due to a pseudo-capacitance related to the adsorption of $\Gamma(\text{aq})$ and $\text{OH}^-(\text{aq})$ species on the Ag_2O film.

Unlike in the $\text{Br}^-(\text{aq})$ case, the cathodic current shows a slight hysteresis after short reaction times. It is believed that two processes are responsible for the observed current behaviour, these are the reduction of Ag_2O to Ag and $\text{OH}^-(\text{aq})$ and the desorption of $\Gamma(\text{aq})$.

In the bromide case the capacitive loop became more prominent with time, but for iodide, the influence of the capacitive behaviour was more significant at stage 1 and diminished with time. Since the chemical reaction of Ag_2O with iodide is fast, most of the available $\Gamma(\text{aq})$ is consumed by this reaction. As a result, the concentration of $\Gamma(\text{aq})$ at the $\text{Ag}/\text{Ag}_2\text{O}$ interface is much less than the bulk $\Gamma(\text{aq})$ concentration, until the Ag_2O film is completely converted to AgI . This explains the significant decrease in magnitude of the anodic and cathodic currents at stage 2. As the Ag_2O film thins by conversion to AgI , the adsorption and desorption of $\Gamma(\text{aq})$ on Ag_2O becomes less prominent in the LPR voltammograms. At this point in the reaction a significant amount of Ag_2O has converted to AgI , and the adsorption and desorption behaviour of $\Gamma(\text{aq})$ on $\text{Ag}/\text{Ag}_2\text{O}/\text{AgI}$ shows different behaviour from that observed on Ag_2O -only. However, if we compare the shape and magnitude of the anodic and cathodic currents to those observed at stage 3, we see that they are very similar. This result, in addition to the partial potentiostatic control experiments, suggests that at stage 2 the Ag_2O film shows signs of porosity and that a small amount of $\Gamma(\text{aq})$ penetrates through the film, reaching the Ag substrate.

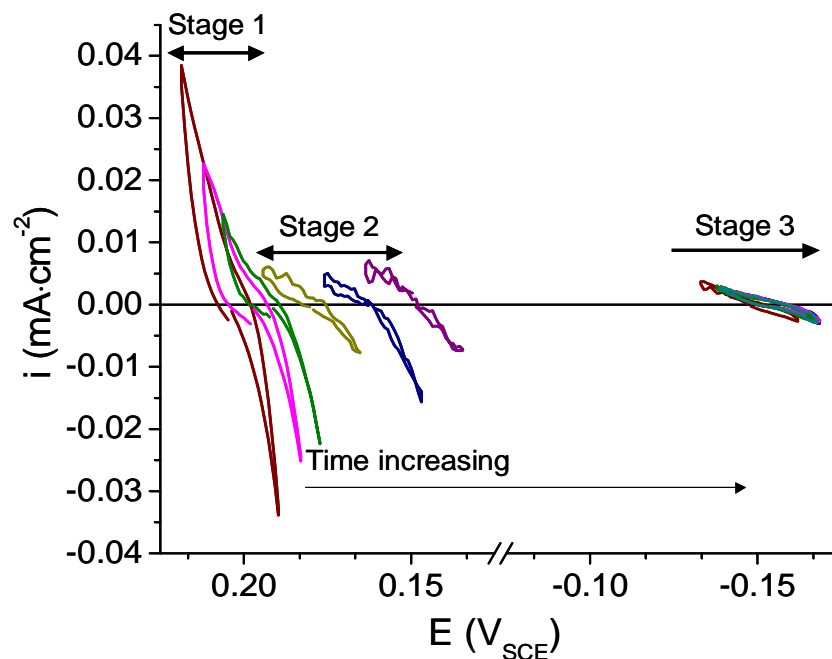


Figure 8.6 Anodic and cathodic currents measured during polarization over the potential range $E_{OC} \pm 15$ mV during the conversion of Ag_2O to AgI in 1×10^{-4} mol·dm $^{-3}$ $\Gamma(\text{aq})$ solutions.

In some instances (though not in the experiment of Figure 8.6) LPR measurements were acquired during the potential transition (Figure 8.7). Scanning in both the positive and negative direction resulted in an anodic current, which was attributed to oxidation of Ag to AgI . This is a consequence of the rapid changes in the kinetics of the cathodic reaction during the potential transition. This result demonstrates how a change in the surface conditions during an individual LPR measurement can affect what is actually being measured and the validity of the measurement.

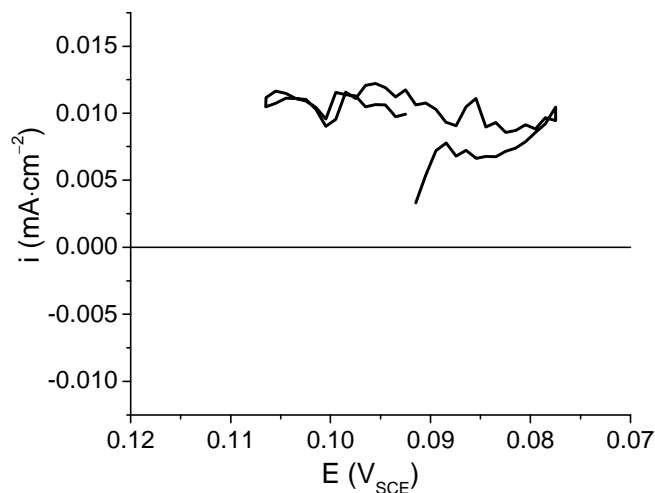


Figure 8.7 Current measured during polarization over the potential range $E_{OC} \pm 15$ mV during the conversion of Ag_2O to AgI in 1×10^{-4} mol·dm $^{-3}$ $\Gamma(\text{aq})$ solutions near the potential transition.

8.4 Conclusions

In this chapter, the galvanic coupling reaction (pathway 3) was probed at different times during the conversion of Ag_2O to AgX . This was accomplished by performing potentiostatic polarization (constant potential) and linear polarization resistance (scanning potential) measurements during the conversion reaction. The current measured during potentiostatic polarization immediately after exposure to $\text{Br}^-(\text{aq})$ increased gradually, until it reached a value equal in magnitude to the current measured during AgBr growth on Ag electrodes. We attributed this current to the growth of a AgBr film at the $\text{Ag}/\text{Ag}_2\text{O}$ interface. The anodic formation of AgBr depleted the concentration of $\text{Br}^-(\text{aq})$ near the electrode surface, which resulted in a suppression of the chemical conversion of Ag_2O to AgBr . A similar result was observed during polarization at the end of stage 1, except the current was near the steady-state current observed during AgBr growth at the start of the

potentiostatic polarization measurement. This suggested that the concentration of bromide at the Ag/Ag₂O is nearly equal to the bulk concentration.

Linear polarization measurements were made throughout the duration of the conversion reaction, however, the results are interpreted in a qualitative manner and used as supporting evidence to the potentiostatic polarization results. In the bromide reaction, the measured anodic currents showed a distinct capacitive loop that was attributed to a pseudo-capacitance resulting from Br⁻(aq) adsorption onto the Ag surface on the positive-going scan and Br⁻(aq) desorption on the negative-going scan. Initially, the cathodic current showed no capacitive behaviour and was attributed to the reduction of Ag₂O to Ag. However, as the Ag₂O film thinned as it converted to AgBr, the pseudo-capacitance became the dominant feature of the voltammogram.

In the iodide case, the current measured during potentiostatic polarization at $(E^e)_{Ag_2O/Ag}$ was identical to the current measured during AgI formation on Ag substrates. Since the difference between $(E^e)_{Ag_2O/Ag}$ and $(E^e)_{AgI/Ag}$ is large, the potential at the Ag₂O/solution interface is large enough to drive the electrochemical formation of AgI on the Ag₂O surface. A negligible current was measured at the end of stage 1. At this time, I⁻(aq) available at the electrode surface will be consumed by the fast chemical reaction between Ag₂O and I⁻(aq).

The contribution from the pseudo-capacitance due to I⁻(aq) adsorption and desorption diminished with time. This is consistent with the potentiostatic polarization results, and was likely due to the fast chemical conversion of Ag₂O to AgI. The E_{OC} behaviour, potentiostatic control, and LPR results suggest that little or no I⁻(aq) diffused through the Ag₂O film to the Ag surface, likely due to the fast chemical reaction of Ag₂O

and $\Gamma(\text{aq})$. Therefore, the galvanic coupling reaction should not contribute significantly in the net reaction of Ag_2O to AgI . This was not the case in the bromide reaction; however additional experiments would be required in order to determine meaningful corrosion rates.

8.5 References

1. X. Zhang, S.D. Stewart, D.W. Shoesmith, and J.C. Wren, *J. Electrochem. Soc.*, **154**, F70 (2007).
2. V.I. Birss, and G.H. Wright, *Electrochim. Acta*, **27**, 1429 (1982).
3. V.I. Birss, and G.H. Wright, *Electrochim. Acta*, **27**, 1439 (1982).
4. A.G. Brolo, and Y. Yang, *Electrochim. Acta*, **49**, 339 (2004).
5. V.C. Wagner, W. Traud, *Z. Electrochemie Angewandt Physika.*, **44(7)**, 391 (1938).
6. F. Mansfield, "The Polarization Resistance Technique for Measuring Corrosion Currents," in *Advances in Corrosion Science and Technology*, Vol. 6, New York: Plenum Press, 1976.
7. G.S. Frankel, *J. ASTM Internat.*, **5(2)**, Paper ID JAI101241 (2008).
8. M. Stern, and A.L. Geary, *J. Electrochem. Soc.*, **104**, 56 (1956).
9. J.R. Scully, *Corrosion*, **56**, 199 (2000).
10. J. Tafel, *Z. Phys. Chem.*, **50**, 64 (1905).
11. X. Zhang, D.W. Shoesmith, and J.C. Wren, *Corr. Sci.*, **50**, 490 (2008).

Chapter 9

Summary and Future Work

9.1 Summary

This thesis examined the mechanism and kinetics of surface reactions involving the conversion of an aqueous halide on silver oxide surfaces. Under the experimental conditions used to investigate the interfacial reaction kinetics, the aqueous-solid conversion of reaction Ag_2O with $\text{X}^-(\text{aq})$ to form AgX on a conducting Ag substrate can occur via one of three main reaction pathways. The first pathway is a chemical reaction (no charge transfer) that occurs at the oxide/solution interface. Conversion can also proceed via a galvanic coupling pathway where the reduction of Ag_2O to Ag is coupled to the oxidation of Ag to AgX . Lastly, conversion can proceed via a dissolution pathway, where $\text{Ag}^+(\text{aq})$ released from Ag_2O dissolution reacts with $\text{X}^-(\text{aq})$ in solution. The AgX that forms in the solution phase can either precipitate on the Ag substrate or remain in solution.

From studies of the electrochemical and morphological properties of silver oxide and silver halide films formed on Ag electrodes under various conditions we have determined that the type of film formed depends on the solution conditions and the magnitude of the applied potential.

The conversion of Ag_2O films on Ag substrates to AgI in aqueous iodide solutions was followed at the open circuit potential (E_{OC}) and cathodic stripping voltammetry measurements were made at different reaction times. The conversion reaction was initiated by placing a Ag_2O -covered Ag electrode into a solution containing

$\Gamma(\text{aq})$. The E_{OC} showed three distinct stages of conversion. In stage 1, the initial E_{OC} starts close to the equilibrium potential for the $\text{Ag}_2\text{O}/\text{Ag}$ redox pair, $(E^e)_{\text{Ag}_2\text{O}/\text{Ag}}$, and decreased slowly with time. In stage 2, the E_{OC} reached and remained at a nearly constant value. In stage 3, the E_{OC} abruptly drops and quickly reached a steady value close to the equilibrium potential for the AgI/Ag redox pair, $(E^e)_{\text{AgI}/\text{Ag}}$ and the change in stage 3 indicated that the conversion from Ag_2O to AgI was complete.

Cathodic current reduction of Ag_2O and AgI to Ag provided a measure of the amount of Ag_2O converted. The conversion reaction was nearly 100% efficient. From the total reaction times as a function of iodide concentration and initial Ag_2O inventory, the reaction rate was found to be first order in iodide concentration and first order in oxide surface area. Based on the kinetic analysis, we determined that the reaction of Ag_2O with $\Gamma(\text{aq})$ forming AgI occurred mainly by a chemical reaction path.

The influence of electrolyte composition on (i) composition and morphology of the Ag_2O film and (ii) the kinetics of the conversion was also investigated. The reaction rate constant in phosphate solutions was approximately two times larger than the value measured in an NaOH solution. This difference was attributed to the differences in the initial surface area or surface structure of the Ag_2O films grown in the presence and absence of phosphate. While $\mu\text{-XRD}$ analysis results suggest the incorporation of phosphate into the Ag_2O matrix occurs during the anodic Ag_2O film growth in phosphate solutions, this does not seem to have any impact on the mechanism or kinetics of the conversion reaction.

The effect of mass transfer on the reaction kinetics was investigated and the reaction time was found to be inversely proportional to the square root of the electrode

rotation rate. These results enabled us to determine a surface chemical reaction rate. This surface reaction rate constant was approximately one to two orders of magnitude larger than the reaction rate constant obtained under stagnant conditions indicating that the conversion reaction is mass-transfer limited under stagnant conditions.

Neutron reflectometry was performed *in situ* during the conversion of Ag_2O to AgI to investigate the mechanism of the conversion reaction. The neutron reflectometry results show that the $\text{Ag}_2\text{O}/\text{AgI}$ interface can be modelled as a layered structure with the conversion occurring layer-by-layer. To confirm that this layered model accurately represents the $\text{Ag}/\text{Ag}_2\text{O}/\text{AgI}$ interfaces, the neutron reflectometry data should be re-analyzed in a way that will allow some variance in the scattering length density values.

The reaction of $\text{Br}^-(\text{aq})$ with Ag_2O on Ag was also studied. The chemical reaction pathway in this system is slower than the iodide system. This results in a build-up of $\text{Br}^-(\text{aq})$ at the $\text{Ag}/\text{Ag}_2\text{O}$ interface and enables the galvanic coupling reaction to occur at a faster and competes with the chemical reaction pathway. Also, dissolution of Ag_2O and release of $\text{Ag}^+(\text{aq})$ leads to the formation of $\text{AgBr}(\text{aq})$ which is more soluble than AgI . The higher AgBr solubility allows it to diffuse in the bulk solution instead of immediately precipitating on the $\text{Ag}_2\text{O}/\text{AgBr}$ film. Both the electrochemical results and SEM images of the $\text{Ag}/\text{Ag}_2\text{O}$ surface confirmed that formation of AgBr via the dissolution pathway is more prevalent in the $\text{Br}^-(\text{aq})$ system than in the $\text{I}^-(\text{aq})$ system.

9.2 *Future Work*

We believe that a more complete understanding of the galvanic coupling reaction pathway can be achieved by completing a few additional experiments. The cyclic

voltammetry results presented in Chapter 3 showed that the polarization resistance measured during Ag_2O or AgX reduction was significantly lower when phosphate was present in the electrolyte solution. These lower resistance values are attributed to solid-state diffusion in the oxide or halide lattice. However, the polarization resistance values measured during Ag_2O and AgX reduction in NaOH were close to the solution resistance. By performing further linear polarization resistance and potentiostatic polarization measurements in the presence of phosphate, we can minimize the influence of the solution resistance and this may provide us with a better understanding of the factors that affect the galvanic coupling reaction.

Another researcher in our group has performed potentiostatic polarization measurements at the end of stage 2 of the $\text{Ag}_2\text{O}/\Gamma(\text{aq})$ conversion reaction, and the results were quite different from those discussed in Chapter 8. Our results suggested that galvanic coupling was most likely to occur during stage 2. Additional experiments that probe the galvanic coupling reaction at the beginning and middle of stage 2 would help to confirm this. Additionally, SEM images of the surface may provide qualitative information (i.e., film layering, crystal sizes/shapes) that may support or enhance the understanding of the potentiostatic polarization and linear polarization resistance results. Some of these experiments have been performed and the results, when analyzed, will be published later.

A few simple experiments could also be completed to investigate the extent of the dissolution observed during the conversion of Ag_2O to AgBr . A number of techniques could be used including; rotating ring disc experiments and electron probe beam

diffraction. The measurements should be performed *in situ* so that the charged species that is migrating away from the electrode surface can be identified.

More extensive computer modelling of the open circuit potential profile as a function of iodide concentration, initial amount of Ag_2O , and electrode rotation rate could be useful. This could inform us further on how the dominant conversion pathway changes with respect to the chemical/electrochemical environment. This would be important for applications where silver surfaces/particles are used for radioiodine trapping.

A long term goal of this work is to use the knowledge gained from the silver/silver oxide and silver/silver halide system and apply it to other metal oxide/metal halide or metal oxide/metal sulphide systems. Smith et al. have applied some of the principles of the kinetic model described in Chapter 4 to the copper oxide/copper sulphide system, but did not complete a detailed kinetic analysis of the system. Extension of the silver work to include an investigation of the conversion of silver oxide to silver sulphide may help to identify how changes in the potential difference between the equilibrium potentials of the AgX/Ag and $\text{Ag}_2\text{S}/\text{Ag}$ redox pairs affects the rates of reaction and the role of solvent properties and surface morphology more generally for surface conversion reactions.

Sarah D. Pretty
B.Sc., Ph.D.

EDUCATION and QUALIFICATIONS

Ph.D. Chemistry

(Sept. 2006 – Dec. 2011)

Department of Chemistry, University of Western Ontario, London, ON

B.Sc. (Hons.) Chemistry

(Sept. 2002 – April 2006)

University of Western Ontario, London, ON

RELATED WORK EXPERIENCE

Graduate Research Assistant:

(2006-2011)

- Responsible for the research and development of a graduate thesis project which requires the use of various skills, including: hypothesis formulation, data collection, experimental optimization, data analysis, summary of results, and establishing directions for future research
- Conducted all scientific research in a clean and safe manner, whereby all laboratory safety rules and restrictions were strictly followed
- Participated in collaborations with researchers from various fields to improve upon and verify thesis project hypotheses
- Recorded, interpreted and reported all scientific data collected in an organized and logical fashion
- Presented research at national and international scientific conferences
- Supervised and directed undergraduate thesis and summer students in their laboratory experiments and authoring of final thesis paper

Graduate Teaching Assistant:

(2006-2011)

- Selected as the Chemistry Outreach Teaching Assistant, aided in the development of the UWO Science Outreach Program
- Assisted in teaching a variety of courses including: 1st year general chemistry, 2nd year physical chemistry and 2nd year analytical chemistry
- Supervised and directed students with their laboratory experiments, which involved both qualitative and quantitative analysis

INVOLVEMENT IN THE NUCLEAR INDUSTRY

- Developed novel methodologies to investigate interfacial surface kinetics or corrosion kinetics related to nuclear safety systems
- Selected as the Nuclear Outreach Teaching Assistant
 - Responsible for the preparation of nuclear-related presentations, activities, and experiments for high school students
- Travelled to the Australian Nuclear Science and Technology Organization and performed in situ electrochemistry with neutron reflectometry

AWARDS and ACHIEVEMENTS

1. *ASPIRE Award Winner, 2010* – Awarded compensation for travel expenses for travel to the Bragg Institute at the Australian Nuclear Science and Technology Organization in Sydney, Australia to perform neutron reflectometry.
2. *CNS/NA-YGN Best Paper Contest Winner, 2008* – Awarded a trip to Switzerland to present thesis work at the 2008 Young Generation in Nuclear Congress.
3. *OGSST Graduate Scholarship, 2007*
4. *CNS Student Conference First Place Award in Chemistry/Chemical Engineering, 2006* – Awarded by members of the Canadian Nuclear Society.
5. *UWO Entrance Scholarship, 2002* – Awarded to students whose average exceeds 80%.

ARTICLES IN PEER-REVIEWED JOURNALS and CONFERENCE PROCEEDINGS

1. **Pretty, S.**, Keech, P.G., Zhang, X., J.J. Noël, Wren, J.C., (2011) The Interfacial Kinetics of Aqueous Iodide Reaction with Ag₂O Surfaces on Ag Substrate: The Effect of Mass Transfer, *Electrochimica Acta*, **56**, 2754-2761.
2. **Pretty, S.**, Zhang, X., Shoesmith, D.W., and Wren, J.C., (2008) Metal-Oxide Film Conversions Involving Large Anions. Conference Proceedings, IYNC 2008, Interlaken, Switzerland, paper # 112.
3. Zhang, X., **Stewart, S.**, Shoesmith, D.W., and Wren, J.C., (2007) Interaction of Aqueous Iodine Species with Ag/Ag₂O Surfaces. *Journal of the Electrochemical Society*, **154** (4) p.F70.

PRESENTATIONS and POSTERS

1. **Pretty, S.**, Keech, P.G., Zhang, X., Wren, J.C., (2010) Corrosion of Ag-Ag₂O in Iodide Solutions: A Potential Radioiodine Immobilization Route. Presented at the ECS Canadian Division Fall Symposium, London, ON. (poster)
2. **Pretty, S.**, Keech, P.G., Zhang, X., Wren, J.C., (2010) Corrosion of Ag-Ag₂O in Iodide Solutions: A Potential Radioiodine Immobilization Route. Presented at the Gordon Conference for Aqueous Corrosion, New London, NH. (poster)
3. **Pretty, S.**, Zhang, X., Keech, P.G., Wren, J.C. (2010) Corrosion of Ag-Ag₂O in Iodide Solutions: A Potential Radioiodine Immobilization Route. 32nd Annual Conference of the Canadian Nuclear Society & 35th Canadian Nuclear Society. (poster)
4. **Pretty, S.**, Zhang, X., Keech, P.G., Shoesmith, D.W., and Wren, J.C. (2009) Electrochemical and Surface Analytical Investigation of the Solid-Aqueous Phase Reaction Kinetics for the Conversion of Ag₂O to AgI in Aqueous Iodide Solutions. Presented at the American Chemical Society Fall 2009 Meeting and Exposition, Washington, DC. (oral)
5. **Pretty, S.**, Zhang, X., Keech, P.G., Shoesmith, D.W., and Wren, J.C. (2009) Electrochemical and Surface Analytical Investigation of the Solid-Aqueous Phase Reaction Kinetics for the Conversion of Ag₂O to AgI in Aqueous Iodide Solutions. Presented at the 92nd Canadian Conference and Exhibition, Hamilton, ON. (poster)
6. **Pretty, S.**, Zhang, X., Shoesmith, D.W., and Wren, J.C. (2008) Metal-Oxide Film Conversions Involving Large Anions. Conference Proceedings, IYNC 2008, Interlaken, Switzerland, paper # 112. (oral)
7. **Pretty, S.** (2007) Metal Oxide Film Conversion Involving Large Anions. 29th Annual Conference of the Canadian Nuclear Society & 32th Canadian Nuclear Society. (oral)
8. Zhang, X., Wren, J.C., **Stewart, S.**, Shoesmith, D.W. (2006) Interaction of Aqueous Iodine Species with Ag/Ag₂O Surfaces. Presented at the Gordon Conference for Aqueous Corrosion, New London, NH. (poster)
9. Wren, J.C., Zhang, X., **Stewart, S.**, Shoesmith, D.W. (2006) Interaction of Aqueous Iodine Species with Ag/Ag₂O Surfaces. Presented at the 89th Canadian Conference and Exhibition, Halifax, NS. (oral)
10. **Stewart, S.**, (2006) Interaction of Aqueous Iodine Species with Ag/Ag₂O Species. 27th Annual Conference of the Canadian Nuclear Society & 30th Canadian Nuclear Society. (oral)